# Determining the cellular localisation of novel cancer therapeutics

A thesis submitted to the University of Birmingham for the degree of

DOCTOR OF PHILOSOPHY

*Student:*
Laura Elizabeth Rowley

PSIBS Doctoral Training Centre
College of Engineering and Physical Sciences
University of Birmingham
September 2013

UNIVERSITY OF
BIRMINGHAM

University of Birmingham Research Archive

e-theses repository

This unpublished thesis/dissertation is copyright of the author and/or third parties. The intellectual property rights of the author or third parties in respect of this work are as defined by The Copyright Designs and Patents Act 1988 or as modified by any successor legislation.

Any use made of information contained in this thesis/dissertation must be in accordance with that legislation and must be properly acknowledged. Further distribution or reproduction in any format is prohibited without the permission of the copyright holder.

# Acknowledgements

I would firstly like to thank my supervisors Mike, Jose, Nik and Ela for their support, knowledge and encouragement over the past five years. Their continued enthusiasm and commitment to the project have ensured that I have made it this far. I would like to thank them for giving me the opportunity to work with them, and for supporting me pastorally as well as academically. I would also like to thank the members of Hannon, Bunch and Hodges groups who have all been a constant source of help, sometimes through helpful discussions about my work, but mainly by just being genuinely nice people who made days in the lab enjoyable - no mean feat!

I must also give thanks to all the members of the PSIBS Doctoral Training Centre, many of whom started as colleagues but are now firm friends. The *raison d'être* for PSIBS was to bring together people from a physical science background who were keen to share knowledge and collaborate to apply our collective knowledge to a wide range of biomedical questions. The centre has worked due to the willingness of the students, staff and collaborators to work towards that aim and I genuinely believe that each student to pass through this centre will produce a PhD of great quality because of this ethos. To that end, I must specifically thank James Brown, Alan Race and Lois Harries for their work within Hannon group as part of their PSIBS 'mini-projects', all of which helped further the work presented here. I must also thank Zahra Khan, Lindsey van Gemeren and Richard Williams for giving up their time and a small part of their sanity to take part in experimental work at Diamond Light Source. The shift patterns required to keep work going at Diamond are punishing and I am grateful to them for putting in such a huge amount of effort to help.

As well as my ‘official’ supervisors, there are many people who have played a key role in this work. Firstly Dr Tina Geraki of Diamond Light Source who helped enormously with experimental design and data analysis, not to mention working through the night with us during beamtime. I must also thank Dr Steve Thomas and Dr Chris Weston, both of the Institute for Biomedical Research, Birmingham who have also provided materials, access to equipment but most importantly their time and knowledge to contribute to the imaging of cell morphology. I am also grateful to Prof Eric Anslyn of The University of Texas for very kindly providing NO imaging probe.

There are several ‘unsung heros’ of both Chemistry and PSIBS, who I would also like to thank. The analytical staff of Dr Neil Spencer, Peter Ashton and Nick May have all given helpful advice over spectra analysis, for which I am very grateful. Then there are staff members such as Stuart Arkless, Ian Bodfish and the wonderful Louise Oram who keep the departments running and happily answered all of the many, many questions I pestered them with.

I cannot complete this section without saying a particular thank you to the friends who have supported me since I joined PSIBS - Amy Davies and Adrian Garcia who, as fellow PSIBS pioneers, have also made it this far and have always been there for a chat over a coffee (or something stronger). Rory Steven, Mim Dowle, Andy Palmer and honorary PSIB-ling Rachel Brown (as well as those mentioned earlier) are responsible for many of the happy memories I take away from PSIBS, and I look forward to my international tour to come and visit you all in the near future!

Finally, I must thank the most important people to me - firstly Rich, for being my best friend and always being there. But of course, I must save my biggest thanks for my parents - none of the wonderful things I’ve had the opportunity to do would have been possible if it wasn’t for you and your constant hard work - I can’t thank you enough for everything you’ve done for me.

# Abstract

Three areas of investigation regarding a novel class of potential anti-cancer therapeutics, triple helicate dinuclear compounds known as ‘cylinders’, have been addressed in this work - the synthesis of a ruthenium-based cylinder, determining the cellular localisation of the cylinders, also determining the cellular effects of the cylinders.

An improved protocol for the synthesis of a ruthenium cylinder has been developed, utilising microwave synthesis as opposed to previously used reflux techniques. Whilst not leading to an increase in yield, the synthesis is now much shorter as there is no need for the synthesis of intermediate compound $Ru(DMSO)_4Cl_2$, and the use of Sephadex C-25 as a solid phase for column chromatography has led to a shorter purification protocol.

First attempts at determining the cellular localisation of the fluorescent ruthenium cylinder have been undertaken, with confocal microscopy showing observable fluorescence within MDA-MB-231 breast cancer cells, but not within SKOV-3 ovarian cancer cells, suggesting some level of preferential uptake or metabolism of cylinder between cell lines. Co-localisation experiments with Hoechst nuclear stains appear to show the reduction in mean fluorescence following treatment with iron cylinder, suggesting localisation of the cylinder within cell nuclei.

Using the I-18 beamline at Diamond Light Source, synchrotron radiation has been used to further investigate the cellular localisation of the cylinders. A sample preparation route of growing cells on silicon nitride windows has been developed, and allowed for the imaging of iron and nickel cylinders within SKOV-3 cells. High levels of iron are found near the cell membrane, corresponding to areas of high calcium concentration, whereas nickel is found more uniformly spread throughout the cell. XANES spectra of these areas show that the iron is in an environment closer to that of the ferric iron found in ferrihydrite as opposed to the ferrous iron found within the cylinder.

The cellular effects of cylinder treatment have also been imaged, with the main observation being that the motility of cells is compromised by cylinder treatment. The iron cylinder causes the production of nitric oxide within MDA-MB-231 cells. Images taken as part of control experiments showed low levels of fluorescence within MDA-MB-231 cells, suggesting that this cell line does produce endogenous nitric oxide, something that has been a subject of debate within the literature.

# Contents

# List of Figures

# List of Tables

## List of Abbreviations

| | |
|---|---|
| A2780 | ovarian cancer cell line |
| ADP | adenosine diphosphate |
| AFM | atomic force microscopy |
| AK | adenylate kinase |
| AMP | adenosine monophosphate |
| ATP | adenosine triphosphate |
| bpy | 2,2’-bipyridine |
| BSA | bovine serum albumin |
| CHCA | hydroxy-4-cinamic acid |
| ct-DNA | calf thymus DNA |
| cNOS | constitutive NOS |
| cRT-PCR | circularised reverse transcription polymerase chain reaction |
| DHB | 2,5-dihydroxybenzoic acid |
| DMSO | dimethyl sulfoxide |
| dpp | diphenyl phenanthroline |
| dppz | dipyrido phenazine |
| eNOS | endothelial NOS |
| ESI-MS | electrospray ionisation mass spectrometry |
| EXAFS | extended X-ray absorption fine structure |
| FBS | foetal bovine serum |
| FITC | fluroscein isothiocyanate |
| FRET | Forster resonant energy transfer |
| GFP | green fluorescent protein |
| HBL-100 | breast cancer cell line |
| HeLa | cervical cancer cell line |
| $IC_{50}$ | concentration of compound required to inhibit cell growth by 50% |
| ICP-MS | Inductively Coupled Plasma Mass Spectrometry |

| | |
|---|---|
| iNOS | inducible NOS |
| KP1019 | indazole trans-tetrachlorobis(indazole)ruthenate(III) |
| KP1339 | sodium trans-tetrachlorobis(indazole)ruthenate(III) |
| LA-ICP-MS | laser assisted inductively couple plasma mass spectrometry |
| LUMO | lowest unoccupied molecular orbital |
| MALDI-MS | matrix assisted laser desorption ionisation mass spectrometry |
| MDA-MB-231 | breast cancer cell line |
| MLCT | Metal to Ligand charge transfer |
| MRC5 | lung cancer cell line |
| MTOC | microtubule organisation centre |
| MTT | 3-(4,5-dimethylthiazol-2-yl)-2,5-diphenyltetrazolium bromide |
| NAMI-A | New Antimetastatic Inhibitor A |
| nNOS | neuronal NOS |
| NONO-AM | diethylamine diazeniumdiolate |
| NOS | nitric oxide synthase |
| PAGE | polyacrylamide gel electrophoresis |
| phen | phenanthroline |
| SH-SY5Y | neuroblastoma cancer cell line |
| SIMS | secondary ion mass spectrometry |
| SKOV-3 | ovarian cancer cell line |
| SPA | sinapinic acid |
| T47D | breast cancer cell line |
| THAP | 2,4,6-trihydroxy-acetophenone |
| TIRF | Total Internal Reflection Microscopy |
| tpphz | tetrapyridophenazine |
| XANES | X-ray absorption near edge structure |
| XAS | X-ray absorption spectroscopy |
| XRF | X-ray fluorescence |

# Chapter 1

# The use and imaging of metallo-drugs

## 1.1 Current metallo-drugs in cancer therapy

The anti-cancer effect of cisplatin was a serendipitous discovery by Barnett Rosenburg, who was investigating the effect of electric current upon the cellular division of *E. coli* bacteria. The cells were kept in an aqueous ammonium chloride buffer and supposedly inert platinum electrodes were used to pass a current through the solution. It was observed that the *E. coli* cells changed morphology to become ling and spindle-like, instead of their normal shorter, wider rod shape. It was initially believed that this was caused by the electrical current, but it was then found that the platinum electrodes were in fact being hydrolysed in the buffer solution, leading to the formation of various platinum compounds [19]. Rosenburg *et al.* then tested a family of platinum salts on *E. coli* bacteria, and found that $(NH_4)_2[PtCl_6]$ caused an even more pronounced elongation of the cells than had previously been observed. It was however found that it was the Pt(IV) compound $PtCl_2(NH_3)_2$ that was being generated by hydrolysis of the electrodes, and it was this compound that was leading to the elongation of the *E. coli* cells. However it was only the *cis* isomer of this compound, which became known as cisplatin, that caused the cells to elongate, the *trans* isomer had no observable effect on the cells [20]. Following subsequent animal trials on mice, cisplatin entered human trials and now, over 30 years after it was approved for clinical use, it is still routinely used in the treatment of many cancers, in particular testicular and ovarian cancers. Due to its success, many other platinum-ammine compounds have been developed and tested as potential anti-cancer treatments. This has led to another two compounds - carboplatin and oxaliplatin - entering worldwide clinical use, with a further three compounds - nedaplatin, heptaplatin and lobaplatin - being approved for use in individual countries [21]. Given their similarity in structure and constituent groups (see Figure 1.1), it is unsurprising that they behave in an analogous way within a physiological environment. The labile chloride or carboxylate ligands are replaced by water molecules to produce mono or di-aqua species, which then bind to DNA in an irreversible way - through metal-nitrogen bonds involving the N7 of purine DNA bases.

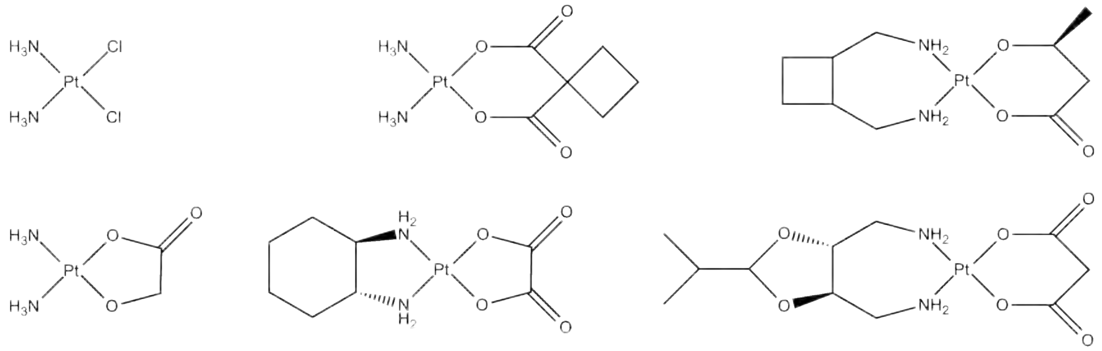

**Figure 1.1:** The structures of platinum-amine based drugs currently in clinical use; cisplatin, carboplatin, lobaplatin (top row) and nedplatin, oxaliplatin and heptaplatin (bottom row).

Jamieson and Lippard [22] comprehensively reviewed cisplatin-DNA interactions and concluded that by far the most common DNA binding mode of cisplatin is to form 1,2-intrastrand cross links involving adjacent guanine bases. The formation of these cross links causes structural distortions to the DNA helix, with a 45-55° 'bending' of the DNA towards the major groove reported, along with an unwinding of around 79°. It has also been suggested that the binding of cisplatin prevents transcription factors from binding to DNA, and so this halts transcription [23]. But whilst cisplatin's binding to DNA has been extensively investigated and appears to be well understood, its cellular uptake and movement is still poorly explained.

It was thought that cisplatin entered cells by a simple passive diffusion mechanism, but more recent work had suggested copper uptake [24] and transporter proteins [25] play a role in cisplatin uptake. However, this hypothesis has now been dismissed although there is a correlation between elevated levels of the human copper transporter protein (also known as hCTR1) and cisplatin uptake [26].

Whilst the ability of the compounds shown in Figure 1.1 to bind extensively to DNA explains their effectiveness as cancer treatments, it is also the reason for their drawbacks. Their DNA binding nature, combined with their non-selective cellular uptake, means that all cells - cancerous and healthy - are subjected to their actions. Whilst obviously their apoptosis-inducing effects are welcome in cancerous tissue, this can be devastating in healthy tissue and their mutagenic effects can actually lead to secondary cancers forming. In addition there are many unpleasant side effects of cisplatin treatment, the most prevalent of which is nephrotoxicity - which was known to be severe enough as to be dose limiting as far back as 1975 [27]. The source of this toxicity is believed to be binding of platinum to sulphur containing protein residues in the proximal tubule in the nephrons of the kidney. To combat this, 'rescue agents' such as sodium diethyldithiocarbamate have been proposed to act as competitive sulphur containing binding sites for platinum. These compounds however have their own toxic side effects and so are of limited clinical use. It is also a common observation that whilst initial patient response to cisplatin is often positive, resistance to the drug is soon developed. Many mechanisms have been hypothesised for this acquired resistance including changes in cellular uptake mechanism and an increase in the rate of DNA repair.

Because of these side effects, vast amounts of resources are being focused on finding a new class of organometallic compounds which can bind to DNA in an entirely different way. As well as investigating new modes of binding, attention has also turned to looking at different metal centres to offer improved anti-cancer activity and budotitane became the first non-platinum based metal compound to enter clinical trials in 1996 [28]. Further titanium compounds have since been investigated [29] with compounds containing gold [30] and iron also being tested for anti-cancer activity. Modified versions of ferrocene showed great potential [31], however the two other metal based compounds that have entered clinical trials both contain ruthenium.

## 1.2 Ruthenium-based anti-cancer drugs

The two ruthenium based compounds that have entered clinical trials - imidazolium [trans-tetrachloro (dimethylsulfoxide)-imidazoleruthenate(III)], otherwise known as NAMI-A [32], and indazolium [transtetrachlorobis(1H-indazole)ruthenate(III)], KP1019 [33] - both contain a central $RuCl_4$ moiety, nitrogen-bound heterocyclic ligands and a corresponding protonated heterocyclic ligand counterion, and are shown in Figure 1.2. NAMI-A has recently completed Phase I/II clinical trials as a combination treatment with gemcitabline for patients with non-small-cell lung carcinoma. A decision on whether a new phase of clinical trials will begin will be made soon [34].

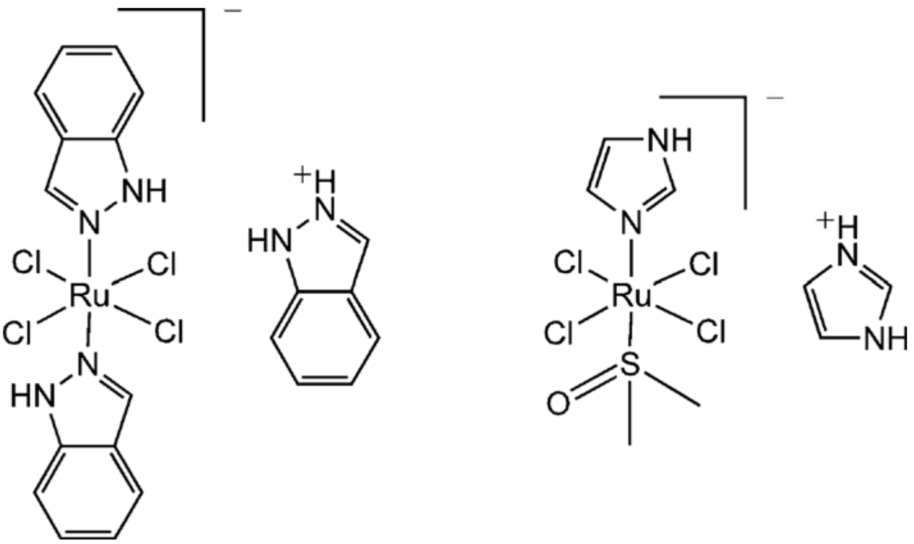

**Figure 1.2:** The chemical structures of the two ruthenium compounds that have entered clinical trials - KP1019 (left) and NAMI-A (right)

NAMI-A as suggested by its full name - New Anti-tumour Metastasis Inhibitor A - shows poor activity in primary tumours but has a potent effect on metastatic tumours. This mode of activity is due to NAMI-A's ability to bind to two mixed metallo-proteases, MMP2 and MMP9 [35]. Both of these enzymes have been implicated in the degradation of cellular collagen. By inhibiting these two enzymes the cell's viability is not compromised, but its ability to migrate is [36]. KP1019, which also contains a square-planar $RuCl_4$ central moiety, shows activity in a wide range of tumours. Ruthenium compounds attract attention due to a series of perceived advantages over platinum based compounds including;

- The accessibility of 2+, 3+ and 4+ oxidation states in physiological conditions.
- The formation of octahedral complexes which intuitively suggests a different action to square-planar platinum complexes.
- The ability of ruthenium compounds to behave as iron compounds do within the body and bind to proteins including transferrin.

As these compounds are relatively new, their mode of action and their uptake is still to de definitively determined. A comparison of KP1019 and its sodium analogue KP1339 show surprisingly marked differences in cellular uptake, localisation and toxicity [37]. KP1019 was found to remain predominantly within cellular cytoplasm whilst KP1339 was localised within cell nuclei; but KP1019 was found to be more cytotoxic. This supports the hypothesis that KP1019 is primarily active in a cell's mitochondria. Further studies on KP1019 and KP1339 support a hypothesis that they are both taken into cells by the transferrin pathway [33]. Tumour cells require large amounts of iron and so contain larger numbers of transferrin receptors than healthy cells. Transferrin is capable of binding two Fe(III) ions before being transported across the cell membrane. The concept of KP1019 binding to a protein to be transferred into cells is further supported by results from Phase I clinical trials which state that the concentration of ruthenium in plasma was 1000 times that found in the blood ultrafiltrate of patients, strongly suggesting that KP1019 is found almost exclusively bound to protein within the blood stream [33]. It is not however believed that KP1019 and NAMI-A's activity is due to nuclear DNA binding interactions. KP1019 is thought to interact primarily with mitochondria leading to depolarisation of the mitochondrial membrane, whereas NAMI-A's main effect is to disrupt interactions between the cell and the extracellular matrix. It has been shown to increase actin dependent cell adhesion and reduce cell invasiveness - leading to a less active form of cancer as opposed to cell death.

Whilst these two compounds clearly have different actions upon a cell, it is thought that both these compounds are actually pre-cursors to actual active species. A hypothesis of ‘activation by reduction’ has been proposed by Clarke [38] stating that the electrochemical potential of tumour cells is lower than that of healthy cells, promoting the reduction of Ru(III) to Ru(II). This change reduces the binding affinity of $\pi$-donor ligands (such as the nitrogen-bound heterocyclic ligands in KP1019 and NAMI-A) potentially giving the opportunity for these ligands to be substituted by cellular proteins.

Dyson *et al.* have exploited electrospray mass spectrometry to help determine the cellular fate of both KP1019 and NAMI-A, particularly in comparison to cisplatin. It was found that both ruthenium compounds formed fewer DNA adducts than cisplatin, but it was also noted that the adducts that were formed by KP1019 and NAMI-A were in a similar position to those formed by cisplatin. The ruthenium compounds also showed the same strong preference for guanine binding sites as exhibited by cisplatin and platinum based drugs oxaliplatin and carboplatin [39]. Further work has shown that the two compounds exhibit different effects upon cisplatin resistant cells - KP1019 was more cytotoxic to these cells, but it was NAMI-A that was found at increased levels and formed a higher number of DNA adducts when compared to its effect on cisplatin sensitive cells [40].

Whilst KP1019 and NAMI-A clearly show potential as anti-cancer compounds, they do not appear to lead to the novel DNA binding mode that may be needed to dramatically advance cancer therapy.

## 1.3 Novel DNA binding cylinders

Work within Hannon group has led to the development of supramolecular cylinders; tetracationic, triple helicate arrangements of the formula $[M_2L_3]^{4+}$ where M can be a variety of metals and L is a bispyridylimine ligand with a diphenylmethane spacer. L can be easily synthesised in good yields and when M is iron, the final cylinder structure can be synthesised in a simple reflux experiment without the need for further purification. The crystal structure of $[Fe_2L_3]^{4+}$ is shown in Figure 1.3(a).

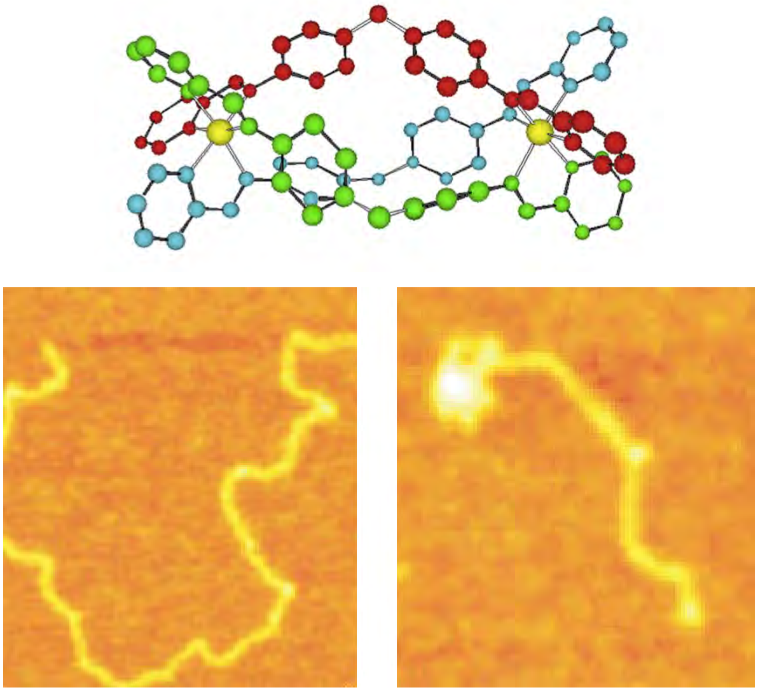

**Figure 1.3:** a) (top) - Crystal structure of $[Fe_2L_3]^{4+}$, with iron metal centres shown in yellow. Hydrogen atoms, counter ions and solvent molecules are omitted for clarity. b) (bottom) - Atomic Force Microscopy images showing the induced coiling of DNA plasmid following treatment with $[Fe_2L_3]^{4+}$. Image reproduced with permission from Figure 3 in [1]

As the cylinders are roughly the same size as zinc fingers (around 2nm in length and 1nm in diameter), it was hoped that these compounds would be able to bind in the major groove of B-DNA - and they indeed do with a binding constant of greater than $10^7$ $M^{-1}$. Atomic Force Microscopy images of calf thymus DNA (ct-DNA) following treatment with $[Fe_2L_3]^{4+}$ revealed an unexpected intramolecular coiling of DNA in much the same way as DNA coils around a histone [1]. Whilst this was a significant observation (as no other synthetic compound has been shown to have such an effect on DNA), a potentially far more exciting discovery was made when the crystal structure of $[Fe_2L_3]^{4+}$ with palindromic DNA revealed that the cylinder had crystallised at the centre of a three-way (Y-shaped) junction as shown in Figure 1.4(a).

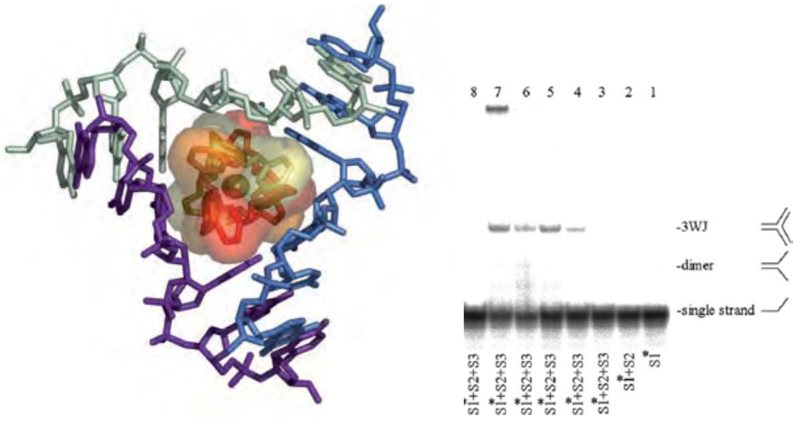

**Figure 1.4:** (a); Crystal structure of $[Fe_2L_3]^{4+}$-DNA complex, minor groove view. Image reproduced with permission from Figure 2 in [2]. (b); Autoradiogram of PAGE gel run at 25°C, showing the ability of $[Fe_2L_3]^{4+}$ to stabilise a DNA three-way junction. Lanes 1-3 contain control samples of strands of DNA alone, Lanes 4-7 contain all three strands of DNA with increasing concentration of $[Fe_2L_3]^{4+}$ and Lane 8 contains a control sample of all three strands with 10 mM $MgCl_2$. Increasing cylinder concentration lead to DNA precipitation (observed in Lane 7), not increasing formation of three-way junction. Image reproduced with permission from Figure 3 in [3].

This mode of binding had never been observed before, and so was further investigated using poly acrylamide gel electrophoresis (PAGE), shown in Figure 1.4(b). This work confirmed that this binding mode was not just an artefact of the crystallisation process, but $[Fe_2L_3]^{4+}$ was in fact able to stabilise a three-way junction. The significance of this binding location is vast - Y-shaped junctions are formed during one of a cell's most important processes; replication. If the cylinder can bind in a three-way junction in a cellular environment and block DNA replication, this would offer a possible explanation for any exhibited cytotoxic effects. This new mode of DNA binding combined with their DNA coiling ability, gives these cylinders two novel interactions with DNA. As discussed earlier, novelty is a much sought after quality for DNA binding compounds, and so an extensive study of the effect of $[Fe_2L_3]^{4+}$ on five cell lines was undertaken.

$[Fe_2L_3]^{4+}$ was shown to reduce mitochondrial activity, inhibit cell proliferation and induce apoptosis at remarkably low concentrations - 7 μM of cylinder was enough to completely arrest cell growth in the SKOV-3 ovarian cancer cell line and to significantly reduce growth in HBL-100 (breast cancer) and MRC5 (healthy lung) cell lines. The Ames and Comet assays were used to determine the mutagenic and genotoxic-potential of the cylinder. The Ames assay utilises bacteria which carry mutations meaning they are unable to produce histidine. These are treated with the compound of interest and then grown in a histidine-free medium. If the compound has mutagenic properties, the initial mutations will be reversed and allow colonies to grow in the histidine-free medium. The Comet assay uses gel electrophoresis on lysed cells which have been treated with the compound of interest. If the compound has a genotoxic effect, a large number of DNA strand breaks will be observed causing the formation of a comet-shaped tail following electrophoresis. It was perhaps the most significant finding in this study that the cylinder was able to induce cytotoxic effects without exhibiting mutagenic and genotoxic effects [41].

These results combine to make these cylinders an excellent potential lead molecule for cancer therapy - they bind to DNA in a novel mode leading to cell death, but without exhibiting some of the toxic side effects that have plagued the traditional platinum-amine drugs currently in clinical use.

As discussed earlier, these cylinders may contain a variety of metals and a ruthenium analogue ($[Ru_2L_3]^{4+}$) has also been synthesised [4]. Unlike KP1019 and NAMI-A, $[Ru_2L_3]^{4+}$ contains Ru(II), not Ru(III). As it is believed KP1019 and NAMI-A are only active once reduced to Ru(II), it was hoped that starting with a Ru(II) compound combined with the cylinder structure would give a very promising anti-cancer target compound. The crystal structure of the ruthenium cylinder is shown in Figure 1.5.

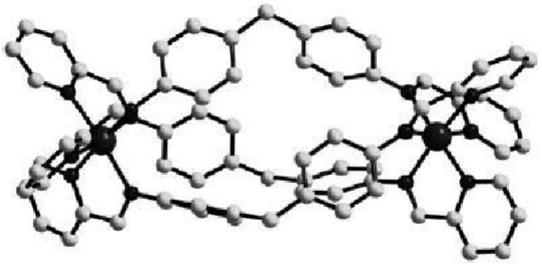

**Figure 1.5:** Crystal structure of $[Ru_2L_3]^{4+}$, with ruthenium metal centres shown as large black spheres. Hydrogen atoms, counter ions and solvent molecules are omitted for clarity. Image reproduced with permission from Figure 1 in [4].

The synthesis of the Ru cylinder is much more problematic than that of the Fe cylinder. It requires a 5 day reflux reaction and a time consuming purification process. However, cytotoxic studies on this compound show that the more difficult synthetic procedure is worth pursuing. $[Ru_2L_3]^{4+}$ has been shown to possess $IC_{50}$ values for HBL-100 and T47D breast cancer cell lines which are only 2-5 times lower than that of cisplatin [4]. However, of equal interest was the finding that $[Ru_2L_3]^{4+}$ is inactive against SKOV-3 cells when just 7uM of $[Fe_2L_3]^{4+}$ has been shown to completely arrest their proliferation [42]. This gives the first indication that the SKOV-3 cells are showing selective uptake of the cylinders based on their metal centres. If there is any way that these cylinders could be tailored so that they are selectively taken up by one cell type over another, and in particular differentiating between healthy and cancerous cells, this would clearly represent a major breakthrough in the design of cancer therapies.

$[Ru_2L_3]^{4+}$ has also been shown to have the ability, unlike $[Fe_2L_3]^{4+}$, to induce single-strand breaks in DNA following irradiation with visible or UV light, mainly at guanine bases due to the production of singlet oxygen [43]. This opens up the possibility of investigating the ruthenium cylinder as a potential photodynamic therapy agent. $[Ru_2L_3]^{4+}$ has also been shown to prevent the binding of the taq-polymerase enzyme to DNA, suggesting that the cylinders can effectively block DNA replication by sitting at the replication fork [44].

The cytotoxic potential of these supramolecular cylinders is clear but work in this area must now concentrate on determining their cellular uptake mechanism and localisation to determine if the DNA binding observed in solution is replicated in a cellular environment. The first work aimed at determining the cellular localisation used Inductively Coupled Plasma Mass Spectrometry (ICP-MS) [42]. HL-60 blood cells treated with ruthenium cylinder were lysed and centrifuged to separate into nuclei and cell cytosol. A control experiment using cisplatin was also prepared. As ruthenium and platinum are not naturally found within human cells, all traces of these metals found within cells must be attributable to $[Ru_2L_3]^{4+}$ or cisplatin. Using ICP-MS it was found that over 80% of the available ruthenium was taken into the cells and nearly 85% of the ruthenium found within cells was found in the nuclei. This compares favourably with ciplatin where just a third of the platinum found within cells was found with the nuclei. This result suggested two things, firstly that the ruthenium cylinder localises within the nucleus and that it may be actively transported into the cell.

However it cannot be said for certain that the ruthenium enters the nucleus (or indeed the cell) as intact cylinder. Therefore there is a need to supplement assay and DNA solution studies by tracking the cylinder's fate within a cellular environment.

## 1.4 The cellular imaging of metallo-drugs

### 1.4.1 The advantages of imaging drugs *in vivo*

Whilst there are many assays that can be performed to try and determine the action of any compound upon a cell, each assay may only allow for one particular enzyme or cell organelle to be studied. For example, the Ames test will determine if any mutagenic effects are produced, the Comet assay will show the level of DNA damage caused and an MTT assay can be used to determine the viability of cells, by measuring a cell's ability to metabolise the yellow MTT salt to a purple formazan. Using this approach means that it difficult to appreciate all the effects a compound may have upon a cell. However, there are a wide variety of imaging techniques that can be utilised that allows the user to look at multiple effects at once - for example, phase contrast microscopy can be used to observe a compound's effects on cell morphology and motility. There are also multiple applications for fluorescence microscopy - structures within a cell can be fluorescently labelled to gain information about the compound's effects on those structures, or if the compound has fluorescent properties its cellular localisation can be determined. Imaging also has the potential to improve the screening of potential drug candidates by allowing the *in vitro* investigation of effects which are currently being studied *in vivo* at a great financial and time cost - a prominent example of this is the micronucleus assay. This assay detects cells that have suffered chromosomal damage which leads to some chromosomes being unable to separate effectively during the anaphase segment of cell division. Traditionally the assay has been performed by examining the bone marrow of mice which have been treated with a drug candidate compound [45]. This scale of testing requires grams of the compound and it will be performed relatively late in the clinical trial process as, in line with ICH M3(R2) (which is followed by the European Medicinal Agency and US FDA) this *in vivo* genotoxicity testing is not required before the first human trial [46]. However, by staining the nuclei of a population of cells *in vitro* as shown in Figure 1.6, the formation of any micronuclei can by observed using milligrams of compound, and as an *in vitro* test, can be performed early on during compound screening, potentially as a complement to other genotoxic tests such as the Comet assay [5].

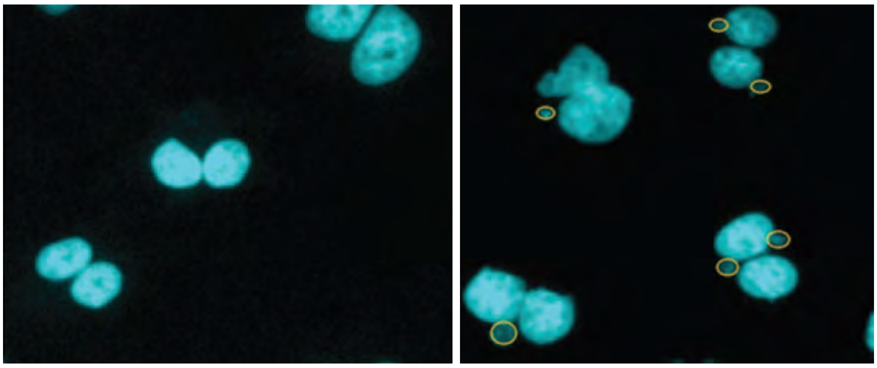

**Figure 1.6:** Cultured cells with nuclei stained with fluorescent dye - control sample (left) showing healthy nuclei and treated sample (right) showing the presence of micronuclei, highlighted in yellow circles. Image reproduced with permission from Figure 3 in [5].

Cellular uptake can also be studied by a variety of techniques, such as ICP-MS as discussed earlier. Barton *et al.* have employed a variety of techniques to determine the uptake mechanism of a series of ruthenium compounds [47][6], which are shown in Figure 1.7. Several techniques such as temperature controlled experiments, metabolic inhibition, transporter inhibition and membrane potential modulation *all* followed by analysis by flow cytometry were employed to determine the mechanism of cellular uptake. After testing several inhibitors, it was concluded that the compound entered by passive diffusion.

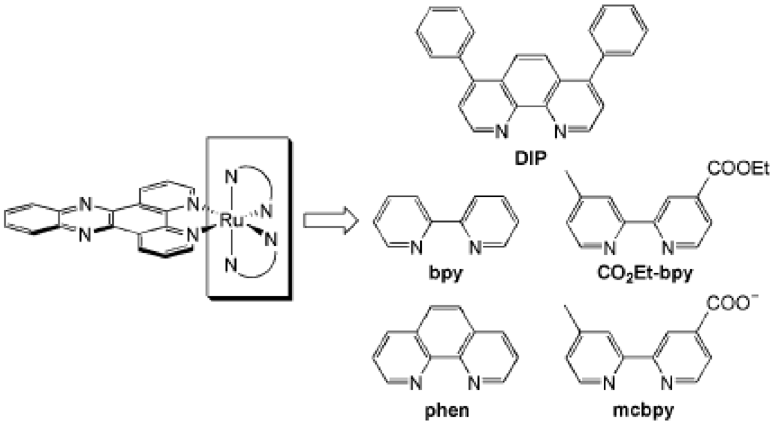

**Figure 1.7:** Structures of ruthenium compounds investigated by Barton *et al.*, image reprinted with permission from [6].Copyright 2007 American Chemical Society.

Whilst these experiments are of course perfectly valid and give a reliable conclusion, if the samples had been imaged instead of being analysed by flow cytometry there was the potential to obtain a huge amount of extra information. Information such as; did any of the inhibitors used actually lead to a delayed uptake of the compound, or did the modulation of the membrane potential lead to localisation of the compound in a different cell organelle than before?

As reviewed in detail by Watson *et al.* [48], there a variety of compounds that can be used to label transporter proteins or the endosomes formed during endocytotic uptake of compounds. Therefore simple co-localisation experiments can be performed to determine the uptake mechanism of the compound. In particular, events at the cell membrane can be studied in great detail using the technique of Total Internal Reflection (TIRF) microscopy.

A traditional argument against the use of imaging is the throughput rate of samples - it can be argued that the imaging of compounds within cells may be so slow it negates any benefits obtained from analysing compounds in this way. However the development of commercial systems to allow for the high throughput of multi-well plates has dramatically increased the number of samples that can be analysed within a given time frame [49], and so provides the possibility for imaging techniques to be a real option for investigating potential drug candidates.

### 1.4.2 The cellular imaging of currently used metallo-compounds

There have been attempts to image the cellular localisation of cisplatin by the addition of a fluorophore [50] [7] [8], or by the formation of fluorescent nanoparticles with an outer coating of cisplatin [51]. Some images taken from [7] and [8] are shown in Figure 1.8. These papers all reported observable fluorescence of their cisplatin based compounds. The fluorophore-tagged cisplatin compounds used in [50], [7] and [8] were also between them studied for co-localisation with lysosomes and Golgi bodies showing again how the imaging of compounds within cells can be used to gather information quickly that may not be easily obtainable from assays.

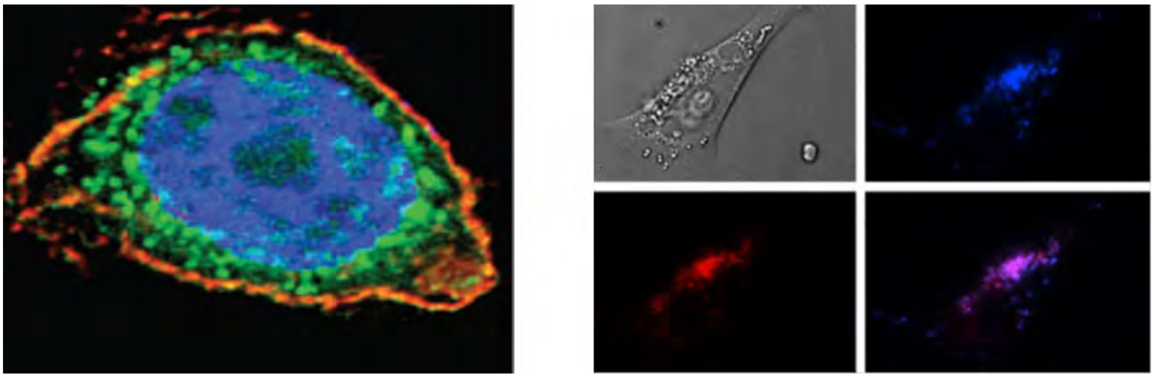

**Figure 1.8:** Left - ovarian cancer cell treated with fluorscein tagged cisplatin (green), and then stained with Alexa Fluor 647 phalloidin (red) to identify actin, and Hoechst 33342 to stain the nucleus. Image reproduced with permission from Figure 2 in [7]. Right - Ovarian cancer cell treated with an anthracene tagged cisplatin, shown in blue and stained with LysoTracker Red to determine localisation of lysosomes. The overlay of these images is shown in bottom right. Images reproduced with permission from Figure 5 in [8]. Both examples suggest the fluorophore-tagged cisplatin is localised in vesicles as opposed to being spread throughout the cytoplasm.

The addition of a fluorphore to a potential drug candidate is a useful technique for imaging its localisation but this now represents an ‘unknown variable’ as the compound being imaged is not the same compound that would be used clinically. If however the compound of interest possesses an inherent fluorescence, cellular imaging can add another dimension of understanding to its cellular uptake and localisation.

### 1.4.3 The cellular imaging of ruthenium-based compounds

As discussed in detail in Section 2.2, the cylinder with the most potential to be used as part of fluorescence imaging studies is the ruthenium cylinder. The is due to the $d^6$ ruthenium centres found within this compound - combinations of $d^6$ metals with high field ligands such as 2,2’-bipyridine or 1,10-phenanthroline lead to compounds with large Stokes shifts and good quantum yields. There are many reported examples of $d^6$ transition metal complexes being investigated as fluorescent probes, but this discussion will focus on ruthenium compounds. The most widely studied ruthenium compound is $[Ru(bpy)_3]^{2+}$.

$[Ru(bpy)_3]^{2+}$ has unusual photophysical properties which make it an attractive compound to study. The absorption spectrum shows an MLCT centred at 450nm, and excitation at this wavelength leads to a triplet excited state. So relaxation and interconversion back to the singlet ground state configuration is slow, giving $[Ru(bpy)_3]^{2+}$ an unusually long fluorescence lifetime in the order of 1μs [52]. $[Ru(bpy)_3]^{2+}$ also has an exceptionally high fluorescence yield of over 0.9 [53]. The combination of these two properties has lead to attention focusing on other $Ru\text{-}N_6$ chromophores in the hope of finding other compounds with attractive photophysical properties.

There are two possible uses for fluorescent ruthenium compounds; either as imaging probes or to track the cellular localisation of potential cytotoxic compounds. The use of ruthenium compounds as DNA probes has been investigated since the first discovery of so called ‘light switch’ compounds. These compounds, again predominantly containing $d^6$ octahedral metal ions undergo an MLCT upon excitation only when they are bound to DNA. The first compound shown to behave in this way was $[Ru(bpy)_2(dppz)]^{2+}$ [54]. The source of this fluorescence is unclear, but the intercalation of $[Ru(bpy)_2(dppz)]^{2+}$ allows for overlap between the phenazine rings and the DNA bases offering an alternative decay mechanism to the protonation of the phenazine seen when $[Ru(bpy)_2(dppz)]^{2+}$ is excited in aqueous solution.

Thomas *et al.* have used a dinuclear ruthenium compound to selectively label breast cancer cells [9]. Their compound contains two $Ru(phen)_2$ moieties linked by a tetrapyridophenazine group - $[(phen)_2Ru(tpphz)Ru(phen)_2]^{4+}$. This compound is non-emissive in water, but emits at 660nm following binding to DNA [55]. High magnification imaging of cells treated with this compound has produced images of individual chromosomes, and lambda stacking experiments during live cell imaging have shown that this compound can actually distinguish between duplex and non-duplex DNA. Excitingly, Thomas *et al.* have also discovered they can target mitochondrial DNA by changing the delivery mechanism of $[(phen)_2Ru(tpphz)Ru(phen)_2]^{4+}$ [10]. By encapsulating the compound in a polymer vesicle that is only broken down within the acidic endosomes, the ruthenium compound is released into the cytoplasm, and then preferentially locates within mitochondria. This raises interesting questions about why the compound should localise within the mitochondrial DNA as opposed to nuclear DNA, and suggests that when treated with free, unencapsulated compound cells actively transport it into the cell and then into the nucleus.

Figure 1.9 shows a collection of images of $[(phen)_2Ru(tpphz)Ru(phen)_2]^{4+}$ localised to both nuclear and mitochondrial DNA.

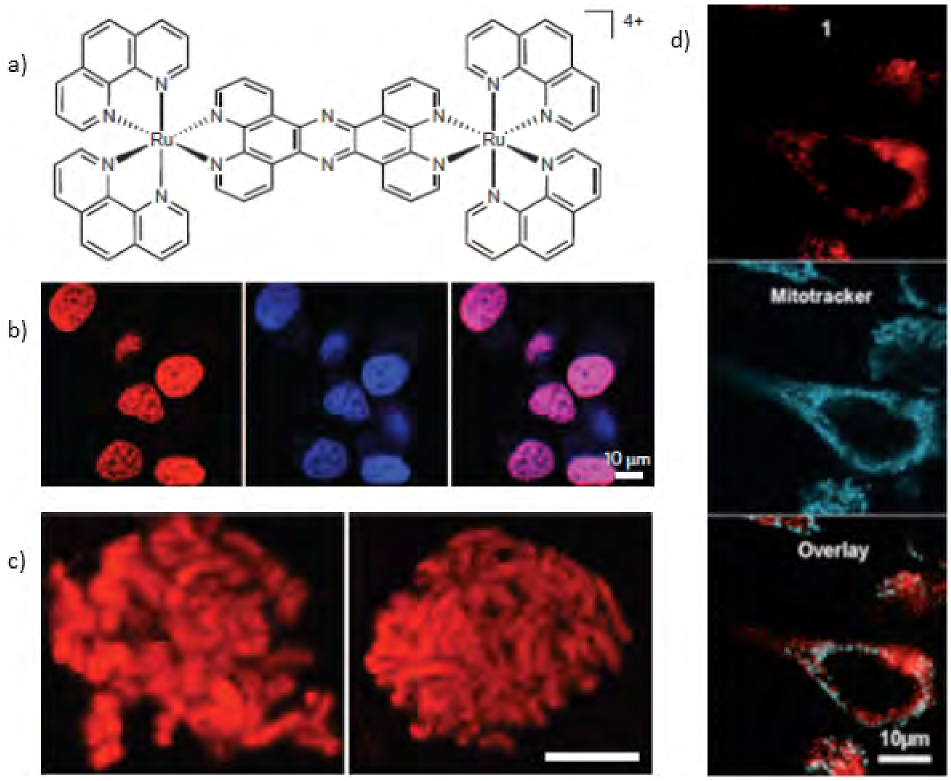

**Figure 1.9:** a) The structure of $[(\text{phen})_2\text{Ru}(\text{tpphz})\text{Ru}(\text{phen})_2]^{4+}$. b) Fluorescence confocal microscopy images of $[(\text{phen})_2\text{Ru}(\text{tpphz})\text{Ru}(\text{phen})_2]^{4+}$ in MCF-7 breast cancer cells (red), nuclear DNA stain DAPI (blue) and overlay of two images showing co localisation of the two following treatment with $[(\text{phen})_2\text{Ru}(\text{tpphz})\text{Ru}(\text{phen})_2]^{4+}$ in media solution. c) High magnification of mitotic cells showing individual chromosomes. d) Images of $[(\text{phen})_2\text{Ru}(\text{tpphz})\text{Ru}(\text{phen})_2]^{4+}$ in MCF-7 breast cancer cells (red), mitochondrial DNA stain Mitotracker Red (blue) and over lay of two images, showing co-localisation of the two following treatment with $[(\text{phen})_2\text{Ru}(\text{tpphz})\text{Ru}(\text{phen})_2]^{4+}$ encapsulated in polymer vesicles. Images (a-c) reproduced with permission from Figure 4 in [9], image (d) reproduced with permission from Figure 2 in [10].

As well as using using luminescent compounds and investigating their DNA binding properties, a strategy of attaching a luminescent ruthenium moiety to compounds which are already known to bind to cellular targets. This approach has been exploited by Turro *et al.* who linked an Ru-$N_6$ centre to an ethidium moiety which is known to intercalate between DNA bases [11]. The resulting compound known as RuEth, shown in Figure 1.10 was spectroscopically shown to increase in fluorescence intensity when bound to RNA, and when breast cancer cells were incubated with RuEth, areas of high fluorescence intensity were observed in the cell nucleolus where ribosomal RNA is synthesised.

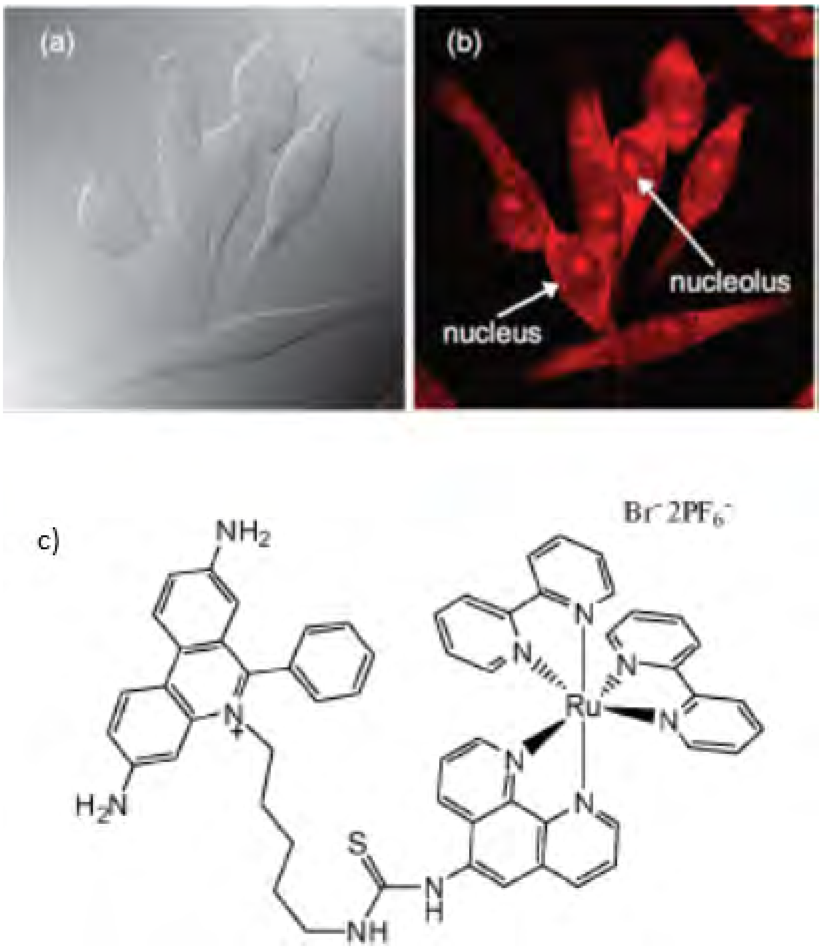

**Figure 1.10:** a) Brightfield image and b) Fluorescence confocal microscopy images of MCF-7 cells treated with RuEth showing localisation of RuEth within the nucleolus. c) Structure of RuEth. Images (a-c) reproduced with permission fro Figure 5 from [11].

Following on from work developing $[Ru(bpy)_2(dppz)]^{2+}$ DNA ‘light switch’, the Barton group have produced a series on papers detailing the imaging of ruthenium compounds within cells. A library of ruthenium dipyridophenazine (dppz) complexes were prepared with $[Ru(dip)_2(dppz)]^{2+}$ (where dip = diphenyl phenanthroline) shown to significantly increase luminescence of HeLa cells treated with the compound, as shown by flow cytometry [6]. Cellular imaging of this compound shows fluorescence located predominantly within the cytoplasm. This work was taken forward by the synthesis of RuRrRk - a ruthenium compound with phen, dppz and a modified bpy ligand. The bipyridine ligand links the ruthenium centre to a 4-peptide long conjugate, RrRK (R = L-arginine, r = D-arginine and K = L-lysine). Flow cytometry again showed that the compound behaves in a ‘light switch’ manner, and when incubated with HeLa cells areas of fluorescence within the cell nucleus were observed [12]. Structures of the compounds used by Barton *et al.* and images of them within HeLa cells are shown in Figure 1.11.

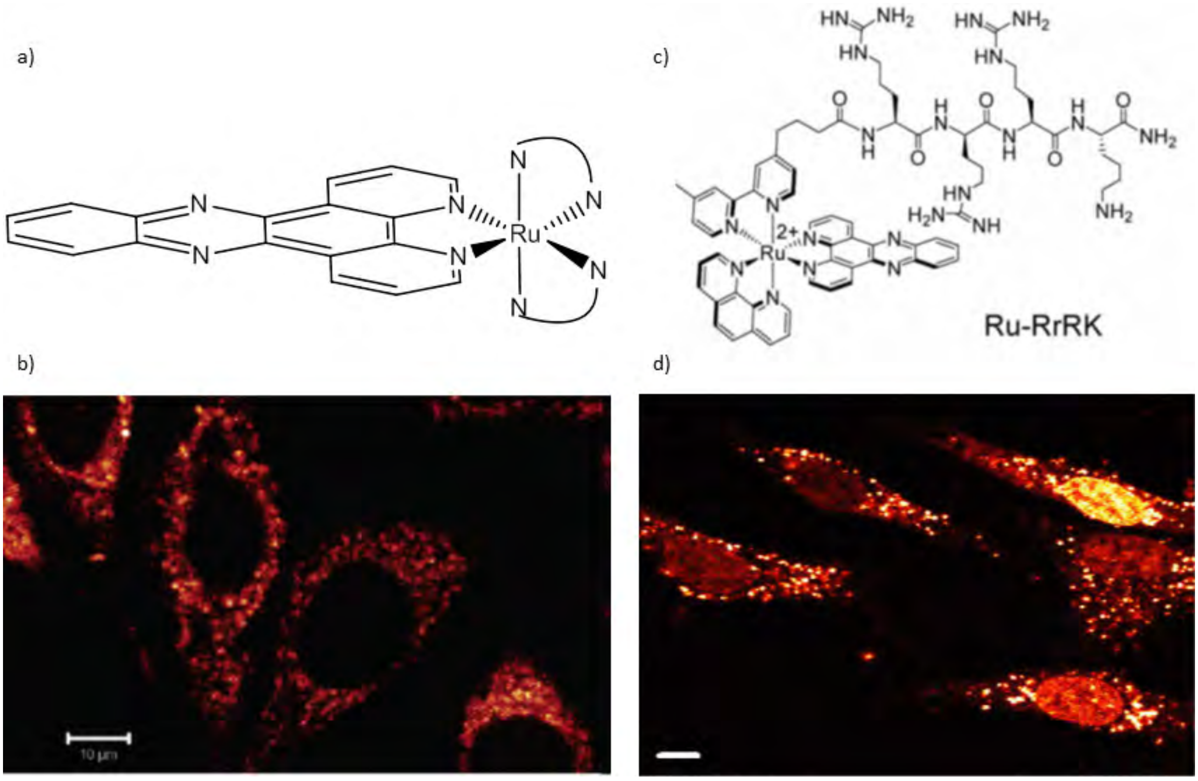

**Figure 1.11:** a) Structure of $[Ru(dip)_2(dppz)]^{2+}$, where N-N is diphenyl phenanthroline. b) Fluorescence confocal microscopy images of HeLa cells treated with $[Ru(dip)_2(dppz)]^{2+}$ showing fluorescence spread throughout the cytoplasm. c) Structure of RuRrRK. d) Image of HeLa cells treated with RuRrRK, with fluorescence now observed within the cell nucleus. Images (a-b) reproduced with permission from Figure 3 in [6], images (c-d) reproduced with permission from Figure 2 in [12].

Very recent work from Lin *et al.* has profiled three ruthenium based compounds for their cytotoxic activity and used fluorescence confocal microscopy to confirm that all of these compounds localise with the nucleus of liver cancer cells [56]. As discussed in Section 1.4.1, the Barton group have investigated the uptake mechanism of their compounds, but it is only from imaging studies that the full cellular localisation of the compounds have been determined.

Ruthenium compounds show great potential as anti-cancer drugs, due to their entirely different interactions within cells when compared to traditional platinum drugs. Ru-$N_6$ compounds also have a variety of applications as imaging probes and so combining a potential drug candidate with the advantages of being imaged within cells represents a great opportunity to fully explore its cellular action.

## 1.5 The aims of this work

This work therefore had two aims;

- The primary aim of this work was to use imaging techniques to attempt to determine the cellular localisation of our supramolecular cylinders to determine if the DNA binding properties of the cylinders shown in solution are replicated in a cellular environment. Several fluorescence microscopy techniques were planned such as live cell imaging to track fluorescent compounds, as well as co-localisation studies with cellular dyes.
- The secondary aim was to also image the effects these compounds have on a variety of cell lines, initially to look at and investigate any changes in morphology and motility.

# Chapter 2

# The synthesis and spectroscopic properties of novel DNA binding fluorescent cylinders

## 2.1 Previously synthesised cylinders

As discussed in Section 1.3, the cylinders can be synthesised to contain a variety of metal centres. However, not all of these cylinders are suitable for imaging studies due to their spectroscopic properties. The absorption spectra of cylinders containing iron and zinc are shown in Figure 2.1. These spectra reveal that the Zn cylinder has no excitable transitions within the visible range of light. Whilst there are absorption bands within the UV region, exciting at these wavelengths is not suitable during the live cell imaging that is required to complete the aims of this work.

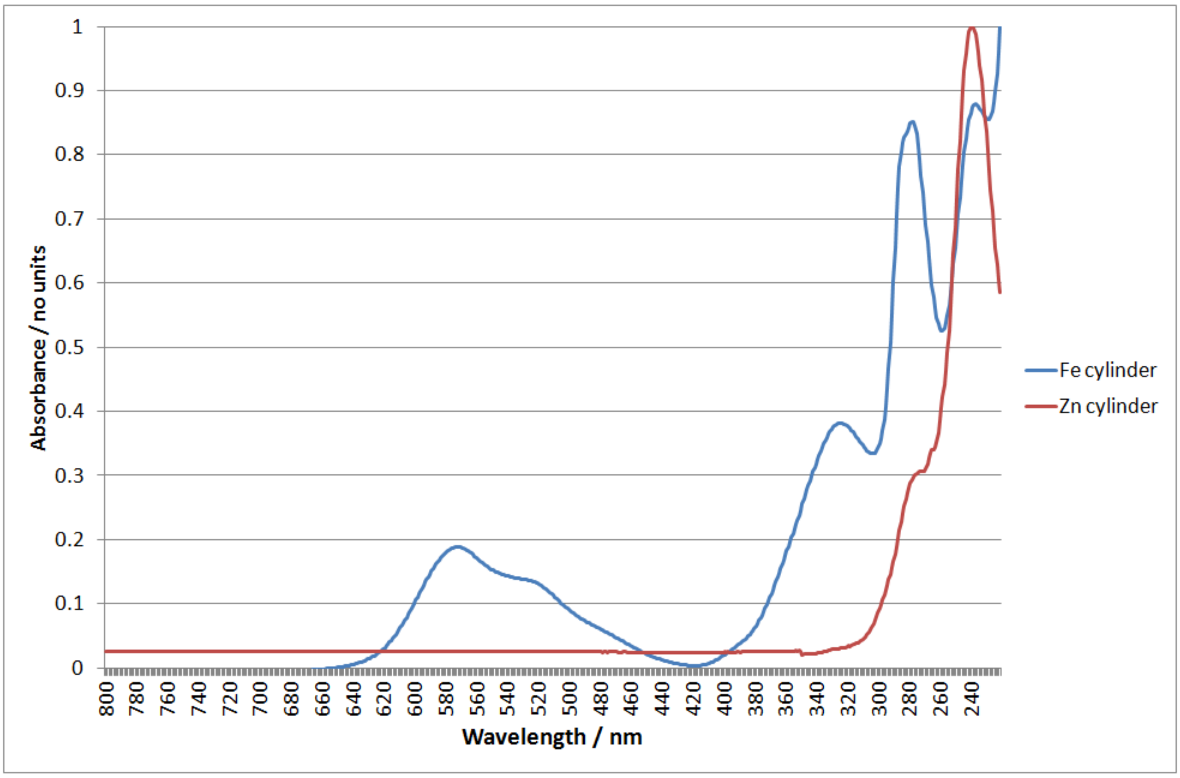

**Figure 2.1:** Absorption spectra of Fe and Zn cylinders in the range of 220-800 nm, both spectra have been normalised to one at the point of maximum absorption to allow for comparability. The spectra show that the Fe cylinder has its maximum absorption at 572nm, caused by a metal to ligand charge transfer, whilst the Zn cylinder has no observable absorption within the visible range, making it unsuitable for cellular imaging studies.

The absorption spectrum of Fe cylinder shows a metal-ligand charge transfer (MLCT) with a maximum at 572nm. For the purpose of imaging studies, it is the MLCT transition which would ideally be used to determine the localisation of the compound, as this confirms that the cylinder structure is still intact. The closest commercially available laser line is the 568nm line, produced either by a krypton/argon gas laser or by a solid state sapphire laser. Unfortunately neither of these were readily available, so it was not considered possible to pursue the fluorescence imaging studies of $[Fe_2L_3]^{4+}$. As well as the attractive toxicology properties of ruthenium compounds, it was decided that using the ruthenium cylinder offered the best opportunity to complete cell fluorescence imaging studies, and so work began on improving the synthetic protocol of $[Ru_2L_3]^{4+}$.

## 2.2 Improving synthetic protocols for Ru cylinder

The synthesis of $[Ru_2L_3]^{4+}$ was first published in 2007, and briefly comprises a 5-day reflux of $Ru(DMSO)_4Cl_2$ and ligand in ethylene glycol at 200°C under a nitrogen atmosphere [4]. An extensive purification protocol of alumina column chromatography was utilised to obtain pure compound, however the reported yield was just 0.3%, with the main impurities being polymeric or double stranded species. Whilst work within the group has led to a more effective purification protocol using silica column chromatography [57], the initial synthesis stage is still time consuming, and often leads to such large excesses of by-products that the amount of compound that can be isolated is so small it cannot be fully characterised, meaning it is often better to start again. Due to the broad peaks observed in the $^1H$ NMR spectrum and *m/z* values seen in ESI-MS spectra of crude reaction product, it is believed that the major product is a $d^5$ low spin Ru(III) double stranded cylinder. This suggests that once the double stranded compound or polymer side products are formed, the reflux conditions aren't strong enough to force the reaction to completion and form the triple stranded cylinder which led to a search for a more efficient synthesis, as presented below. It is noted at this point that as the published protocol does not always lead to a successful outcome, all synthetic attempts using non-published protocols were repeated on several occasions before determining if the new protocol was worth pursuing.

The first strategy considered for improving Ru cylinder synthesis was to consider the starting materials used. The synthetic route for the synthesis of the ligand is well established and $^1H$ NMR analysis of all ligand batches synthesised showed no unassigned peaks. It was therefore determined that this synthetic route could not be improved upon. Attention was therefore turned to the other starting material, $[Ru(DMSO)_4Cl_2]$. The synthesis of cis-$[Ru(DMSO)_4Cl_2]$ was first described in [58], and involves refluxing $RuCl_3 \cdot 3\,H_2O$ in a molar excess of DMSO. As the final compound contains no protons suitable for $^1H$ NMR analysis, characterisation of the compound relies on ESI-MS or crystallography studies. A literature review for the synthesis of $[Ru(DMSO)_4Cl_2]$ revealed that the only deviation from Evans' originally published route were variations in the length of time spent refluxing the materials, but this did not lead to a significant increase in reported yields. It was however noted that some authors included a step to recrystallise crude [Ru(DMSO)$_4$Cl$_2$] from DMSO solvent [59]. This was therefore performed by dissolving crude [Ru(DMSO)$_4$Cl$_2$] in the minimum volume of hot DMSO solvent to give a deep red solution, anticipating that yellow [Ru(DMSO)$_4$Cl$_2$] would form upon allowing the solution to cool to room temperature. Initial attempts led to no crystallisation being observed, and so the [Ru(DMSO)$_4$Cl$_2$] was re-precipitated using acetone and then isolated using filtration and allowed to dry *in vacuo*. However the isolated product was orange in colour and so this was discarded as it was clear that the product was contaminated with other ruthenium species. Following attempts concentrated on encouraging crystallisation, regardless of the size of crystals obtained. Therefore syntheses were performed whereby the solution was immediately either refrigerated at 5°C, or immersed in an ice bath. Whilst crystals were duly observed under both of these conditions, the high boiling point of DMSO (189°C) means that DMSO does not evaporate under atmospheric conditions. Even under a vacuum, it was not possible to remove all the DMSO solvent and so the resulting crystals were filtered and then allowed to dry *in vacuo*. As with the crude material, the crystals were characterised using ESI-MS and were confirmed to contain [Ru(DMSO)$_4$Cl$_2$], but as ESI-MS is a qualitative and not quantitative technique, it cannot be determined if the re-crystallisation process had increased the purity of the final [Ru(DMSO)$_4$Cl$_2$]. The recrystallised [Ru(DMSO)$_4$Cl$_2$] was then used in attempted syntheses of Ru cylinder using the published protocol, but all syntheses resulted in the formation of a dark red solution; a tell tale sign that the predominant reaction product was double stranded cylinder. From these results, it was shown that the recrystallisation of [Ru(DMSO)$_4$Cl$_2$] did not lead to a more effective synthetic route and so this was not pursued further.

It was perhaps to be expected that refinement of the synthesis of the cylinder starting materials would not lead to a significant improvement of cylinder yield - the starting material contains ruthenium in a d$^6$ low spin configuration and so is classically inert, meaning large amounts of energy are needed to cause the Ru(DMSO)$_4$Cl$_2$ to react. Experience within the lab led to the observation that the synthesis of [Ru$_2$L$_3$]$^{4+}$ often gave higher yields if the oil bath used in the reflux synthesis was pre-heated to 200°C before the reaction vessel was immersed, instead of starting the reaction at room temperature. The apparent need for immediate high energy meant that utilising microwave synthesis seemed a logical route to investigate. Traditional heating methods, such as the oil bath, led to a temperature gradient developing within the reaction vessel as the heat is transferred from the oil to the vessel, then from the vessel to the solvent and reagents. Using microwave energy instead causes dielectric heating to take place, which gives rapid, uniform heating throughout the entire vessel. The heating is rapid if appropriate microwave transparent glassware is used delivering the energy directly to the reagents, and uniform if the cavity containing the vessel is designed so that the radiation reflects from the walls of the cavity to the vessel used. No contact between the vessel and the energy source is required [60]. There are several examples of microwave chemistry being used to synthesise novel ruthenium compounds, or to improve the yield or reaction time required of previously synthesised compounds [61, 62, 63], and in 2008 Glasson *et al.* described the synthesis of a ruthenium triple helicate using microwave irradiation; with a reported yield of 36% [64]. It was therefore hoped that the use of microwave energy along with an improved purification process would lead to a greatly improved yield.

All microwave work was performed using a Discovery System machine (CEM, USA), which uses sealed vessels with a recommended total volume of 20 ml. This meant that all aspects of the reaction needed to be considered both to design a successful synthetic protocol and to prevent damage to the instrument. Solvents interact with microwaves based on their polarity - non-polar solvents such as toluene and hexane are transparent to microwaves and so a polar solvent must be used. As discussed earlier, the Ru cylinder synthesis requires a large amount of energy to the activation barrier, and so a high reaction temperature was required. Whilst one advantage of using microwave synthesis is that it can allow a solvent to reach a higher temperature than it would do under reflux conditions, the microwave requires a closed reaction system so further consideration was given to the vapour pressure that would be generated by each solvent at a temperature of 200°C. The microwave used can operate up to a maximum pressure of 435 psi, so any solvent with a vapour pressure above this at 200°C was immediately ruled out for investigation. Using the Antoine equation as shown below, and parameters as taken from [65] and [66], the vapour pressures of available solvents at 200°C were calculated as included in the Table 2.1.

$$\ln P = A - \frac{B}{T + C}$$

**Table 2.1:** Table showing the Antoine parameters for six selected solvents, and their calculated expected vapour pressure. Note that for DMSO, the parameters quoted require temperature (denoted as T in Equation above) to be given in degrees Kelvin, and so is taken as 473K. For all other solvents, temperature is given in degrees Celsius.

| **Solvent** | **A** | **B** | **C** | **Expected Vapour Pressure at 200°C / psi** |
|---|---|---|---|---|
| Water | 16.3872 | 3885.70 | 230.170 | 226.7 |
| Methanol | 16.5785 | 3638.27 | 239.500 | 583.8 |
| Ethanol | 16.8958 | 3795.17 | 230.918 | 472.4 |
| Acetonitrile | 14.8950 | 3413.10 | 250.523 | 218.8 |
| DMSO | 15.8617 | 4717.40 | 41.5900 | 117.2 |
| Ethylene Glycol | 15.7567 | 4187.46 | 178.650 | 15.9 |

This analysis showed that common solvents such methanol and ethanol were unsuitable for use in this protocol, but it also revealed that the estimated vapour pressure of DMSO is 117.2 psi at 200°C. Whilst this is within the acceptable range to use within the microwave, it is known that DMSO decomposes under microwave irradiation into gaseous species [67], which can lead to pressure building up within the system. This meant that the favoured starting material - $Ru(DMSO)_4Cl_2$ - was no longer suitable to be used in this synthesis. $RuCl_3 \cdot xH_2O$ was therefore used, in a 2:3 ratio with ligand and heated to 225°C in ethylene glycol for 4 hours, following Glasson *et al.*'s procedure. This however led to a large pressure build up within the system and the reaction could not be safely controlled under these conditions. With Glasson *et al.*'s procedure used as a starting point, work was performed to develop a suitable protocol for Ru cylinder synthesis.

For each set of conditions tested as part of this work, the crude reaction mixture was worked up in line with published protocol [4] by adding it to a saturated aqueous solution of $NH_4PF_6$, and then re-precipitating from acetonitrile using diethyl ether. This crude material was then subjected to $^1$H NMR and ESI-MS analysis to determine if the material contained any $[Ru_2L_3]^{4+}$; if no cylinder was identified at this stage the sample was discarded and a fresh synthesis was prepared. $[Ru_2L_3]Cl_4$ is easily characterisable using mass spectrometry due to the unique isotope pattern of ruthenium, with seven stable isotopes observable. The full characterisation of $[Ru_2L_3]Cl_4$ is given in section 6.3.2. To prevent instrument damage, further syntheses performed on the microwave were set to limit pressure to 70 psi (4.8 bar), as this is well below the expected vapour pressure for ethylene glycol at 200°C and also well within the recommended guidelines for using this instrument. Should this pressure limit be reached, the microwave will stop heating the reaction until the pressure has decreased below this limit. As initial attempts were focused on determining if Ru cylinder was formed under the selected temperature and pressure conditions, only small quantities of starting materials were used with the aim of scaling up quantities once suitable conditions had been found. Therefore 0.4 mmol of $RuCl_3 \cdot xH_2O$ and 0.6 mmol of ligand were combined in 20 ml of ethylene glycol and heated to 180°C, using 260W for 4 hours. It was noted that the pressure within the reaction vial increased to 70 psi, at which point the temperature of the system was 170°C. This showed that these conditions were either generating a gaseous species, or the solvent was contaminated with another solvent with a higher vapour pressure at 180°C, most likely water. This reaction gave a dark red solution, which was shown subjected to the work up as described above but no Ru cylinder related peaks were obvious within the $^1$H NMR spectrum, so this sample was discarded. These conditions were repeated with the same results achieved, and so the conditions were altered to increase the temperature to 200°C, and the maximum allowable pressure within the system was increased to 80 psi. Initially these conditions led to the same results as seen previously with the temperature achieved within the reaction vial again limited by the build up of pressure within the system, but when repeated, these conditions led to a dark brown solution which afforded a red/brown solid when worked up as described previously. $^1$H NMR and ESI-MS analysis showed that this crude mixture contained Ru cylinder and so this sample was purified using silica gel chromatography. $[Ru_2L_3]^{4+}$ was isolated in its pure form following three successive silica gel columns, eluted as the first orange band using a 3:1 mixture of acetonitrile and deionised water containing a final concentration of 10 mM $NH_4PF_6$. This gave a final yield of 1 mg, which represents a 0.25% yield with respect to starting materials. Although conditions had now been found that lead to the formation of Ru cylinder, the achieved yield was below that previously published and so the protocol was adapted to incorporate a stage where the glassware and ethylene glycol were purged with $N_2$ before beginning the reaction, as would be done if performing the reaction under reflux conditions.

The glassware used in the microwave is specially designed for the instrument and so does not connect to standard laboratory equipment such as a Schlenk line. This meant the only way to purge the glassware was to use an inverted funnel to create a curtain of $N_2$ under which the vial containing the solid reagents was kept. The ethylene glycol was purged in a Schlenk flask and then transferred to the vial underneath the curtain, before the lid was placed on the vial. The vial was then subjected to the same conditions as before, heated at 198°C for 4 hours, and this gave an orange/brown solution which was also precipitated using saturated aqueous $NH_4PF_6$, and then re-precipitated from acetonitrile using diethyl ether. The same purification routine as described above was followed and this gave a final yield of 3 mg (0.9%). Whilst this is still a small mass of final product, this protocol gives a higher yield to that of the published reflux protocol and it has been achieved with a vastly reduced reaction time, achieving the aim of creating a more efficient synthetic protocol. Attempts were made to scale up this protocol by doubling the amount of $[RuCl_3 \cdot xH_2O]$ and ligand used, but this lead only to crude material where only polymeric or double stranded cylinder were visible in $^1H$ NMR analysis.

It was consistently noted that the syntheses which led to the formation of Ru cylinder were those where the pressure within the microwave vial remained close to 0 psi. This suggests that it is contamination of the reaction mixture with another solvent with a higher vapour pressure at these temperatures that is preventing the reaction from going to completion. It cannot be said if this observation is purely an artefact of having set an arbitrary limit on the pressure within the system, or if this is an observation that can be applied to failed syntheses that have been observed whilst performing the reaction under reflux conditions. As the reflux conditions require that the reaction is performed in apparatus that has been purged with $N_2$, it too is performed in a closed system meaning that any water contamination of the solvent will remain in the system for the entirety of the reflux process. It is therefore proposed as future work that the use of a dry solvent be investigated to determine if the presence of water within the system has any effect on the yield of the reaction. One further aspect noted it that the starting material used for microwave synthesis of the Ru cylinder contains ruthenium in a 3+ oxidation state, as opposed to the 2+ oxidation state as found in $[Ru(DMSO)_4Cl_2]$. The use of a different Ru(II) starting material was considered for microwave synthesis, but as many of the simple Ru(II) compounds available are derivatives of $[Ru(bpy)_3]^{2+}$, it does not seem reasonable to assume that one $Ru{-}N_6$ chromophore would be broken to form another. The investigation of different ruthenium starting materials is therefore also proposed as future work but, as the aim of this work was not solely focused on improving synthetic protocols, these options were not pursued further here.

## 2.3 Improving purification protocols for Ru cylinder

As well as investigating methods to improve the synthesis of Ru cylinder, this work also presents attempts to improve the purification protocol. As discussed above, one consistent problem is the production of Ru(III) by-products, observed as paramagnetic material in NMR spectra which are not removed by chromatography. It was hypothesised that attempting to reduce any Ru(III) by-products to Ru(II) material may make separation more successful by changing the way that the species interact with the silica of the chromatography column. Therefore N-ethylmorpholine was used as a reducing agent, as previously seen in literature [68, 69, 70]. This procedure was introduced into the protocol after the first silica chromatography column, following the removal of the majority of the unwanted material. Following protocols as seen in literature cited above, the crude reaction material was dissolved in methanol and then heated before adding 2 ml of N-ethylmorpholine. Methanol was used as the solvent to allow for it to be oxidised to methanal as part of the redox reaction. This step led to the removal of much of the by-product, as shown by $^1$H NMR spectra in Figure 2.2.

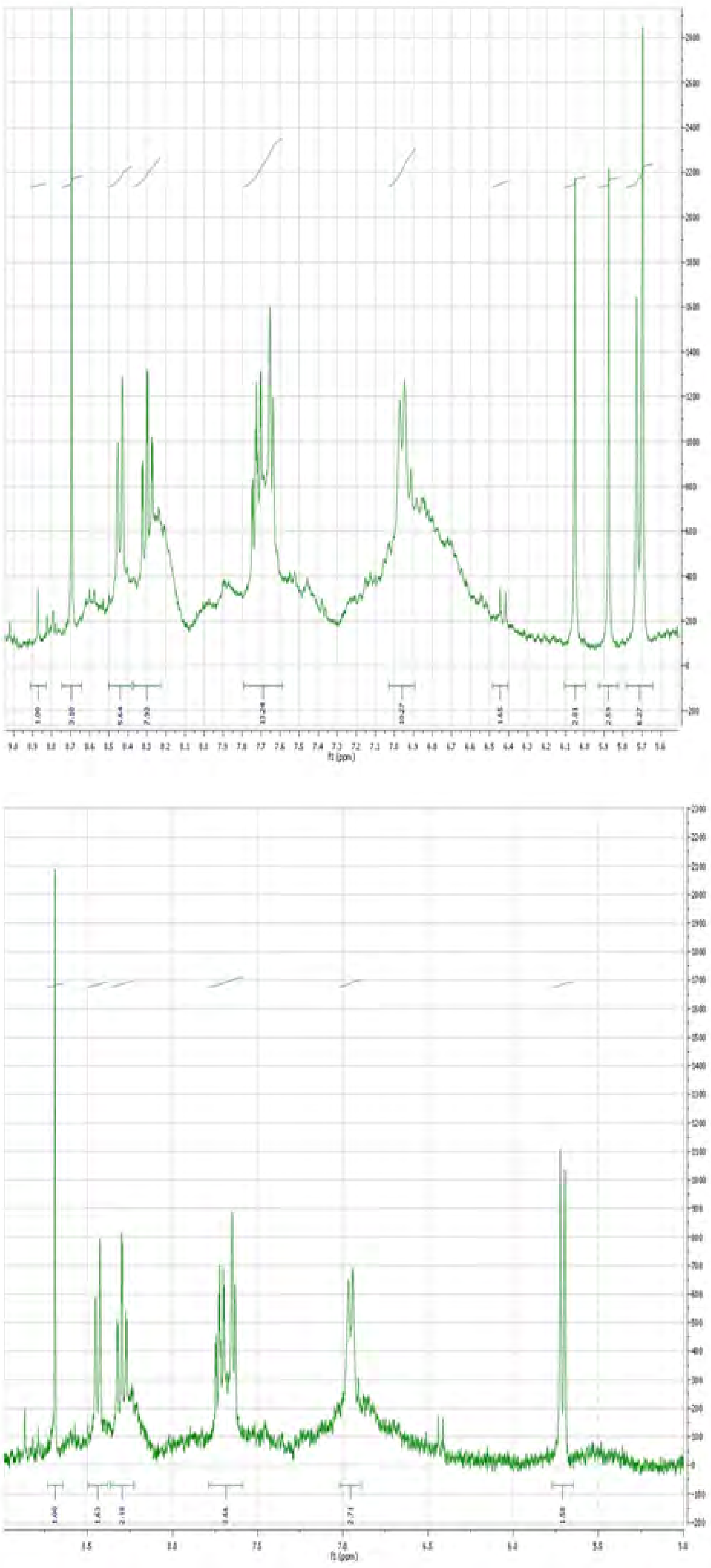

**Figure 2.2:** $^1$H NMR spectra of Ru cylinder before (top) and after (bottom) reduction with N-ethylmorpholine in methanol. The spectra show how this process led to the removal of much of the impurities initially seen within the $^1$H NMR spectrum.

Whilst the use of N-ethylmorpholine removed some of the impurities seen in $^1$H NMR spectra, it is clear that further column chromatography was still required to remove the remaining impurities. However, subsequent silica chromatography columns failed to remove any more impurities, showing that the use of this reducing agent did not further improve the purification protocol and so this was not investigated any further.

This work also presents investigations made to improve the column chromatography protocol for Ru cylinder, as the current protocol of silica chromatography is both time consuming and leads to large loss of product as it readily adheres to the silica. The use of Sephadex C-25 resin has been investigated and has been found to be more time-efficient. As the Sephadex resin must be prepared in aqueous solution, the crude $[Ru_2L_3]^4$ must also be soluble in water. When complexed with $(PF_6)$ counter-ions, the Ru cylinder is only soluble in acetonitrile or acetone, so it was necessary to complete an ion-exchange process. A protocol for this process had already been established as part of the published synthesis so this was used without alteration - the crude $[Ru_2L_3](PF_6)_4$ was dissolved in acetone and added to t-butylammonium chloride (also dissolved in acetone). This allows the chloride ion to replace the $(PF_6)$ counter-ion to give a final complex of $[Ru_2L_3]Cl_4$. This complex in insoluble in acetone, so precipitates from solution and can be collected by filtration. Using the Sephadex columns, pure product can be eluted using increasing concentrations of NaCl in water. Pure $[Ru_2L_3]Cl_4$ was eluted using 0.4 M NaCl. A second Sephadex column was usually required, again eluting with 0.4 M NaCl in water. This strategy proved to be more time efficient as it only required two chromatography columns to be used, but is does not lead to an increased yield of final product. Therefore either Sephadex C-25 or silica column chromatography were found to be suitable for purification of Ru cylinder.

## 2.4 Fluorescent properties of Ru cylinder

As discussed in Chapter 1, the attraction of using Ru cylinder to determine the cellular localisation of this class of compounds is the fluorescent properties of the Ru cylinder. The absorption and emission spectra of [$Ru_2L_3$]$Cl_4$ are shown in Figure 2.3. These show that the MLCT of the ruthenium cylinder has a maximum at 484nm and, when excited at this wavelength, gives an emission spectrum with a maximum at 690nm.

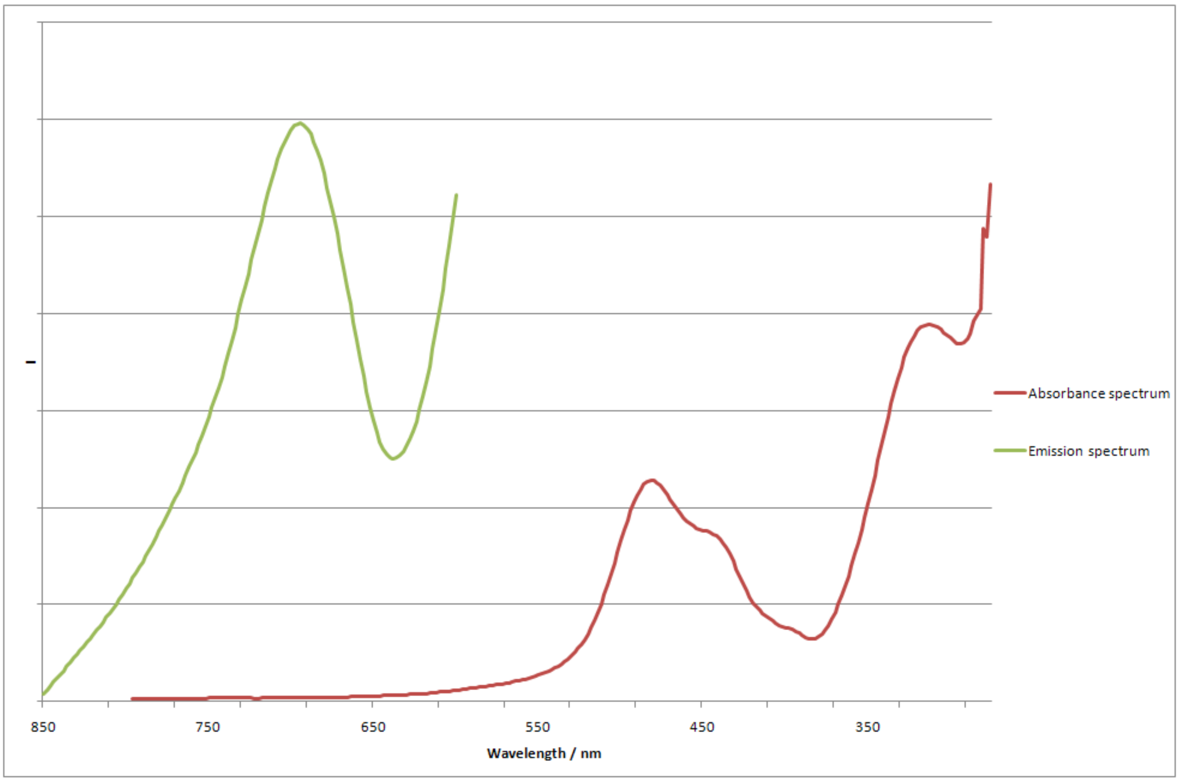

**Figure 2.3:** Absorption and emission spectra of Ru cylinder recorded in DMEM media normalised to one at the point of maximum absorption or emission. The absorption spectrum shows MLCT centred at 484nm, with maximum emission at 690nm

The emission recorded from [$Ru_2L_3$]$Cl_4$ is found in the far-red portion of the electromagnetic spectrum. This is in line with other Ru−$N_6$ chromophores, the most notable of these compounds is [$Ru(bpy)_3$]$^{2+}$ - tris(bipyridine) ruthenium(II). [$Ru(bpy)_3$]$^{2+}$'s emission is however centred at 630nm, so there is a notable red-shift in light emitted by [$Ru_2L_3$]$^{4+}$. This change has previously been attributed to the pyridylimine ligand having a $\pi^*$ orbital at a lower energy than that observed in the pyridine ligand [71]. Combined with the recorded absorption profile, it is expected that [$Ru_2L_3$]$^{4+}$ will be suitable for both fixed and live cell imaging. The MLCT occurs at 484nm - a wavelength which is outside the UV range and so exciting here will not the cause severe damage to cells during live cell imaging that is associated with UV light. It also means the MLCT can be efficiently excited using a commonly available 488nm argon laser. The emission profile is also favourable as any emission seen at 690nm during cell imaging should be directly attributable to $[Ru_2L_3]Cl_4$ as cellular autofluorescence is not known to be observed in this region. With a suitable synthetic protocol established, imaging experiments began.

# Chapter 3

# Investigating the cellular localisation of cylinders

## 3.1 Developing a suitable imaging protocol

As no cytotoxicity data for MDA-MB-231 cells treated with $[Ru_2L_3]^{4+}$ had been collected, developing a suitable imaging protocol was the first aim of this work. Previous work in the group suggested that treatment of the same cell line with $[Fe_2L_3]^{4+}$ led to a disruption in cell motility, and caused cells to 'ball up'. However, when MDA-MB-231 cells are treated at the same concentration for the same amount of time, results of an MTT assay show that the cells are still viable [14], so imaging alone of $[Ru_2L_3]^{4+}$ treated cells cannot determine which cells are simply changing morphology due to the effects of cylinder and those which have entered apoptosis. It was therefore decided to perform an assay to determine how viable MDA-MB-231 cells are after treatment with increasing concentration of ruthenium cylinder. The ToxiLight BioAssay was selected as it is a straightforward and highly sensitive assay. It works by detecting the presence of adenylate kinase (AK) in cell media. AK is a phosphotransferase enzyme found in all mammalian cells, and will only be found in cell media when the membrane of cells has been compromised and so has leaked into the surrounding media. AK catalyses the interconversion of two molecules of adenosine diphosphate (ADP) to one molecule each of adenosine triphosphate (ATP) and adenosine monophosphate (AMP);

$$\text{Mg}^{2+}\text{-ADP} + \text{ADP} \xrightarrow{AdenlyateKinase} \text{Mg}^{2+}\text{-ATP} + \text{AMP}$$

This assay utilizes a second enzyme, luciferase, which catalyses the formation of light from ATP according to the following reaction;

$$\text{ATP} + \text{Luciferin} + \text{O}_2 \xrightarrow[Mg^{2+}]{Luciferase} \text{Oxyluciferin} + \text{AMP} + \text{PP}_\text{i} + \text{CO}_2 + \text{light}$$

The intensity of light emitted is therefore linearly related to the levels of AK in the cell media, which can then be taken as a measure of the level of cell viability.

Cells were treated with 12.5, 25, 50 or 100 μM $[Ru_2L_3]^{4+}$ and positive or negative control samples were also prepared. A 100% Lysis Reagent was used as the positive control and a tris-acetate buffer was used for the negative control  both of these reagents were supplied with the assay kit. Three 30 μL aliquots of cell media were taken at zero, two, four and six hours. This was then added to AK detection reagent in a 96-well plate, and luminescence was recorded on a TECAN GENios Multifunction Microplate reader. The average of the three readings taken at each time point was then calculated and corrected for background luminescence from the AK detection reagent alone. The percentage viability was then defined as;

$$[(\text{Positive control} - \text{averaged reading})/\text{Positive control}] \times 100$$

The averaged luminescence value of the positive control sample after 6 hours was taken as the positive control value, as all cells would be completely lysed by this time point. Data is presented in Figure 3.1 on page 55.

These results show that there appears to be little or no cytoplasmic membrane damage induced by these concentrations of cylinder over this time-scale. this suggests that the change in morphology observed during imaging using these time-scales and concentrations is not due to apoptosis and therefore appears to reinforce the findings of the previous work with $[Fe_2L_3]^{4+}$. Control experiments performed with $[Ru_2L_3]^{4+}$ added to cell lysates produced surprising results. Increasing concentrations of $[Ru_2L_3]^{4+}$ lead to decreasing luminescence, suggesting that

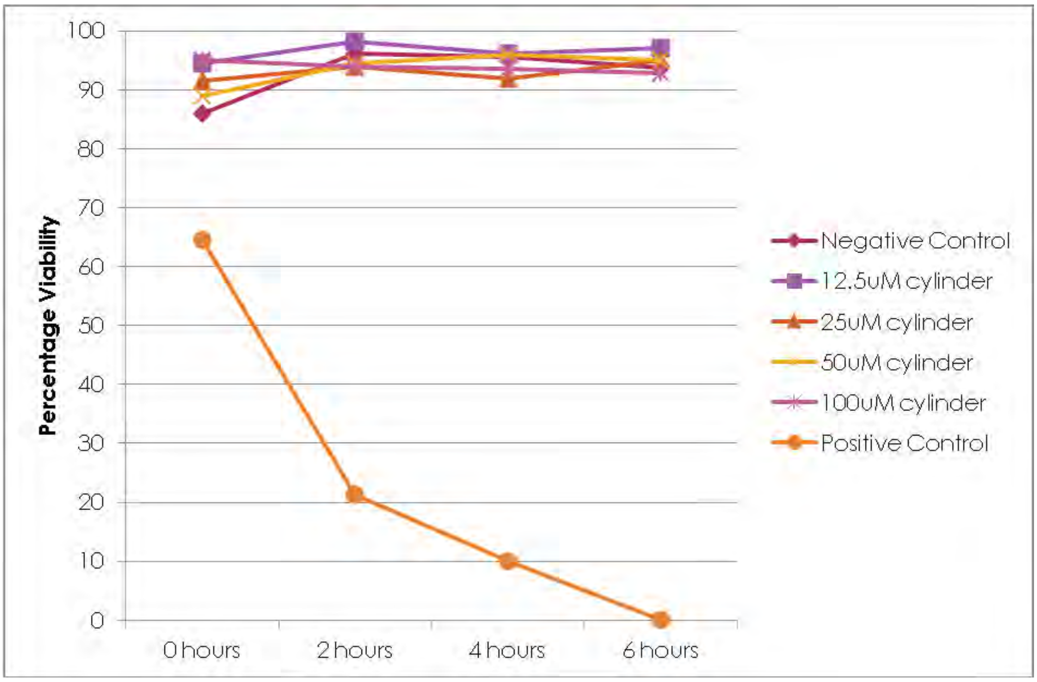

**Figure 3.1:** The cytotoxic affect of $[Ru_2L_3]^{4+}$ on MDA-MB-231 cells as determined by Toxilight assay. The data points are the mean and standard deviation of three experiments (n=3) carried out in quadruplicate.

$[Ru_2L_3]^{4+}$ inhibits the production of light during the assay. Further control experiments with cell lysates showed that the inhibition is a function of a complete cylinder and not free ligand L or metal, as shown in Figure 3.2 and Figure 3.3 on page 56.

It was therefore decided that the Toxilight assay was not suitable for developing an imaging protocol. Based on previous work using MTT assay to determine the toxicity of $[Ru_2L_3]^{4+}$ [14] [42], it was decided to use 100 µM treatments for imaging studies as this had been shown to not be toxic over the short time frame used for imaging experiments.

## 3.2 Fluorescence microscopy of cylinders within cells

### 3.2.1 Imaging Ru cylinder using confocal fluorescence microscopy

Confocal microscopy has been utilized in order to image $[Ru_2L_3]^{4+}$ within MDA-MB-231 cells. As the cylinder is known to have its maximum emission at 705nm, emission was col-

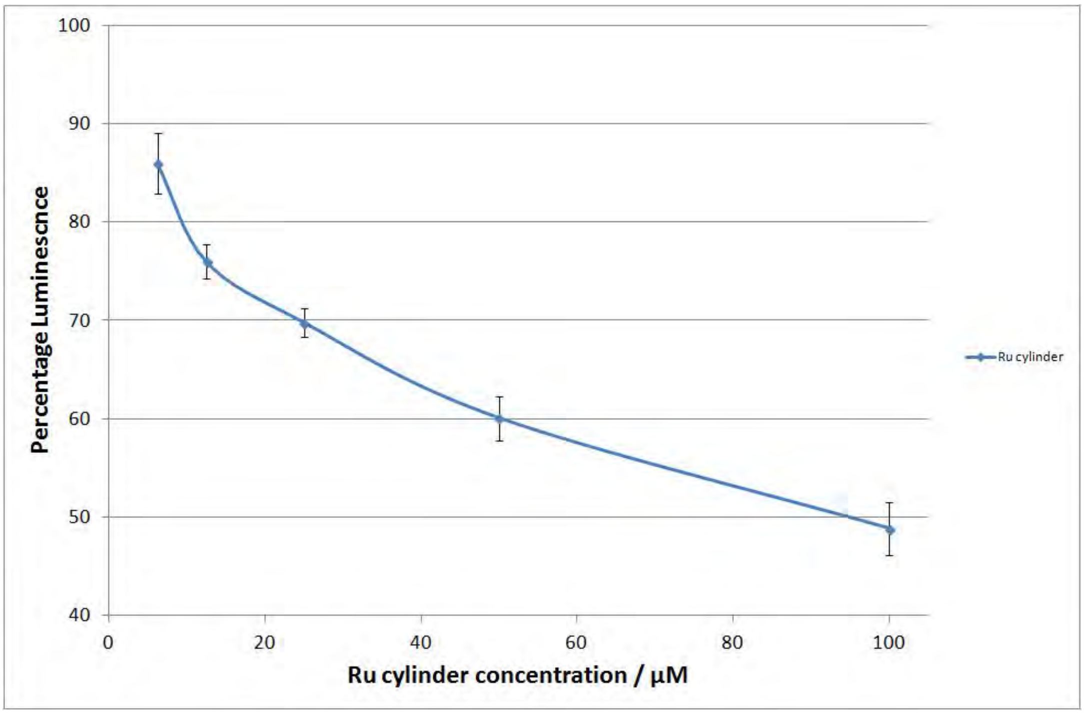

**Figure 3.2:** The inhibition of light produced during Toxilight assay using cell lysates treated with increasing concentrations of $[Ru_2L_3]^{4+}$. The data points are the mean and standard deviation of triplicate experiments.

lected between 680-720nm, following excitation at 484nm. Control samples of untreated cells were imaged, as were cells treated for both 1.5 and 4 hours respectively. Cells treated for 1.5 hours clearly show cellular uptake of the compound, but no clear evidence of nuclear localisation, shown in Figure 13. Areas of fluorescence corresponding to the appearance of vesicles surrounding the nuclear membrane suggest either an endocytosis uptake mechanism, or the ‘packaging’ of the compound once within the cell. The images taken of samples treated for 4 hours show similar results, with no clear nuclear localisation observed, but again distinct areas of fluorescence corresponding to vesicles could be seen, shown in Figure 3.4.

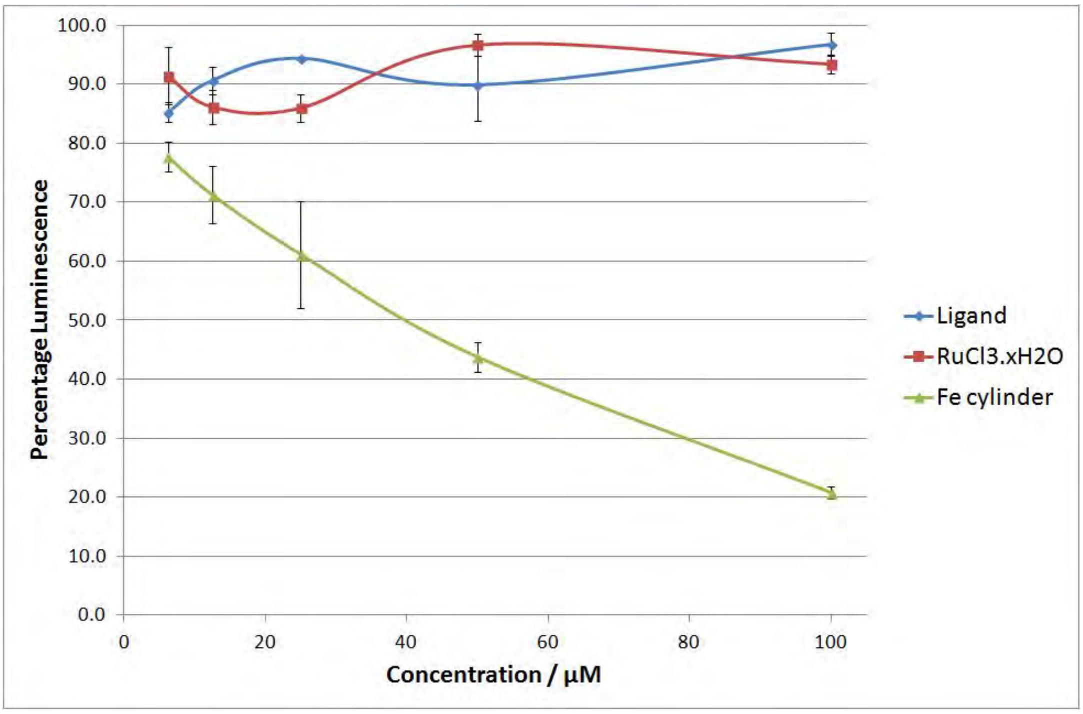

**Figure 3.3:** Control experiment for Toxilight assay with cell lysates treated with ligand L, $RuCl_3 \cdot xH_2O$ and $[Fe_2L_3]^{4+}$ showing that light production is only inhibited by the cylinder structure, not its components. The data points are the mean and standard deviation of triplicate experiments.

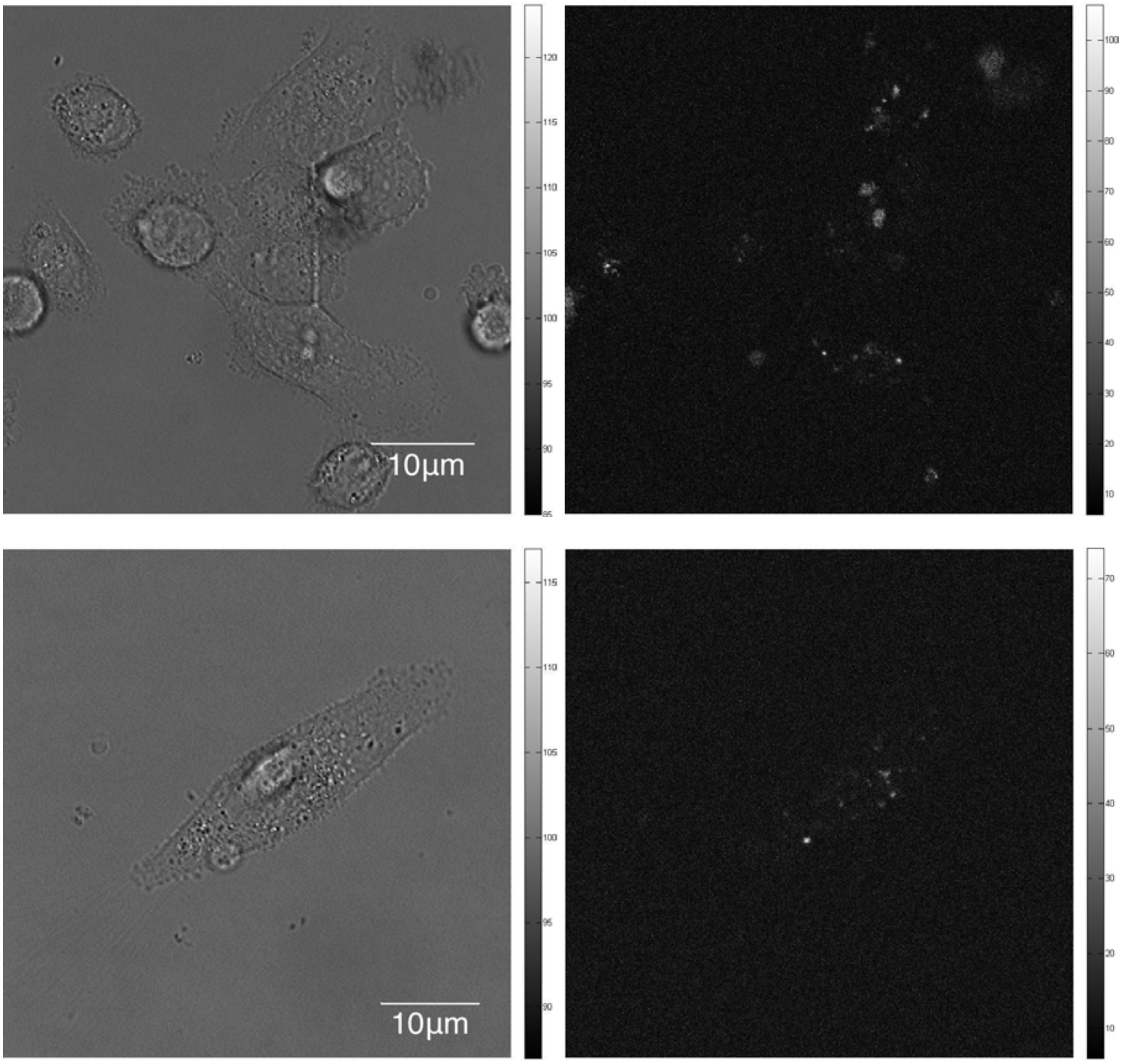

**Figure 3.4:** Images of $[Ru_2L_3]^{4+}$ in MDA-MB-231 cells, at time points 1.5 hours (top row) and 4 hours (bottom row). Scale bar indicates 10 μm, and intensity bars correlate to detected fluorescent counts.

The images shown in the bottom row of Figure 3.4 was recorded as part of a Z-stack experiment where confocal images are recorded at intervals throughout the volume of the cell. It was then possible to use these images to produce an image to show the average fluorescence signal in the cell. An image showing the average fluorescence detected is shown in Figure 3.5.

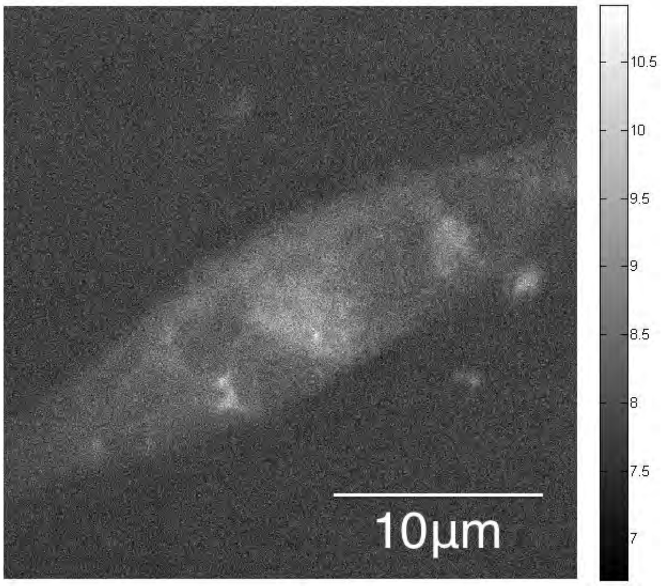

**Figure 3.5:** Image showing the average fluorescence of $[Ru_2L_3]^{4+}$ in MDA-MB-231 cells. Scale bar indicates 10 µm, and intensity bars correlate to detected fluorescence counts.

The fluorescence signal across the cell is very weak, and there is a comparable level of noise within the image. However the strongest signal seen is that from within the cell, and it does strongly suggest that $[Ru_2L_3]^{4+}$ is taken into MDA-MB-231 cells and leads to a fluorescent signal. The fluorescence signal is not evenly distributed across the cell suggesting some degree of localisation within the cell.

After observing Ru cylinder within MDA-MB-231 cells, attempts were also made to image the cylinder within SKOV-3 ovarian cancer cells. Previous toxicology work within the group has shown that the Ru cylinder is inactive against SKOV-3 cells whilst the Fe cylinder has toxicity within one order of magnitude of cisplatin [14]. Imaging of cells treated with Ru cylinder for 4 hours revealed that no fluorescence was observable from within the SKOV-3 cells (as shown in Figure 3.6) suggesting that the Ru cylinder is inactive as it does not enter the cells or because it is immediately broken down once inside the cell.

Therefore MTT data was acquired to determine if free ruthenium metal is toxic to MDA-MB-231 or SKOV-3 cells - if it is proved to be toxic then it can be said that the viability of the cells following cylinder treatment indicates that the cylinder is not broken down within the cell.

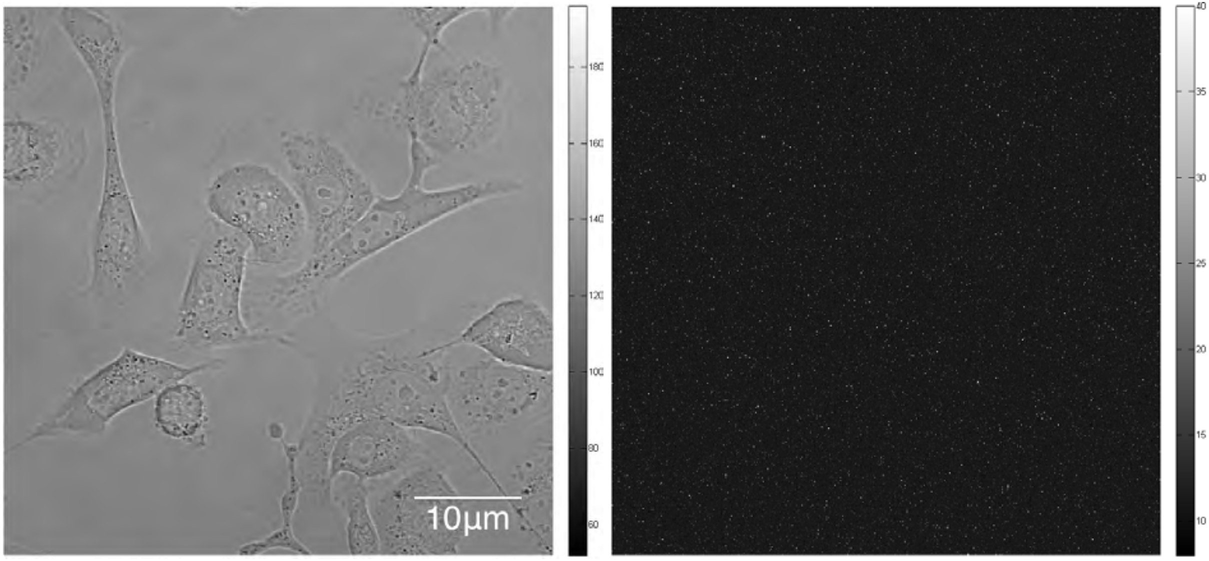

**Figure 3.6:** Image of SKOV-3 cells treated with $[Ru_2L_3]^{4+}$ for four hours, showing brightfield image (left) and fluorescence image (right), however no discernible fluorescence signal was observed. Intensity correlate to detected fluorescence count.

MTT assay work has already shown that free ligand is not toxic to cells [42]. Data collected here now shows that free ruthenium is also non-toxic to SKOV-3 and MDA-MB-231 cells, as determined using Student's t-test, at a confidence of $P < 0.05$. This means it cannot be said for certain whether the cylinder enters SKOV-3 cells and is then broken down, or does not enter the cell at all. It also raises the possibility that the low levels of fluorescence seen in MDA-MB-231 cells may be caused by $[Ru_2L_3]^{4+}$ being taken into cells and then being metabolised, losing the Ru-$N_6$ chromophore. The results of the MTT assays are presented in Figure 3.7.

### 3.2.2 Imaging fluorophore-tagged cylinders using an integrated UV-Vis spectrometer/brightfield microscopy system

As observing the cylinder within cells proved difficult due to the low quantum yield of the cylinder, work began on attaching a fluorophore to the parent ligand, L. The aim of this was to improve visualisation of the cylinder within cells, whilst remaining aware that the addition of

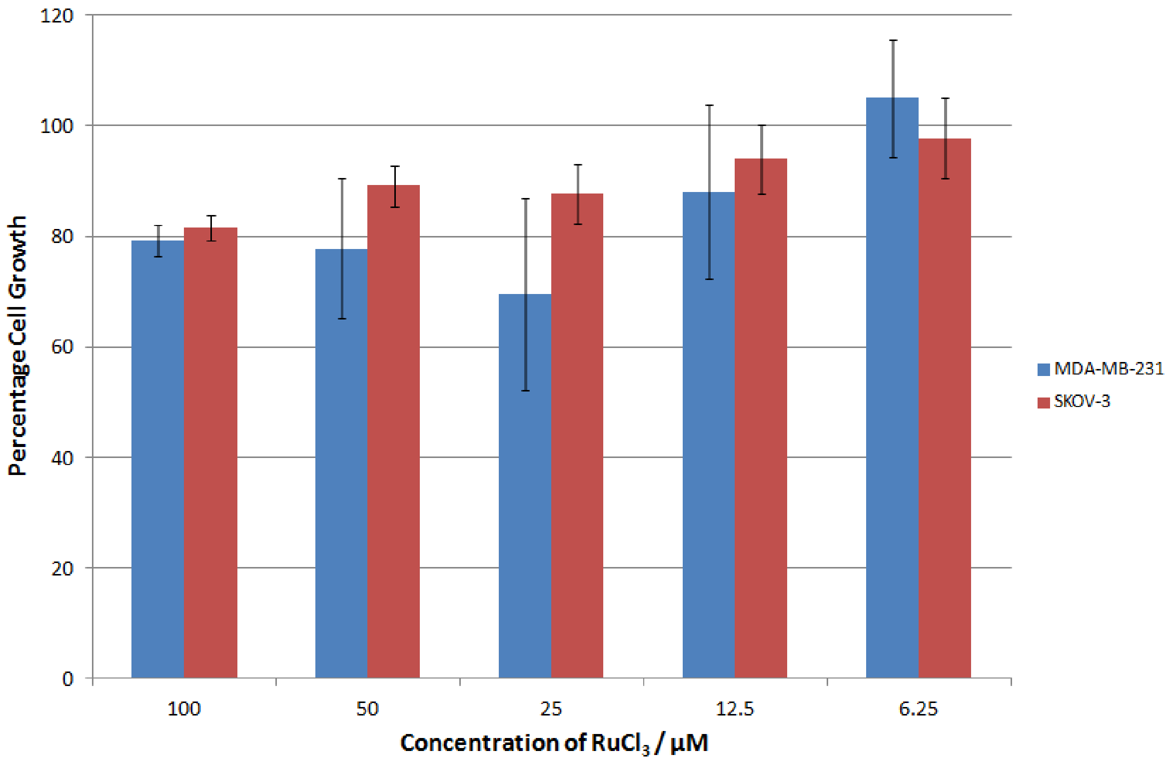

**Figure 3.7:** MTT data of $RuCl_3 \cdot xH_2O$ showing that it is not toxic for MDA-MB-231 or SKOV-3 cancer cells. Data shows mean and standard deviation (n=3) or triplicate experiments, each experiment was performed in quadruplicate. Student's t-test analysis using P=0.05 showed that there was no statistically significant difference between the population treated with $RuCl_3 \cdot xH_2O$ and those left untreated.

any fluorophore to the cylinder would clearly alter the cylinder's size, shape and could also impact on the cylinder's DNA binding properties. The ideal fluorophore would therefore be small enough to not interfere with the cylinder's DNA binding properties and have fluorescent properties suitable for cellular imaging. Anthracene was chosen as it is small, has a high quantum yield, absorption and emission removed from cellular autofluorescence and an usual emission spectrum which would be easily identified within a sample. Using synthetic routes previously developed within the group [72], a synthetic route for attaching commercially available 2-amino anthracene to the C5 position of ligand L's terminal pyridine group was devised, and ultimately $[Cu_2L^{Ant}2]^{2+}]$ cylinder was synthesised within the group [73]. Due to the large size of this compound it was only soluble in DMSO, limiting its usefulness as an imaging probe as the presence of DMSO is toxic to cells on its own. The low yielding reaction also meant that there was not enough compound to perform toxicology and imaging studies, so as a first attempt at imaging, MDA-MB-231 cells were treated with 100μM anthracene-tagged cylinder for 4 hours, fixed using paraformaldehyde and mounted onto microscope slides before being imaged using a novel integrated UV-Vis spectrometer and brightfield microscope system. Recorded images are shown in the top and middle rows of Figure 3.8.

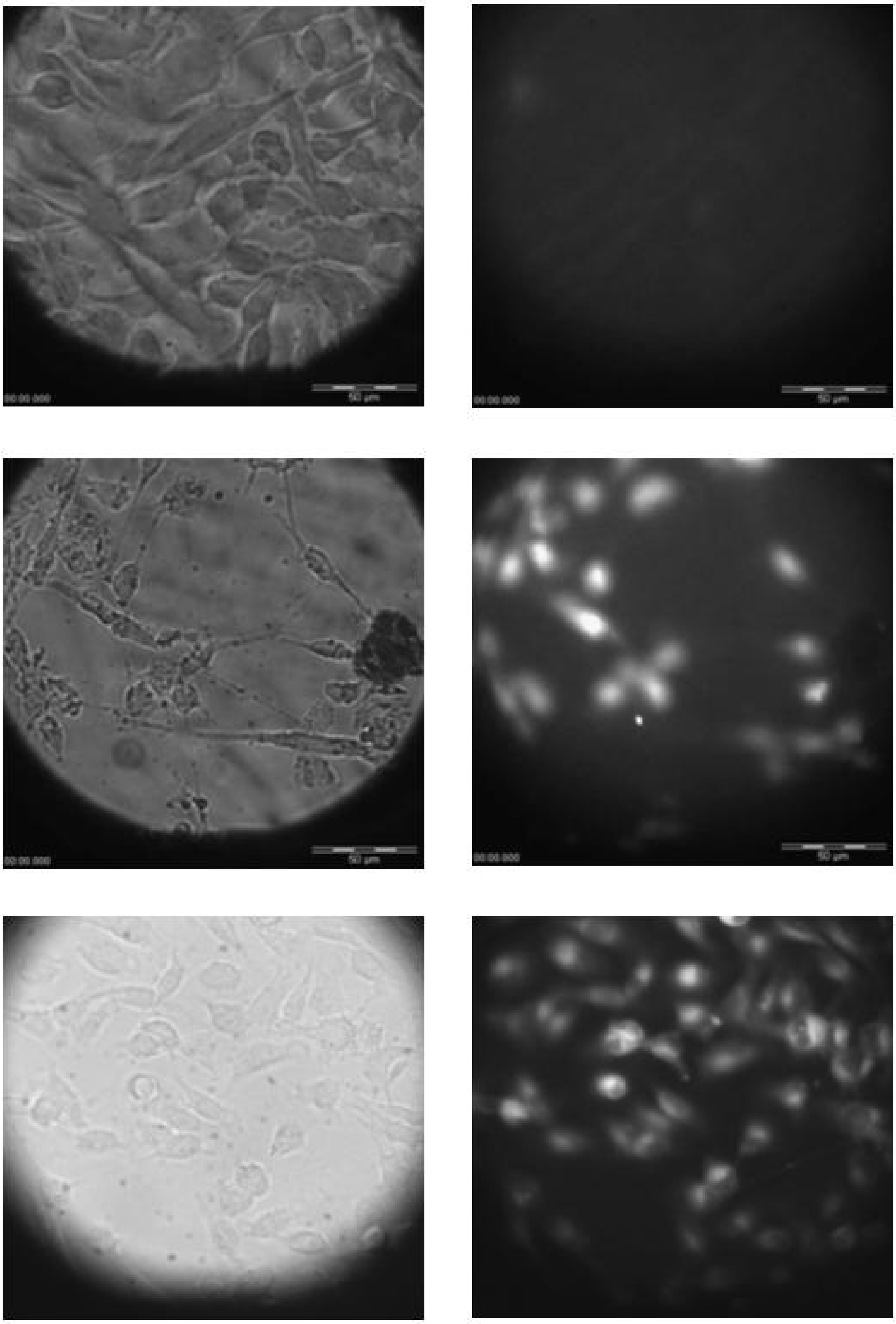

**Figure 3.8:** MDA-MB-231 cells imaged using an integrated UV-Vis spectrometer and brightfield microscope system. Top row shows control brightfield and corresponding fluorescence images, middle row shows cells treated with 100μM anthracene-tagged cylinder and bottom row shows cells treated with 100 μM amino-anthracene. Both treated samples show observable fluorescence following excitation at 342nm however those treated with anthracene-tagged cylinder show a clear change in morphology. Scale bar indicates 50 μm.

The control samples show the expected cell morphology of MDA-MB-231 cells, with the known 'spindle-like' morphology clearly observable in the brightfield image. The corresponding fluorescence image shows no cellular autofluorescence following excitation at 342nm. Treatment with the copper cylinder shows a clear induced change in morphology and also a decrease in cell density on the surface. The corresponding fluorescence image shows bright fluorescence within cells, although not localised to any definable region. Exciting at the MLCT from copper to ligand ($\lambda_{\mathrm{ex}}$ = 540nm) led to no observable fluorescence.

As this is a new cylinder, it was not known how stable this compound would be. As such, imaging studies continued using amino-anthracene instead of cylinder. It was believed that the spectra of bound and free anthracene within cells would differ due to the extended conjugation system of the cylinder. Therefore images and emission spectra were recorded of MDA-MB-231 cells treated with amino anthracene and are presented in the bottom row of Figure 3.8. Comparing spectra for control, cylinder-treated and anthracene-treated samples with the spectra of anthracene cylinder in DMSO solution (as shown in Figure 3.9), it is clear the cylinder treated samples retain the characteristic finger-print spectra of the anthracene cylinder, whereas the samples treated with amino-anthracene show an broad extra peak centred around 500nm.

From the recorded images and emission spectra, it is believed that the anthracene remains bound to the ligand within cells. However it was not known how stable a double-stranded copper cylinder would be, and if the cylinder was remaining as one structure within cells. So the stability of copper cylinders was investigated using UV/Vis absorption spectrometry. Due to the difficulty and low yielding synthesis of the anthracene cylinder, the studies were performed using the a copper cylinder synthesised using the parent ligand - $[Cu_2L_2]^{2+}$, which has previously been synthesised within the group [74]. The absorption spectrum of $[Cu_2L_2]^{2+}$ shows absorbance at 240nm, 330nm and 505nm, with the absorbance at 505nm due to the MLCT. The absorption spectra of $[Cu_2L_2]^{2+}$ is shown in Figure 3.10.

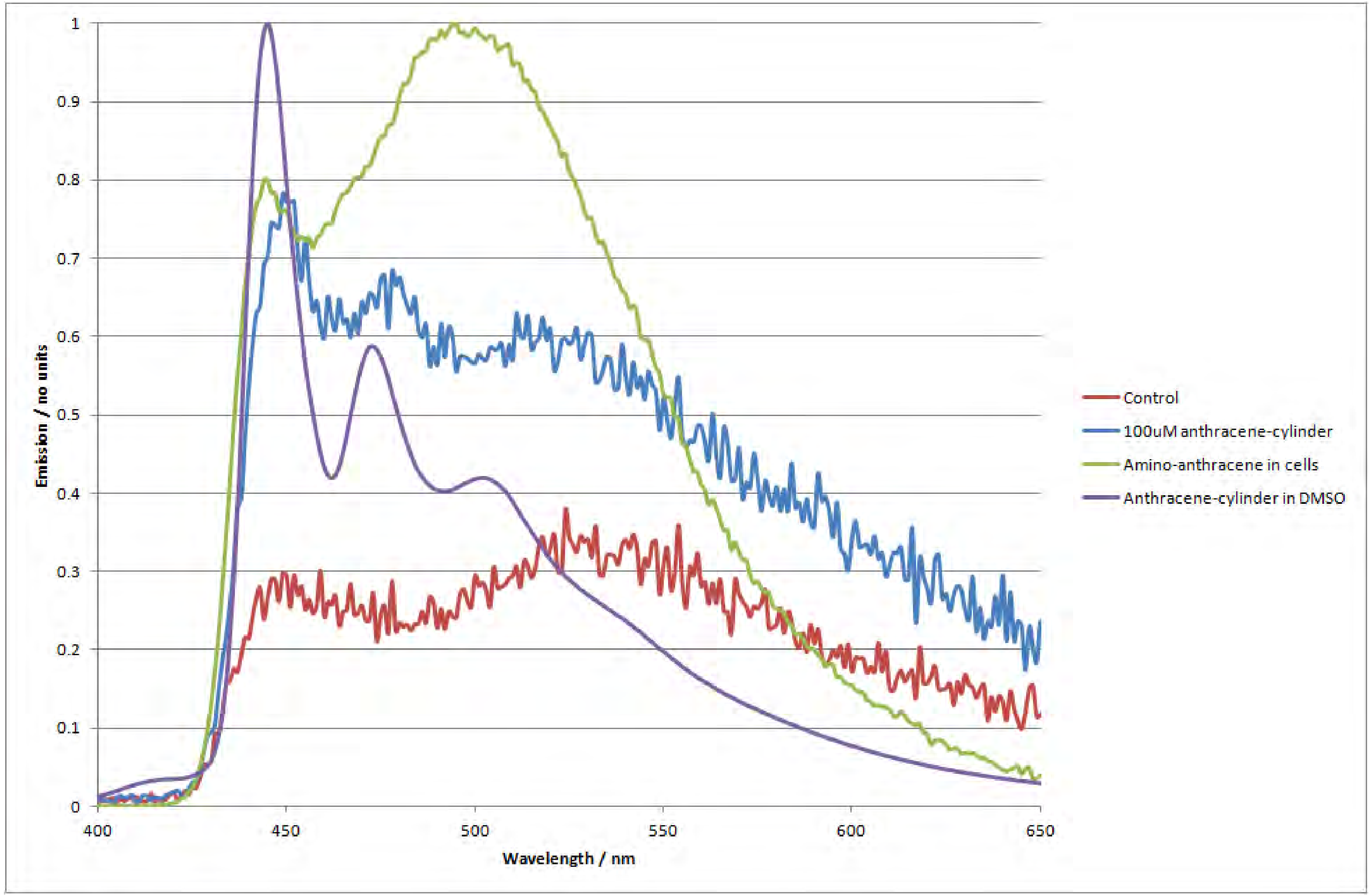

**Figure 3.9:** Emission spectra of MDA-MB-231 cells treated with anthracene cylinder, amino-anthracene and DMSO solution of anthracene cylinder

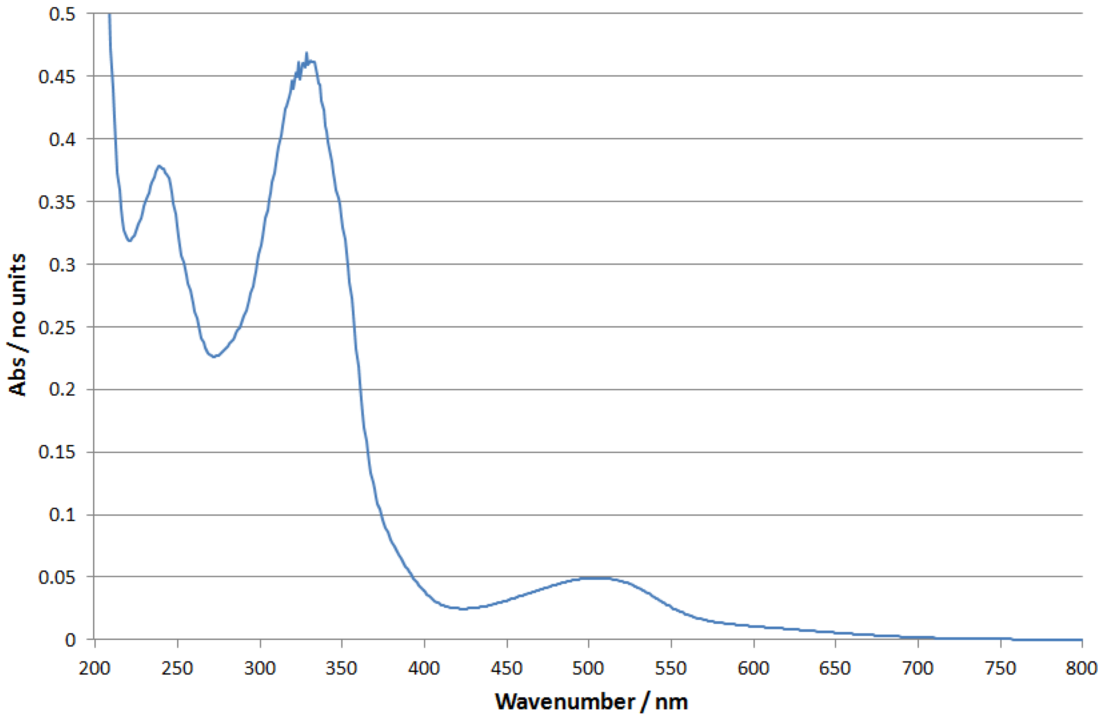

**Figure 3.10:** Absorption spectrum of $[Cu_2L_2]^{2+}$.

Stability studies (performed by recording UV-Vis spectra of a compound over 12 hours in solution and observing any change in absorption bands) show that $[Cu_2L_2]^{2+}$ does not fall apart in solution during the time scale measured, the resulting spectra are shown in Figure 3.11 - only the spectra recorded at 0 and 12 hours are shown for clarity.

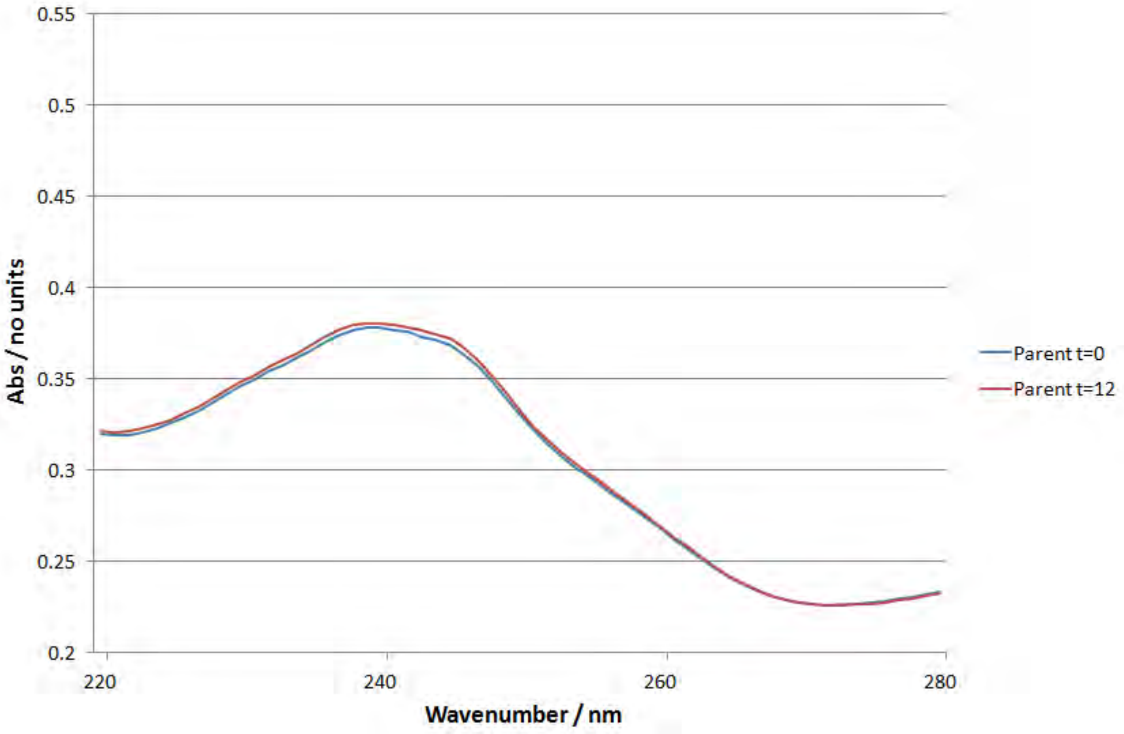

(a) Spectra of region 220-280nm

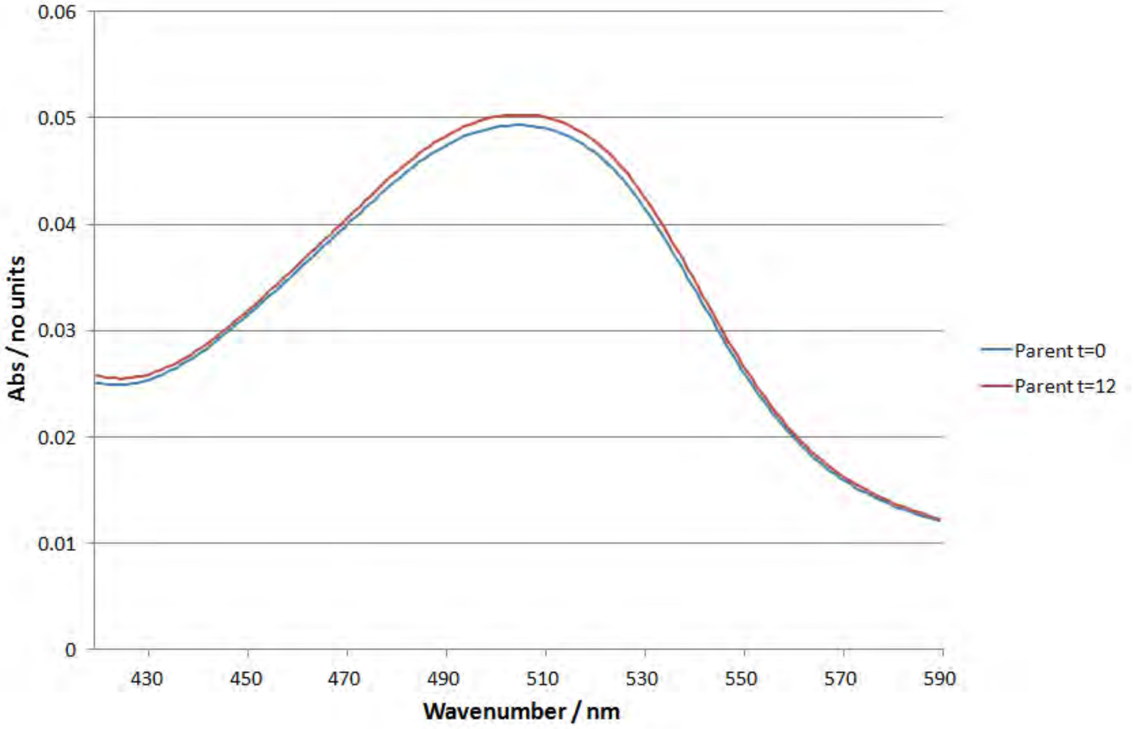

(b) Spectra of region 420-590nm

**Figure 3.11:** Stability studies of $[Cu_2L_2]^{2+}$ (Parent cylinder). Spectrum at 0 hours shown in blue and spectrum at 12 hours in red. Spectra for the region 220-280nm (top image) and 420-590nm (bottom image) show that $[Cu_2L_2]^{2+}$ does not fall apart in solution.

The anthracene modified ligand has been been shown to remain intact within MDA-MB-231 cells, but as no fluorescence resulting from a metal-ligand transition has been observed, it cannot be said that the cylinder structure as a whole is intact within the cells. However stability studies with other double helicate copper cylinders show that this general structure is stable.

Previous work within the group to attach peptides to the triple stranded iron cylinder [72] showed that the modified cylinder had increased toxicity and actually stabilised the DNA three-way junction compared to the parent cylinder. Work of this type must be performed to determine if the addition of the anthracene has altered the DNA binding that was previously observed for double stranded copper cylinders [75].

## 3.3 Co-localisation of cylinders with cellular dyes

Another strategy investigated for determining the cellular localisation of cylinders was to look for co-localisation of cylinder fluorescence with organelle specific dyes. Using this strategy gave two possible ways of looking for cylinder localisation;

- Co-localisation of dye and cylinder fluorescence
- Decreasing dye emission with increasing cylinder concentration – suggesting the cylinder is either quenching or displacing the dye.

### 3.3.1 Studies with Hoechst nuclear dyes

The nuclear dye investigated was Hoechst 34580. This was chosen as it is an easy to use dye with attractive fluorescence properties. Although its maximum absorption is at 375nm, it can be efficiently excited using a readily available 405nm laser, and has emission centred around 450nm when bound to DNA. This gives Hoechst 34580 another attractive property – the possibility of engineering a Forster Resonant Energy Transfer (FRET) experiment. The long tail observed on Hoechst 34580 means that the ruthenium cylinder should absorb in the region Hoechst emits. It was hoped that by exciting at 405nm, fluorescence could be observed in the 680-720nm region and therefore be attributed to the cylinder. This offered a third way of showing any nuclear localisation of cylinder, in addition to those described above. MDA-MB-231 cells were treated with 0.4 µg/mL Hoechst 34580 for 25 minutes followed by 4 hours treatment with 15 µM $[\mathrm{Ru_2L_3}]^{+}_{4}$ and imaged live using confocal microscopy. Figure 3.12 shows a control experiment of cells treated solely with Hoechst 34580, and it is clear that the tail of the Hoechst emission spectrum is still detectable between 680-720nm - the area where it was hoped FRET fluorescence from the ruthenium cylinder would be detected.

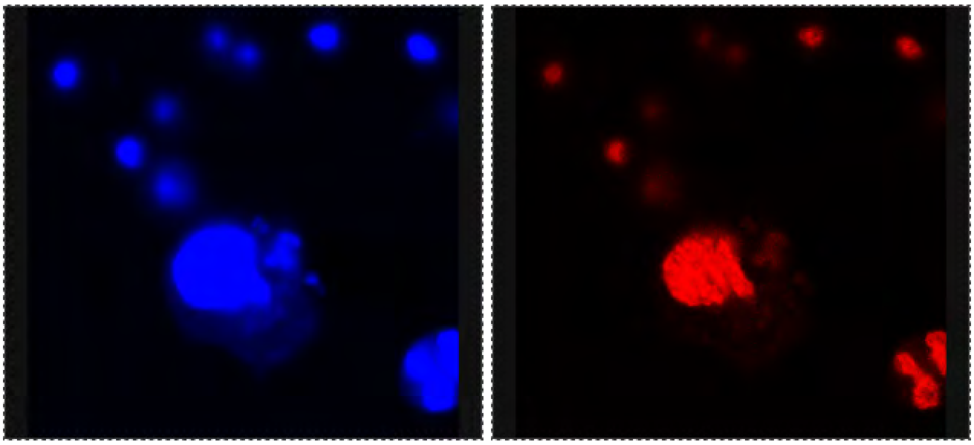

(a) Emission recorded between 440-460nm (b) Emission recorded between 680-720nm

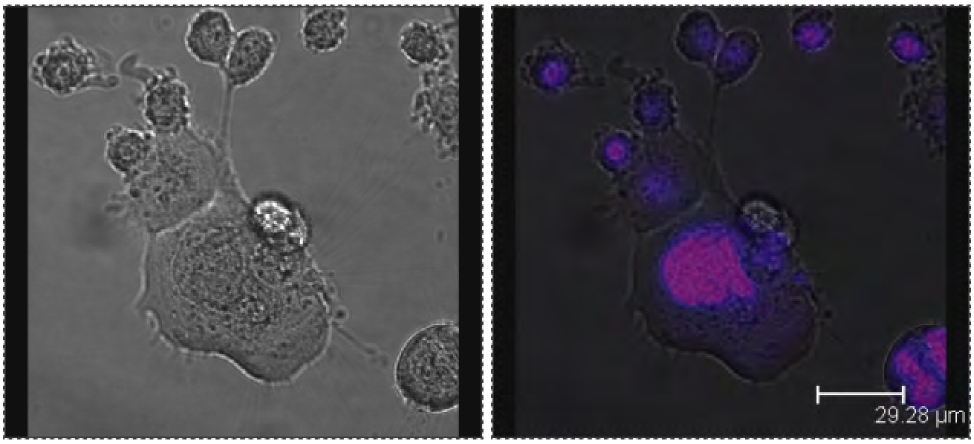

(c) Corresponding brightfield image (d) Overlay of images (a-c)

**Figure 3.12:** Images of MDA-MB-231 cells stained with Hoechst 34580 nuclear dye.

Figure 3.13 shows the images collected of cells following treatment with ruthenium cylinder, which were recorded under the same conditions as those shown in Figure 3.12.

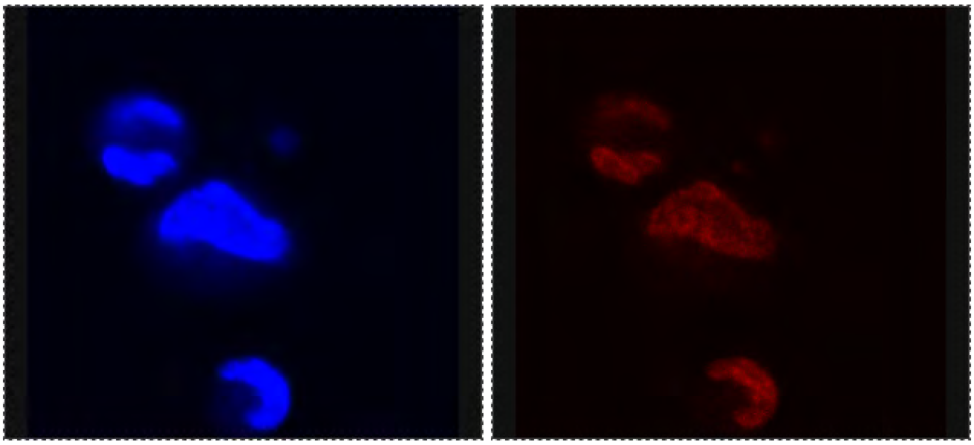

(a) Emission recorded between 440-460nm (b) Emission recorded between 680-720nm

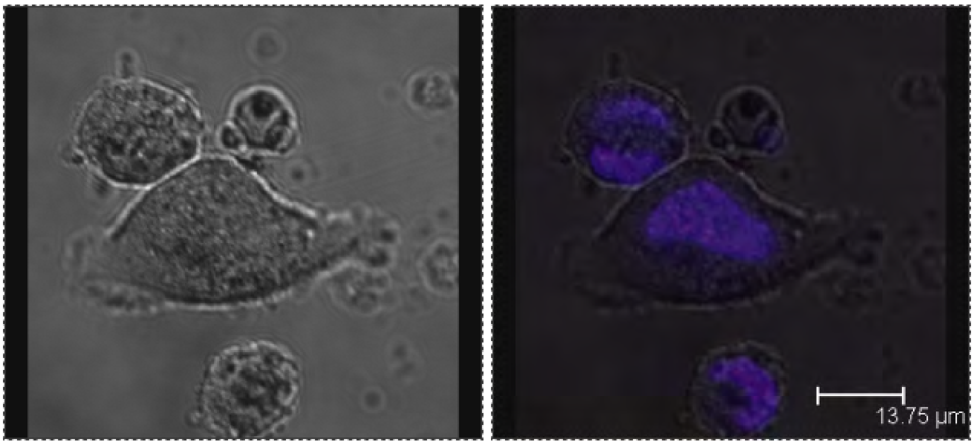

(c) Corresponding brightfield image (d) Overlay of images (a-c)

**Figure 3.13:** Images of MDA-MB-231 cells stained with Hoechst 34580 nuclear dye and then treated with $[Ru_2L_3]^{4+}$.

It was however noted that the fluorescence appeared to decrease following treatment with the cylinder, so analysis of both sets of images was undertaken to see if an decrease in fluorescence could be observed following cylinder treatment. Taking a simple average mean pixel intensity across the whole image is not a reliable approach as this does not take into account the number of cells in each image – images containing large areas of background could artificially decrease the mean pixel intensity. To combat this a simple algorithm was constructed to threshold the fluorescence images into binary images where pixels of an intensity above that found in the control images were given a value of 1, and all other pixels took a value of 0. Determining the mean pixel intensity of the thresholded pixels in the original image gives a much fairer reflection of the average fluorescence intensity for each sample. The calculated average intensities are presented in Figure 3.14.

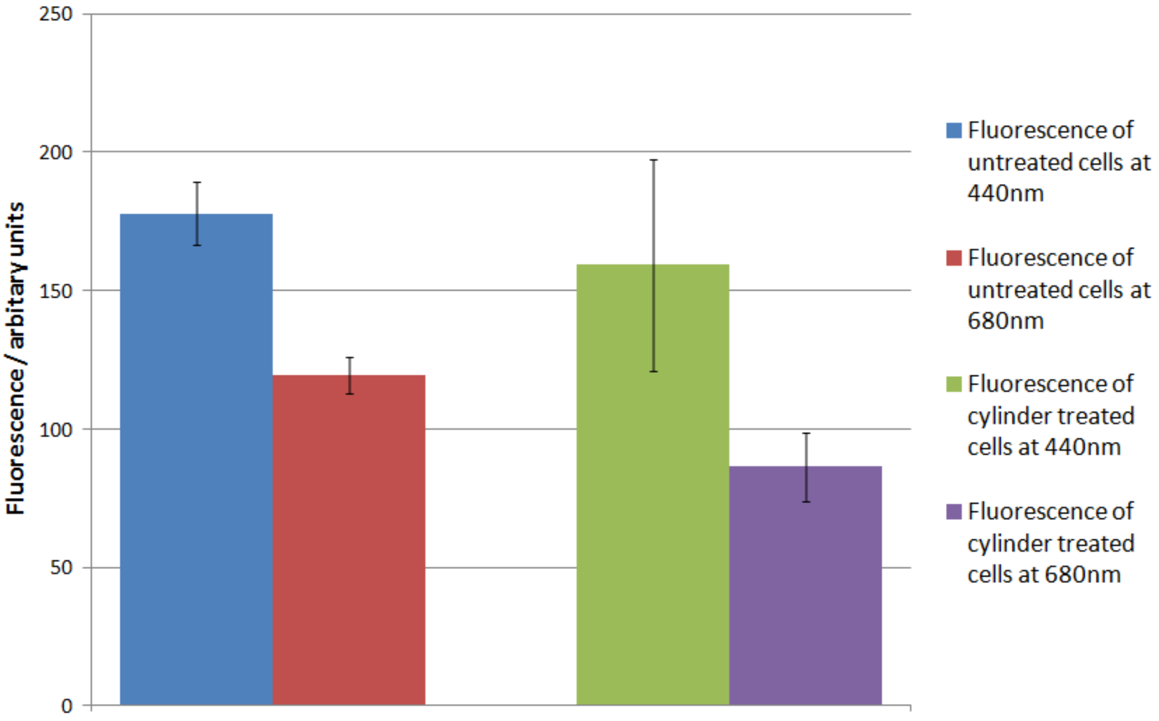

**Figure 3.14:** Average pixel intensity of fluorescence images of MDA-MB-231 cells treated with Hoechst 34580, with $\lambda_{ex}$ = 405nm. The red and blue bars are controls, showing average intensity between 440-460nm and 680-720nm respectively. The green and purple bars show average pixel intensity between the same ranges following treatment with $[Ru_2L_3]^{4+}$. Error bars indicate one standard deviation (n=3) from the mean pixel intensity. A Student t-test at p=0.05 showed that the difference between recorded fluorescence at each wavelength is statistically significant.

The average pixel fluorescence intensity is shown to decrease following treatment with cylinder, but emission recorded between 440-460nm in control and treated samples lie within a standard deviation of each other, so it cannot be said that the decrease is statistically significant, and so no further analysis of this data is presented here. It is also noted that, the images analysed here were acquired by confocal microscopy as a proof of principle, and so there is the possibility that the change in fluorescence seen is due to the location of the plane in focus within the cell. As such, Z-stack experiments over a series of cells would give the total level of fluorescence within them, and lead to a fairer comparison. This line of investigation was not pursued further in this work, but was instead taken forward within the group - Z-stack images of cells treated with Hoechst dye and then treated with the Fe cylinder showed a significant decrease in Hoechst emission, showing that the Fe cylinder was able to displace Hoechst dye [76].

## 3.4 Using synchrotron radiation to detect cylinders within cells

### 3.4.1 Principles of XANES and XRF spectroscopy

X-Ray Absorption Near-Edge Spectroscopy (XANES) is a technique for measuring the interactions between core-shell electrons. It uses lower energy than related technique Extended X-ray Absorption Fine Spectroscopy (EXAFS), and involves the excitation of core electrons to the Lowest Unoccupied Molecular Orbital (LUMO). The movement of the electrons between orbitals will occur at a defined x-ray energy for each transition, and so at the point when a large increase in absorption is observed, the electronic transition caused by the incident x-ray can be deduced. This means that properties such as the oxidation state of the atom, and the identity of any bonded atoms can be identified [77].

Synchrotron radiation can also be used to gather information about the cellular localisation of elements within a sample. This is done using the technique of X-Ray fluorescence (XRF) spectroscopy. Of course following excitation of an electron due to absorption of an x-ray, there must be a decay mechanism to return the atom to its ground state. The fluorescence caused by this decay is again characteristic for each element, and so by recording the fluorescence spectrum at hundreds of discrete locations across the sample allows for the simultaneous detection of all elements within the detection range. By then assigning each spectrum to a pixel within an image, maps showing the distribution of each element are produced.

### 3.4.2 Examples of compound investigation using synchrotron radiation

Synchrotron radiation is particularly useful for the investigation of compounds because of the ability to detect elements at low concentrations, and also the ability to detect multiple elements in one measurement.

X-Ray Absorption Spectroscopy (XAS) has been utilised to probe the interactions between NAMI-A and bovine serum albumin (BSA), prompted by the results of Phase I clinical trials suggesting NAMI-A was found in the blood plasma of patients [33]. A technique such as X-Ray Absorption Spectroscopy (XAS) is ideal for investigating a ruthenium compound within biological samples as the ruthenium identified can only be attributed to the compound. By using XANES, Ascone *et al.* have been able to show that the ruthenium centre of NAMI-A remains at a 3+ oxidation state following binding to BSA, with the chlorine environment most significantly changed [78].

Following on from this, Lay *et al.* have used synchrotron radiation to investigate the cellular effect of KP1019 and NAMI-A within liver cancer cells [79]. This work corroborated that NAMI-A forms several adducts with serum albumins. Interestingly, it was concluded that the XAS spectra of NAMI-A and an eqimolar amount of BSA was not significantly different from the spectra obtained when KP1019 was combined with BSA, with substitution of chlorine ligands on both compounds leading to binding to the protein. A further interesting conclusion was the observation that KP1019 appears to decompose when left for 4 hours in serum-enhanced media. This lead to a 50% decrease in uptake of ruthenium into liver cells than compared to cells treated with a 'fresh' solution of compound, whilst low levels of ruthenium were found in samples treated with NAMI-A, again reinforcing the hypothesis that NAMI-A's effectiveness is not due to a cellular uptake.

### 3.4.3 Examples of cellular imaging using synchrotron radiation

The applicability of synchrotron radiation for the use of imaging cells was beautifully demonstrated by McRae *et al.* who used the technique to map the elemental distribution of metals in a cell undergoing mitosis, and were able to show that cellular levels of zinc almost treble during mitosis [80]. The use of synchrotron radiation to image compounds within cells was comprehensively reviewed by [81] in 2007. Since then, there have been several more examples of synchrotron radiation being used to image metallodrugs within cells, such as [82] and [83]. Of particular relevance to this work, imaging studies have also been used to conclude that NAMI-A is not taken up into neuroblastoma cells SH-SY5Y [13]. Images obtained by Aitken *et al.* (using XRF at Advanced Photon Source, 2-1D-D, Chichago at an energy of 22.5 keV) are shown in Figure 3.15. By studying elemental co-localisation, it was determined that the ruthenium taken into the cells was coincident with areas of high phosphorus concentration, suggesting the ruthenium is delivered to the nucleus. The area of high phosphorus concentration is taken to be the nucleus as the phosphate backbone of DNA would be the main site of phosphorus found within the cell.

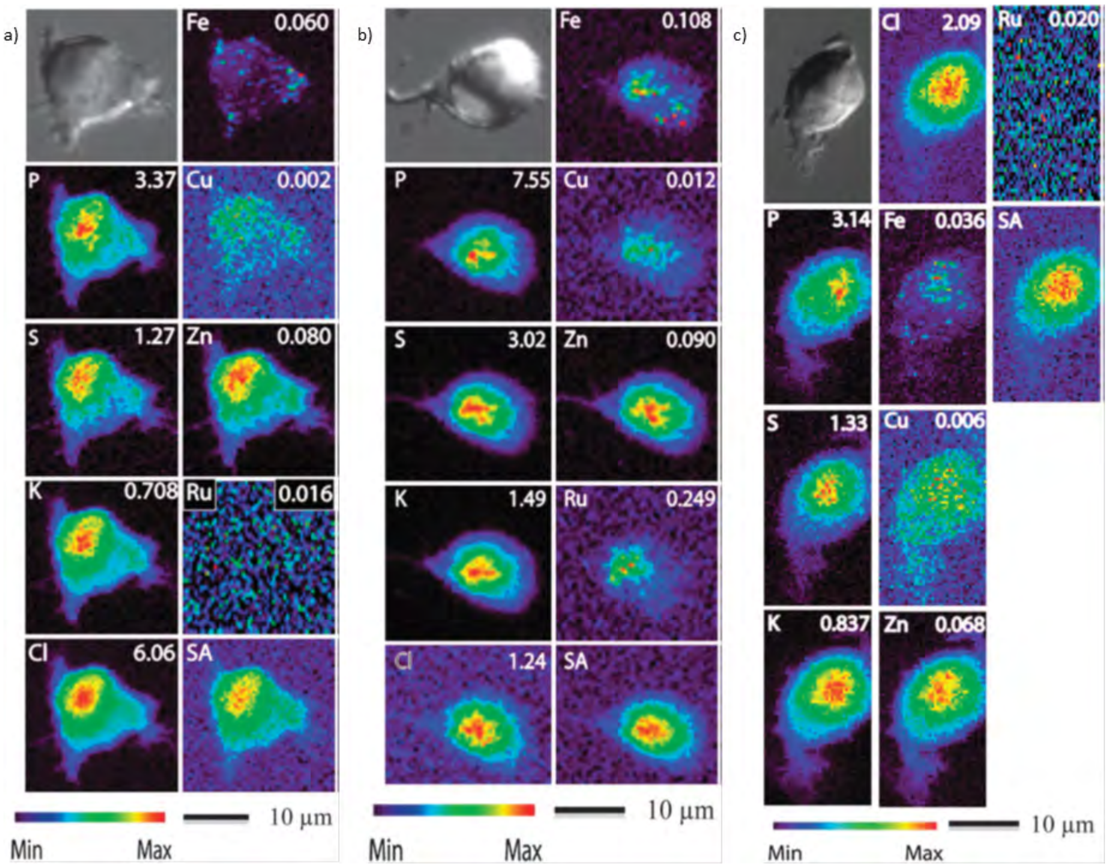

**Figure 3.15:** Brightfield image and elemental maps for a) untreated SH-SY5Y cells, b) SH-SY5Y cells treated with KP1019 and c) SH-SY5Y cells treated with NAMI-A. For all images, the element mapped is shown in top left corner where SA denotes absorption from scattered x-rays. All images reproduced with permission from Figures 1,2 and 4 in [13]

### 3.4.4 Using synchrotron radiation for imaging of cylinders

All imaging experiments described so far show fluorescence that has been attributed to the cylinder but these experiments do not allow for any chemical information about the cylinder to be gathered. If elemental maps of cellular samples treated with $[Ru_2L_3]^{4+}$ can be obtained, these could be an excellent complement to the confocal fluorescence microscopy images presented earlier. The elemental mapping of cells can also reveal the location of cell organelles, for example an area of zinc and phosphorus co-localisation is considered to be a good indicator of the concentration of zinc fingers proteins expected to be found within the nucleus. This allows imaging experiments to be taken a stage further from work already performed - if any ruthenium could be detected within a cellular sample, it may be possible to determine a discrete cellular location.

Also, the uptake mechanism of the iron cylinder may be able to studied using this approach. Many iron compounds are known to enter cells via the transferrin uptake pathway, which has several mechanisms, but receptor-mediated endocytosis of transferrin is the most understood [84]. The iron-free form of transferrin, apotransferrin, binds two Fe(III) ions to form ferrotransferrin. All cells express transferrin receptors and cancer cells have been shown to have elevated expression of the receptor compared to health cells [85]. At physiological pH, ferrotransferrin binds strongly to the transferrin receptor to initiate its internalisation via endocytosis. Once inside the acidic ($pH < 6$) late endosome compartment, the two Fe(III) ions are dissociated from ferrotransferrin (which now becomes apotransferrin again) and transported into the cytosol [86]. The apotransferrin remains bound it the transferrin receptor and is recycled at the cell membrane. This protein-ligand bond is unstable at pH values above 6 and hence the apotransferrin dissociates away from the receptor at the cell membrane, which is then free to bind to a new ferrotransferrin molecule. If it can be shown that iron at the membrane is only found in +2 oxidation state, then uptake of the iron cylinder by the transferrin pathway seems unlikely.

With the aim of imaging both ruthenium and iron cylinders within cells and producing XANES spectra of areas of metal concentration, work began on the I18 beamline at Diamond Light Source Synchrotron, which has already been used to study metals within breast cancer tissue [87]. Limits of detection on this beamline under the most optimal conditions has not been tested for every element, but it is estimated that the detection limits for transition metals would be high parts per billion (ppb) /low parts per millions (ppm) [88]. One ppm is taken as an estimate as this is the typical metal concentration in the reference standards used for evaluating XRF limits, and so detection limits equate to approximately Fe = 18 µM, Ni = 17µM, Ru = 10µM. As the cells to be imaged here are to be treated with 100 µM of cylinder, and the cylinder containing two metal atoms, the effective concentration of the elements of interest will be 200 µM, so the quantity of element present should not be a limiting factor on the ability to detect it within these samples. The ability to detect elements of interest at low concentrations is largely due to brilliance of the X-ray beams provided the synchrotron and the ability to focus the bright light to micron-sized dimensions. This has the effect of increasing the photon flux delivered to the sample, dramatically increasing the number of X-ray  element interactions per second. The ability to focus the incident beam to a spot size of known dimensions also permits sensitive spatially resolved mapping of elements. Since the monochromater enables the X-ray energy and bandwidth to be tuned, the excitation conditions at the sample can be altered to maximise the chance of detecting a particular element amongst a background of other elements. This can be achieved, for example, by tuning the monochromator to output a beam of a very narrow energy range centred about a particular transition energy for the element of interest. Conversely, varying the focus of the beam will change the flux density of photons incident on the sample as the same number of photons are distributed over a different sized area, and this would reduce the detected signal over the same measurement period and hence reduce sensitivity.

### 3.4.5 Sample Preparation

Two sample preparation methods were initially investigated - freezing cells grown directly on quartz or embedding samples within resin following a protocol as described in [89]. Freezing cells directly on the surface they were grown on allows the cells to grow to their natural size and shape, and removes the need of any chemical fixative which could suppress any signal from our sample. However there are no literature reports of attempting to fix these cell lines using freezing so it was not known if this method of sample preparation would alter the cell morphology or even detach the cells from their substrate. Embedding cells in resin is a much more widely used technique as it is routinely used in the preparation of electron microscopy samples. However, this preparation method involves detaching the cells from their growth surface and using gluteraldhyde fixatives which ideally would be avoided, due to their slow fixation rates and ability to react with free amines within the cell. Detaching the cells also causes them to contract in size and so taking sections of the resin runs the risk of missing the cells completely or taking a section of only the very edge of a cell.

Initially, two cell lines were investigated, MDA-MB-231 and A2780. Samples were grown on quartz slides, with silicon rings being used to define the cell growth area. Cells were left to adhere for 24 hours before being treated with cylinder. The cells were only treated for two hours, as treatment with any longer may have resulted in cell death which would have lead to a narrow scope of cell imaging experiments. The slides were then frozen by plunging in $CO_2$ cooled acetone. Once frozen, samples were stored at -20°C until required for imaging. Resin embedded samples were prepared by growing cells in 6-well plates and treating with cylinder before detaching the cells using trypsin and spinning them into a pellet before re-suspending in gluteraldehyde. Cells were left in the fixative overnight before being embedded in resin by Dr Paul Stanley at the Centre for Electron Microscopy, University of Birmingham.

### 3.4.6 Initial Results

Optical imaging of the samples were acquired using an Olympus reflected light microscope prior to imaging on the beamline. These showed that almost no MDA-MB-231 cells had adhered to the quartz slides, and very few A2780 cells could be observed. The slides had been checked prior to freezing, and adherent cells had been observed so it was determined that the freezing process had caused many of the cells to detach. Improving the freezing protocol was therefore highlighted as future work. Once the samples had been inserted into the beamline, optically observing the cells became problematic due to the requirement to place an Ultralene film over the sample for health and safety reasons. The film is a simple hydrocarbon, with formula $C_4H_4$, meaning that there was no potential for any signal from the film to be mistaken for signal from the cylinder. The film did however allow for monitoring of the location of the beam which scorched the film while rastering across the sample, making it straightforward to align the beam with the microscope image. All beamline work with MDA-MB-231 samples confirmed that no cells were present on the quartz slides, so efforts concentrated on A2780 samples. Elemental maps were obtained of areas showing strong co-localisation of calcium, zinc, potassium, iron and chlorine - elements that are routinely found within cells.

### 3.4.7 Further Development of Imaging Protocol

To overcome the sample preparation problems that were encountered during the first experimental run, modifications to the original sample protocol were investigated, as well as the use of a new substrate - silicon nitride windows. The silicon nitride windows have been used in several published articles [13], [90] and [91] and it was hoped the new substrate would allow for improved growth of both MDA-MB-231 and SKOV-3 cells.

The silicon nitride windows were used by placing them in 6-well plates before cell and media were added. Inspection of the wells using light microscopy showed that cells began to adhere to the windows within two hours of being added. Whilst the silicon nitride windows were an excellent growth substrate, their fragile nature made them difficult to handle.

Therefore modifications to the protocol of growing cells on quartz were investigated. It was decided to coat the quartz slides with a protein prior to adding cells in the hope of promoting cell adherence. Coating the slides with foetal bovine serum (FBS) lead to improved adherence of SKOV-3 cells, but did not lead to any adherence of MDA-MB-231 cells. Coating with collagen however lead to adherence of both cell lines upon the quartz slides, which meant that it was now possible to prepare samples on both quartz and silicon nitride to investigate any differences between growth substrate. It was noted that the elemental maps of cells grown on collagen coated slides show high levels of zinc across the slide, believed to be due the metalloproteases found within collagen. This however could be used as a good negative contrast for confirming the presence of cells on a slide.

The final modification to cell preparation was to alter the freezing process by changing the freezing medium to dry ice cooled methanol as opposed to acetone. As methanol is commonly used as a cell fixative this seemed a sensible choice and no noticeable detachment of cells was caused by the freezing process. All samples were therefore frozen using this method.

The imaging of samples was a two stage process - firstly the slide was imaged optically using a Zeiss confocal microscope, in order to find an area of cells suitable for imaging on the beamline. The co-ordinates of this position were noted, meaning that it was easy to find the relevant area once the sample was inserted into the beamline. A beam of approximately 2x5 μm was used to map areas of the order of 200 x 200 $\mu m^2$ allowing the localisation of a number of cells per slide. A beam energy of 11 keV was used for all mapping studies. This energy allows simultaneous detection of the cylinder metals but also the endogenous elements that help confirm the location of the cells in the surrounding matrix (eg Cl, Ca and Zn). Photographs of the experimental set up are shown in Figure 3.16. Previous attempts at imaging were limited by the need to use Ultralene film, following consultation with Dr Tina Geraki, Diamond Light Source, it was not deemed necessary to use this film for any of the samples used from this point onwards, and so all samples shown below were recorded without the presence of any film/coating on top of the sample. A helium cryojet was also now available, which meant it was possible to maintain the samples as frozen during the data acquisition process.

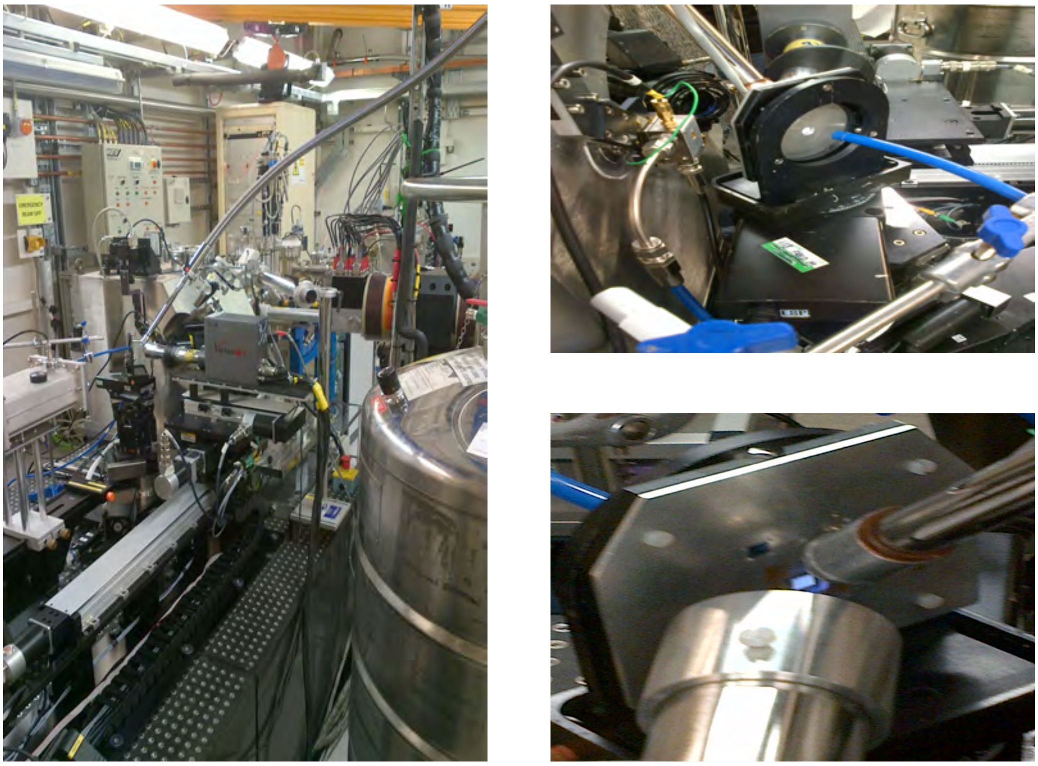

**Figure 3.16:** Images of experimental set up at I18 beamline. Left - view of experimental hutch, facing towards the beamline. Right - Rear (top) and forward facing (bottom) views of sample *in situ*. The blue pipe blows cooled nitrogen to the rear of the sample, the thinner outlet in the bottom right image is a helium cryojet - both of these are to keep the sample cold. The large apparatus seen in the bottom right image is the detector, held at 45° to the sample.

Control samples of SKOV-3 cells grown on quartz were imaged to gain an understanding of the elemental distribution and levels in an untreated sample. Elemental maps and an optical image of cells are shown in Figure 3.17.

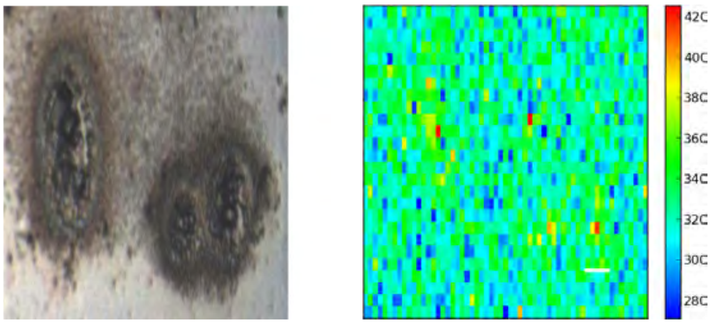

(a) Optical image (b) Fe map

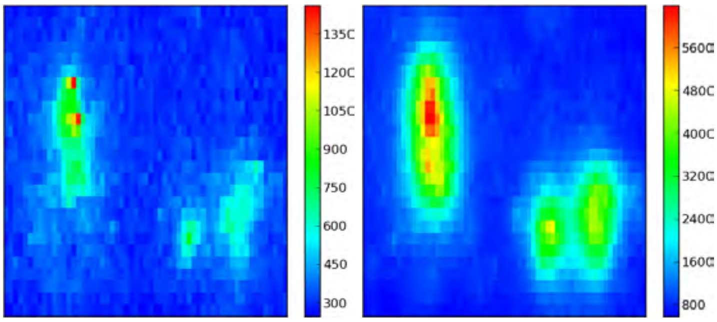

(c) Ca map (d) Cl map

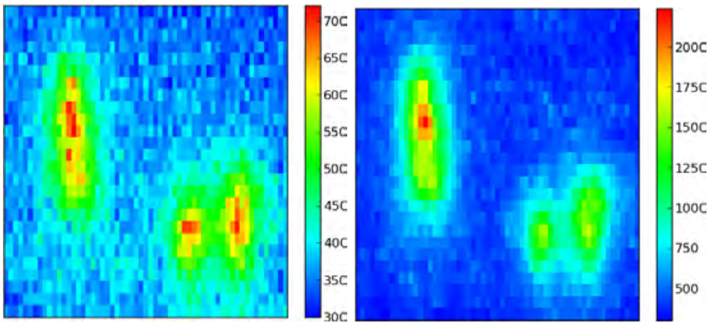

(e) Cu map (f) K map

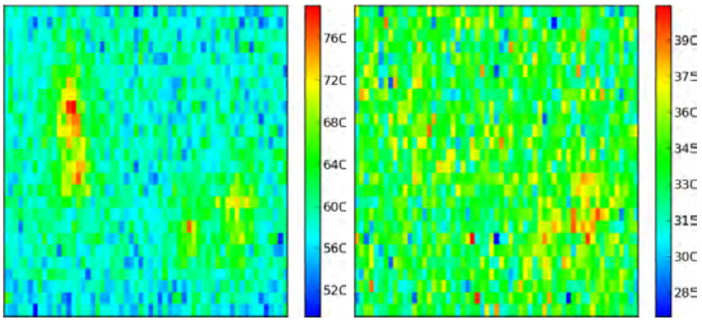

(g) Zn map (h) Ni map

**Figure 3.17:** Elemental maps and optical image of control SKOV-3 cells, which were grown on quartz following FBS coating. Scale bar represents 10 μm, intensity bar represents detected fluorescence photon count rate. The gating of all detected fluorescence to each element was performed by Dr Tina Geraki of Diamond Light Source.

The control images show that elements such as calcium, chlorine, copper, potassium and zinc can be seen as clearly localised within the cells. Unsurprisingly, nickel is seen in low levels and the levels found within the cells do not appear to be significantly higher than the surrounding area. More surprisingly, the elemental map of iron is very similar to that of nickel. As tumour cells are known to have more transferrin receptors than healthy cells, it was expected that the control elemental map would contain high levels of iron and would also be able to used to ‘mark’ the position of the cell. However, there is a converse argument that cancer cells are particularly active, and so have low levels of iron at any one time, so this observation of low levels of iron appears to support the second hypothesis.

Following collection of control data, attention turned to imaging SKOV-3 cells treated with iron cylinder. Images collected of a SKOV-3 cell treated with iron cylinder having been grown on a silicon nitride window are shown in Figure 3.18.

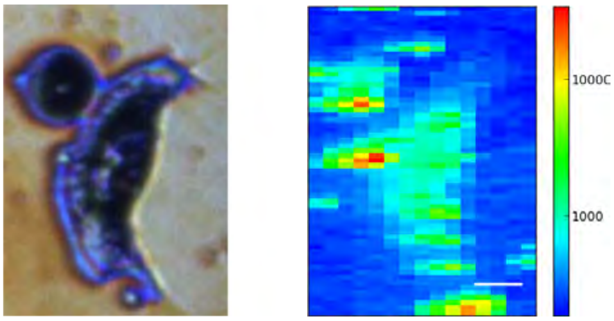

(a) Optical image (b) Fe map

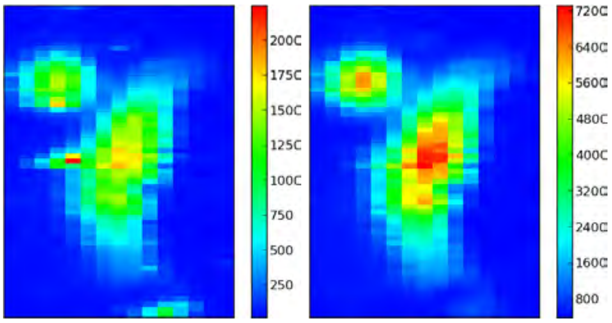

(c) Ca map (d) Cl map

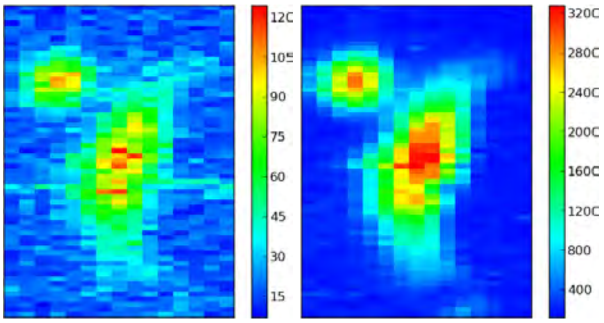

(e) Cu map (f) K map

**Figure 3.18:** Elemental maps and optical image of SKOV-3 cells grown on $Si_3N_4$ windows, and then treated with $[Fe_2L_3]^{4+}$ cylinder. Scale bar represents 10 μm, intensity bar represents detected fluorescence photon count rate. The gating of all detected fluorescence to each element was performed by Dr Tina Geraki of Diamond Light Source.

As per the control images, elements such as calcium and chlorine clearly show the location of the cell. Whilst all other elemental maps are shown on linear scale, the iron map is shown in logarithmic scale for clarity. It is clear that there are increased levels of iron within the cell, and a noticeable ‘hot spot’ of iron present at the cell membrane. This area appears to coincide with a vesicle that can be seen at the membrane of the cell in the optical image.

XANES scans were performed on the area of high iron concentration to determine the oxidation state of the Fe. This proved to be very problematic as the regions being looked at were often smaller than the beam diameter. However, we appear to be seeing a mixture of Fe(II) and Fe(III) oxidation states within the vesicles. This suggests that either the cylinder is changing oxidation states (which is consistent with the cylinder binding to the transferrin glycoprotein), or there are other Fe containing compounds within the cell/media.

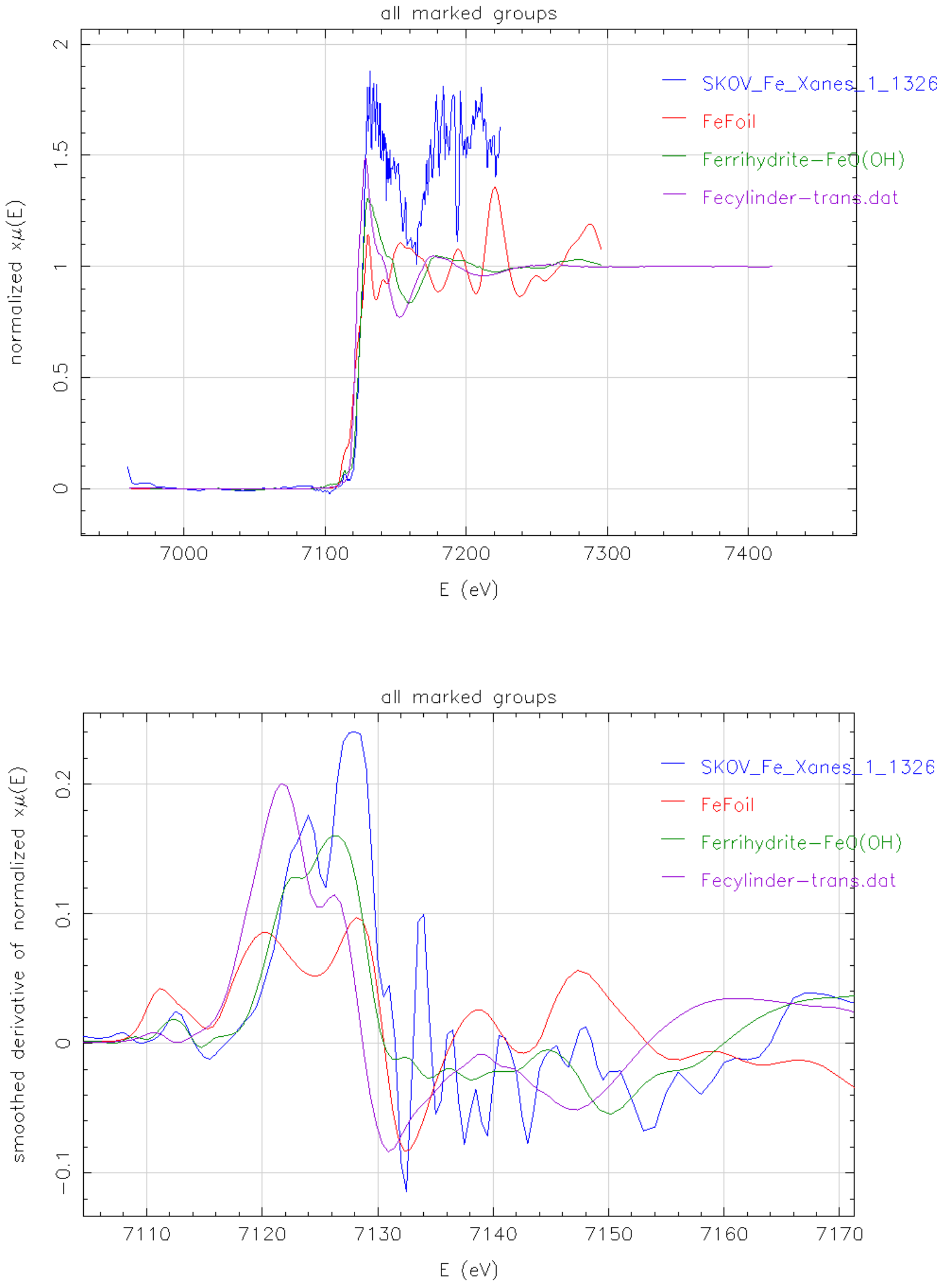

**Figure 3.19:** XANES spectra of Fe 'hot spot' within SKOV-3 cell (blue), $[Fe_2L_3]^{4+}$ pellet (purple), Fe foil (red) and ferrihydrite (green); post background removal (top) and in derivative form (bottom).

To further review the apparent mixture of Fe(II) and Fe(III) states being observed, linear combination fitting of the ferrihydrite and cylinder standards as shown in Figure 3.19 has been performed within Athena software [92]. The resulting fit is shown in Figure 3.20 below.

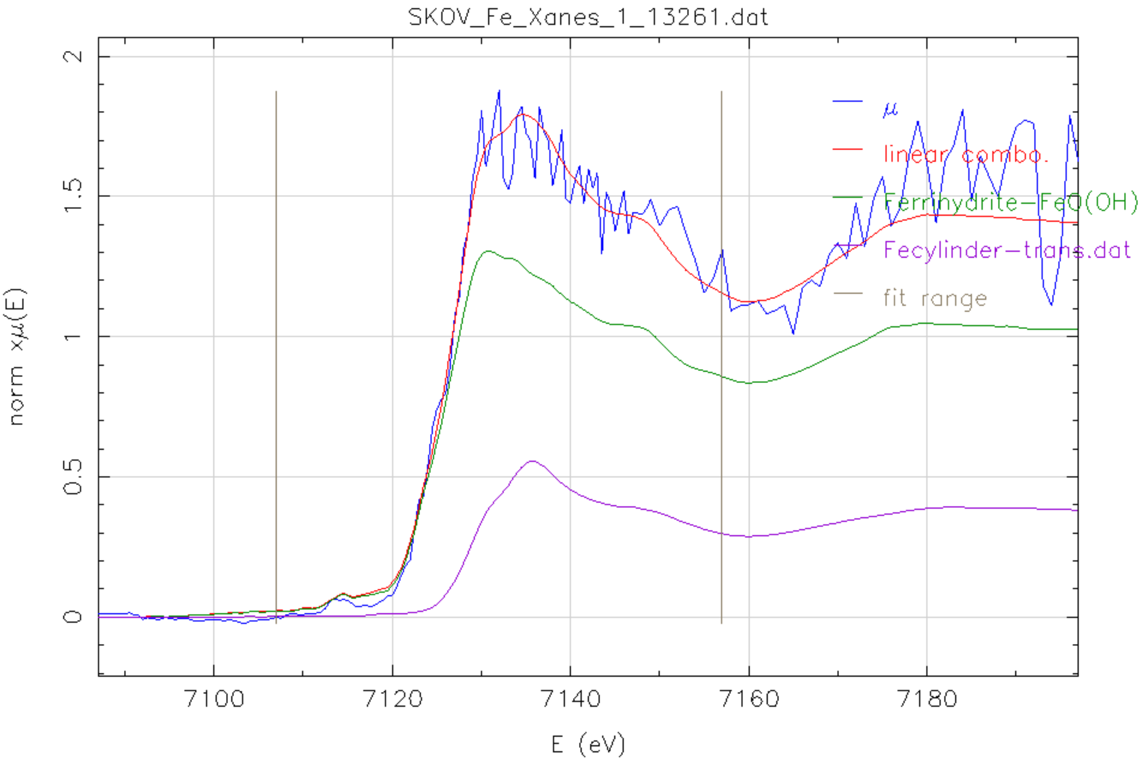

**Figure 3.20:** Standards of ferrihydrite (green) with a weighting of 1.00 and Fe cylinder powder (purple) with a weighting of 0.374 were used in a linear combination analysis (red) and fitted to the signal observed from Fe hotspot (blue). The results of the linear combination analysis showed that the hot spot contained mainly Fe(III) species, with some Fe(II). A reduced chi squared value of 0.867 was returned from this analysis.

As determined within Athena software, the linear combination was found by combining the entire ferrihydrite standard with 0.374 of the powdered cylinder sample. This shows that the hotspots are predominantly Fe(III), but around a quarter (27.2%) of the iron found within this region is Fe(II). A reduced chi squared value of 0.867 was returned from this analysis (as determined within Athena software), showing a good fit of the data. As part of the linear combination process, the standard of iron foil was included within the list of standards with which Athena should perform the linear combination, but the closest fit to our sample was found to not contain any contribution from the iron foil standard.

Following on from this, SKOV-3 cells also treated with iron cylinder but grown on quartz were imaged, the resulting images are shown in Figure 3.21.

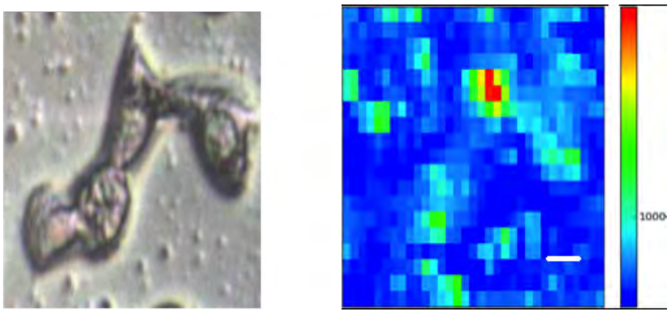

(a) Optical image (b) Fe map

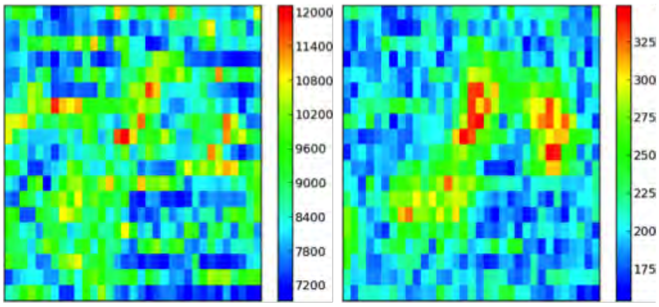

(c) Ca map (d) Cl map

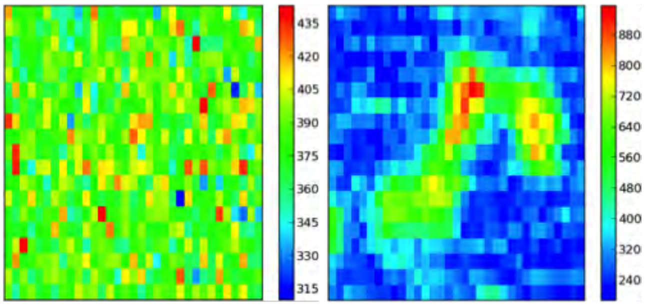

(e) Cu map (f) K map

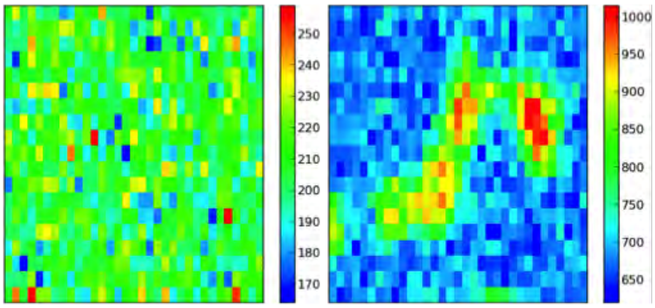

(g) Ni map (h) Zn map

**Figure 3.21:** Elemental maps and optical image of SKOV-3 cells grown on quartz following FBS coating, and then treated with $[Fe_2L_3]^{4+}$ cylinder. Scale bar represents 10 μm, intensity bar represents detected fluorescence photon count rate. The gating of all detected fluorescence to each element was performed by Dr Tina Geraki of Diamond Light Source.

As with the samples grown on silicon nitride, there is a noticeable increase in iron levels within the cell following treatment with iron cylinder. Once again, the elemental map for iron is presented in a logarithmic scale for clarity and an iron 'hot spot' can again be seen close to the cell membrane. XANES scans again showed that this area contained a mixture of Fe(II) and Fe(III) compounds as had been seen in the cells grown on silicon nitride. It was therefore concluded that the growth substrate used has no discernible effect on the uptake of the iron cylinder into SKOV-3 cells.

During XANES scan acquisition, it was noted that the long dwell time on any particular point within a cell had a detrimental effect on the cell's integrity, as is shown in Figure 3.22. For the planning of future work using this technique, this observation implies that it may not be possible to collect XANES spectra of multiple regions of the same cell without questioning the validity of the later acquisitions.

**Figure 3.22:** Optical image of SKOV-3 cell shown in Figure 3.21 following acquisition of XANES spectra

Cells treated with nickel cylinder were imaged to compare localisation of this compound with that of the iron cylinder. The images acquired are shown in Figure 3.23. Note the optical image presented was acquired after elemental maps were acquired, and unfortunately the sample had been damaged by ice build up on the detector. The location of the cells can however be seen within the ice damage.

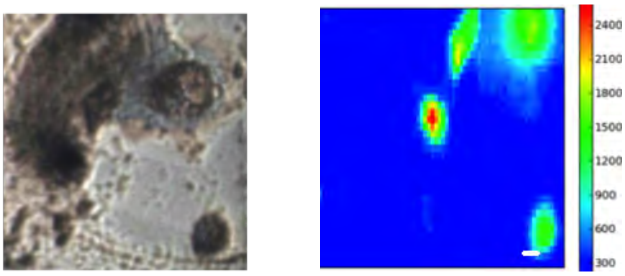

(a) Optical image (b) Ni map

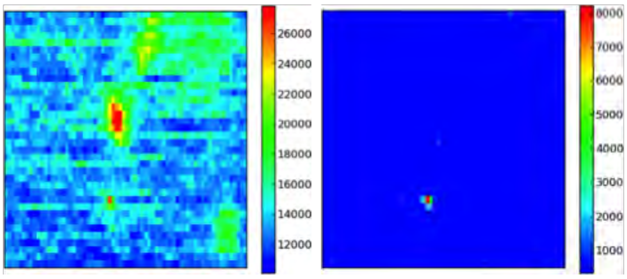

(c) Ca map (d) Fe map

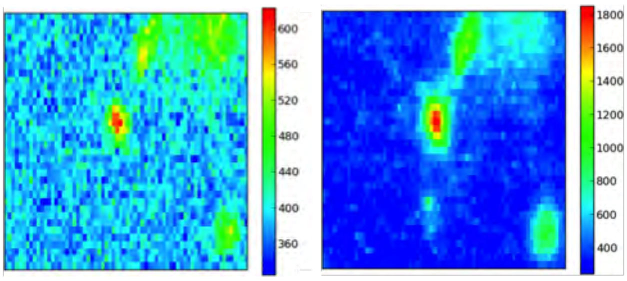

(e) Cu map (f) K map

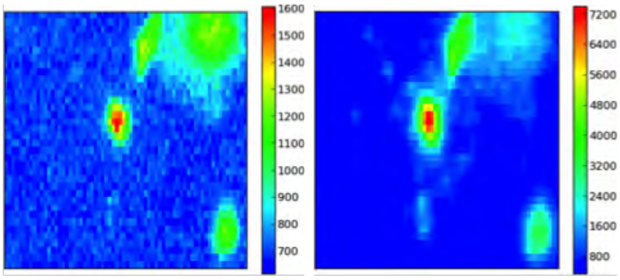

(g) Zn map (h) Cl map

**Figure 3.23:** Elemental maps and optical image of SKOV-3 cells grown on quartz following FBS coating, and then treated with $[Ni_2L_3]^{4+}$ cylinder. Scale bar represents 10 μm, intensity bar represents detected fluorescence photon count rate. The gating of all detected fluorescence to each element was performed by Dr Tina Geraki of Diamond Light Source.

It is immediately noticeable that there is an uptake of nickel into the cells when compared with the control image shown in Figure 3.17(h). The nickel is shown to be co-localised with the calcium and potassium, suggesting it is taken into the centre of the cell. What is interesting to note it that there is no sign of a nickel ‘hot spot’ at the cell membrane as there was for iron in the cells treated with iron cylinder. Whilst this on its own is not conclusive evidence that the cylinders are taken into the cells by different pathways, it is an intriguing result and repetition of these experiments as a time course study may reveal if the nickel localises at the cell membrane before being taken into the cell, and if the iron ‘hot spot’ seen eventually spreads in the cell cytoplasm or remains at the membrane.

XANES spectra of the nickel found within the cell were recorded and again compared to standards of nickel foil and a pellet of nickel cylinder, as shown in Figure 3.24. Spectra from two different cells were recorded and shown to be identical to each other, and very similar to the spectrum of nickel foil. The shoulder seen on the spectrum for powdered cylinder however is not seen in any of the other spectra, suggesting the nickel found in the cell is not in the same environment as the nickel at the centre of the cylinder.

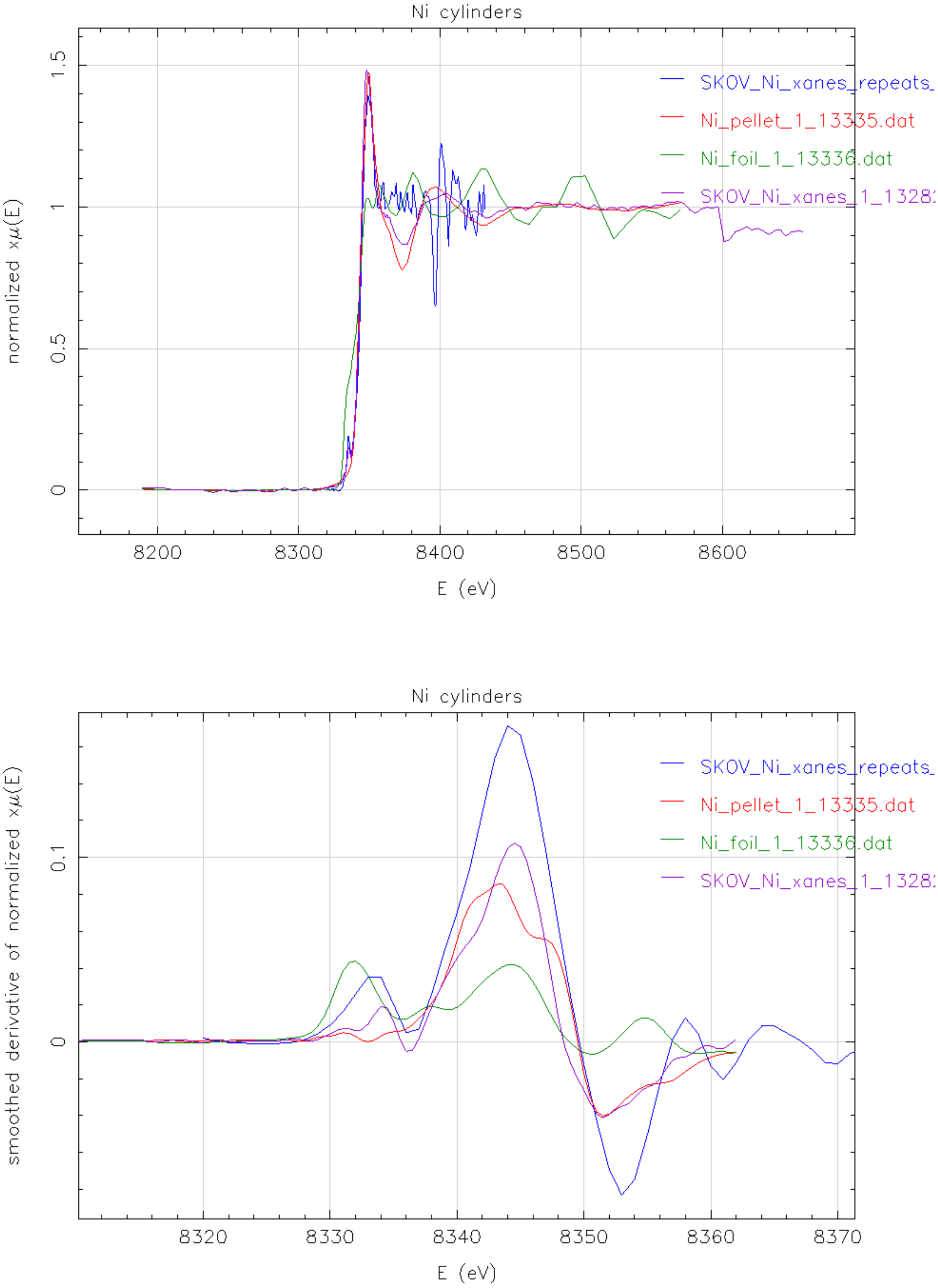

**Figure 3.24:** XANES spectra of Ni containing area within SKOV-3 cell (blue and purple), $[Ni_2L_3]^{4+}$ pellet (red), and Ni foil (green); post background removal (top) and in derivative form (bottom).

Attempts were also made to image ruthenium cylinder within MDA-MB-231 cells. This however proved difficult to perform due to the hardware available on I18 beamline. The K edge of ruthenium is 22117 eV, which is above the energy range obtainable at I18, where optics and wigglers are set up to focus the beam to lower energies to cover edges more commonly studied. The $L_1$ and $L_2$ edges of ruthenium have been detected at 3224 eV and 2967 eV respectively whilst the $L_3$ edge at 2838 eV [93]. Unfortunately, the $L_3$ edge is unresolvable from the chlorine K edge found at 2822 eV [94], and the $L_1$ and $L_2$ edges are only seen at much lower intensities so would be very difficult to confidently assign within a spectrum. A spectral subtraction process was undertaken to try and isolate a map due to ruthenium $L_3$ edge, but this was unsuccessful. It was therefore decided that work should concentrate on determining the cellular localisation of iron and nickel based cylinders.

### 3.4.8 Initial conclusions on data acquired

These initial attempts at cellular imaging of cylinders have led to the development of a suitable protocol for cell growth on silicon nitride windows and quartz slides. Treatment with iron cylinder has been shown to lead to ‘hot spots’ of iron at the membrane as well as within the cells, whereas nickel cylinder treatment leads only to nickel spread throughout the cell. It however is noted that due to damage to the samples during acquisition, a complete set of data of control, iron cylinder treated and nickel cylinder treated cells all grown on the same substrate could not be collected during the synchrotron beam-time allocated to this project to date. Any future beam-time access will be used (in combination with the experience gained from experiments performed here) to obtain this complete data for multiple cell lines.

Work so far has also shown how information about the oxidation state of metals found within cells can be investigated using XANES spectroscopy. However future experiments must be designed carefully to ensure that multiple XANES scans are not required from one cell due to the damage caused by spectrum acquisition.

# Chapter 4

# Investigating the effect of cylinder on cells

## 4.1 Investigating cells morphology and motility

It is not enough to just determine the cellular localisation of the cylinder compounds - their effects on cells must also be investigated to determine their full cause of toxicity. These effects can include cell morphology, motility and surface adhesion which can all be observed readily using microscopy techniques. Therefore phase contrast and fluorescence confocal microscopy have been used to observe the effects of cylinder treatment on two principle cell lines; MDA-MB-231 and SKOV-3.

### 4.1.1 Phase contrast imaging of MDA-MB-231 and SKOV-3 cells

Previous work within the group had begun investigating the effects of $[Fe_2L_3]^{4+}$ on the motility of MDA-MB-231 cells [14]. That work showed that $[Fe_2L_3]^{4+}$ caused changes in cell morphology even at time points where $[Fe_2L_3]^{4+}$ is known to be non-lethal.

To build on and expand this work, the effects of iron cylinder on the morphology and motility of MDA-MB-231 cells has been investigated using time-lapse phase contrast microscopy. Four analogues of the iron cylinder were synthesised to investigate the effect of changing the central $CH_2$ moiety of the ligand for hetero atoms such as oxygen ($[Fe_2L^O{}_3]^{4+}$) or sulphur ($[Fe_2L^S{}_3]^{4+}$), and also the effect of introducing a methyl group in place of the imine hydrogen ($[Fe_2L^{Me}_3]^{4+}$). The structures of these ligands are shown in Figure 4.1.

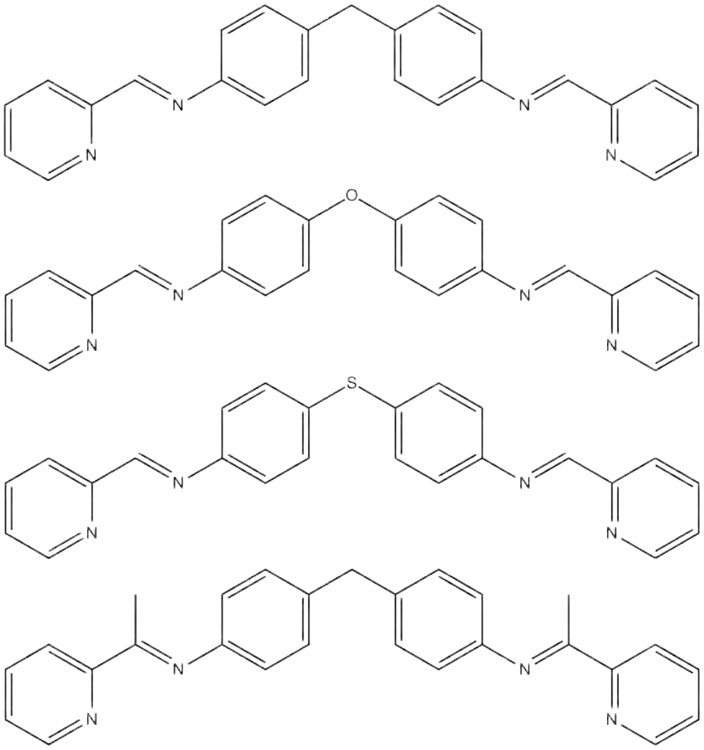

**Figure 4.1:** Structures of cylinder ligands, (from top to bottom) parent ligand (L), oxygen ligand ($L^O$), sulphur ligand ($L^S$) and methyl ligand ($L^{Me}$).

$[Fe_2L^S_3]^{4+}$ and $[Fe_2L^O_3]^{4+}$ have already been shown to bind to DNA 3-way junctions, but the $[Fe_2L^O_3]^{4+}$/DNA complex shows reduced thermal stability [95]. $[Fe_2L^{Me}_3]^{4+}$ however, has very different DNA binding results. Gel electrophoresis studies appear to suggest that less than 10% of the DNA is found in a three-way structure when treated with $[Fe_2L^{Me}_3]^{4+}$ compared with over 40% of DNA found when treated with $[Fe_2L_3]^{4+}$. Toxicology studies also show that $[Fe_2L^{Me}_3]^{4+}$ is inactive to concentrations up to 100 μM in A2780 ovarian cancer and MDA-MB-231 cells. This is in stark contrast to $[Fe_2L_3]^{4+}$ which shows toxicity comparable to cisplatin [14]. These results suggest a direct correlation between cylinder binding to three-way junction and cylinder toxicity.

Cells were seeded into 6-well plates, allowed to adhere for 24 hours before being treated with 100 μM of compound. The plate was then imaged using a phase contrast microscope with a heated stage and controlled $CO_2$ environment: Images were acquired every 5 minutes. From the videos obtained, it is apparent that addition of any of the compounds leads to an almost complete arrest in cell movement. Stills from the videos at t=zero, one, two, three and four hours are shown in Figure 4.2 to Figure 4.6. Over the 4 hours of the experiment, there are no obvious signs of cell death such as breakdown of the membrane or the cells detaching from the surface, so it is believed that the cylinder is having a specific effect on the cell motility, either by interaction with the cell cytoskeleton or by interrupting the signalling cascade. In the cells treated with $[Fe_2L_3]^{4+}$, the viability of the cells was confirmed by the observation of almost complete cell replication, wherein replication of the nucleus can clearly be observed but the two daughter cells seem to be incapable of separating. Two leading edges are formed, and the cells attempt to move in opposite directions but instead of separating, a long, thin spindle is formed between the two cells which ends in both cells suddenly moving back to their starting point. This was not observed in cells treated with the other three cylinders, but these seem to completely arrest the movement of some cells, with the cells observed at t=0 hour still in the field of view at t=4 hour, particularly for the cells treated with $[Fe_2L^O{}_3]^{4+}$. In contrast however, the cells treated with $[Fe_2L^{Me}{}_3]^{4+}$ do not show such a decrease in motility. This nicely correlates with the toxicity data, as the one cylinder we know does not bind to the DNA three-way junction and shows no toxicity at concentrations below 100 μM does not appear to have any effect of cell motility.

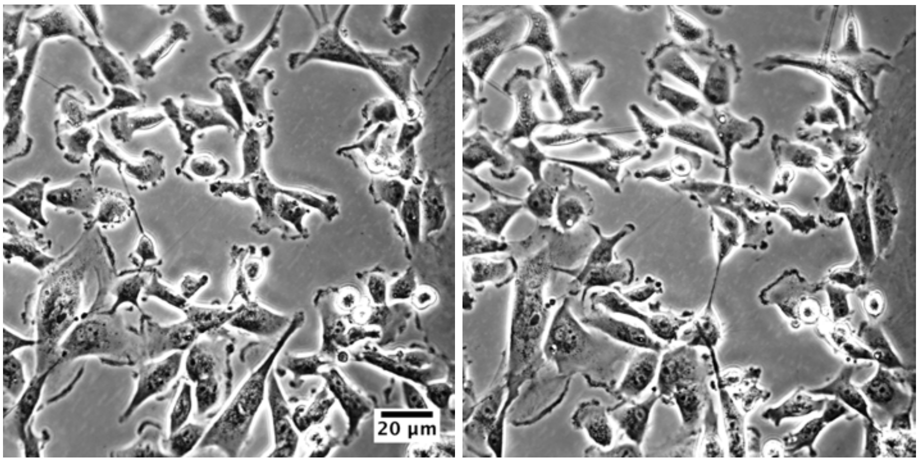

(a)
Zero
hour

(b)
One
hour

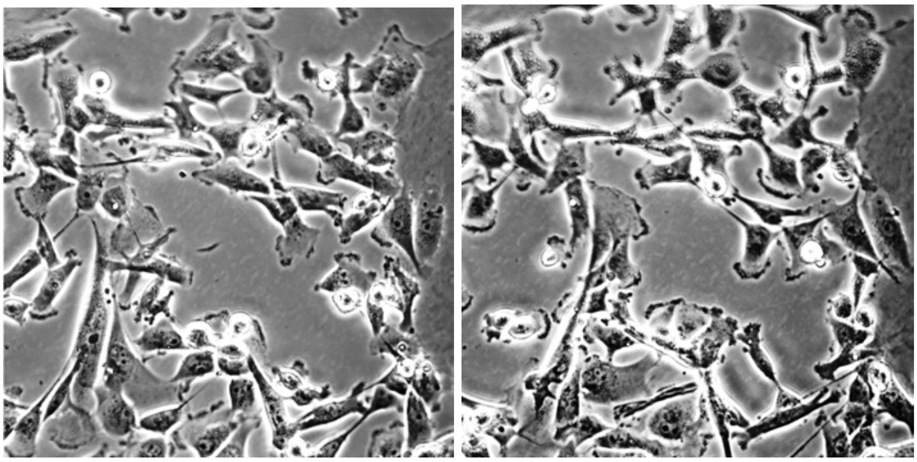

(c)
Two
hours

(d)
Three
hours

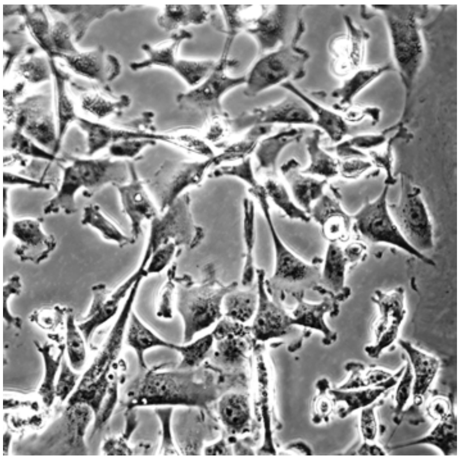

(e)
Four
hours

**Figure 4.2:** Time lapse images of untreated MDA-MB-231 cells, imaged over 4 hours. Clear movement of the cells is observed in between each frame.

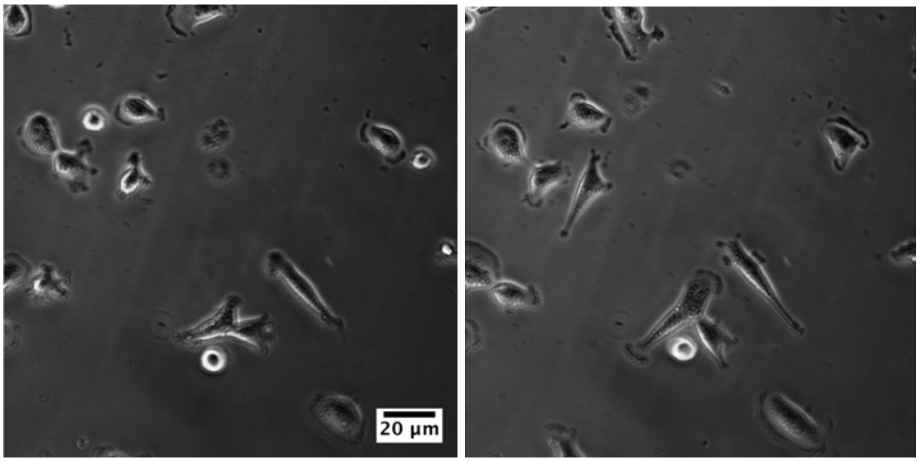

(a)
Zero
hour

(b)
One
hour

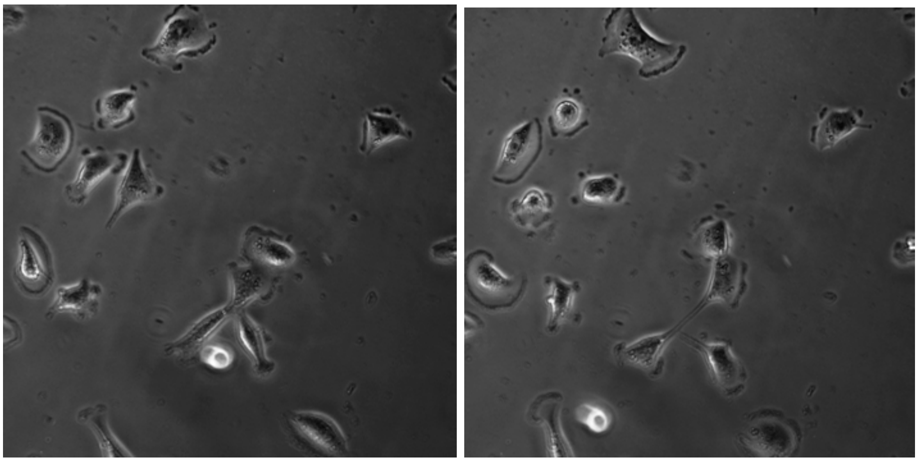

(c)
Two
hours

(d)
Three
hours

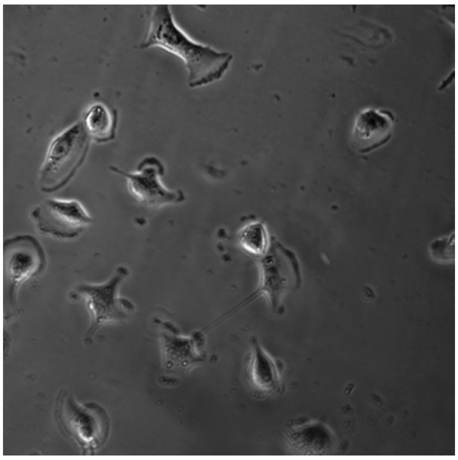

(e)
Four
hours

**Figure 4.3:** Time lapse images of MDA-MB-231 cells treated with 100 μM $[Fe_2L_3]^{4+}$, imaged over 4 hours. Little movement of cells is seen in between each frame.

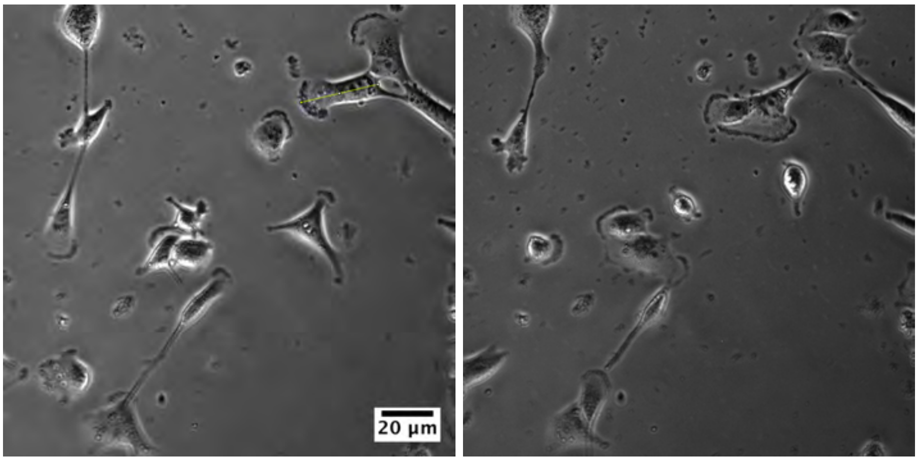

(a) Zero hour

(b) One hour

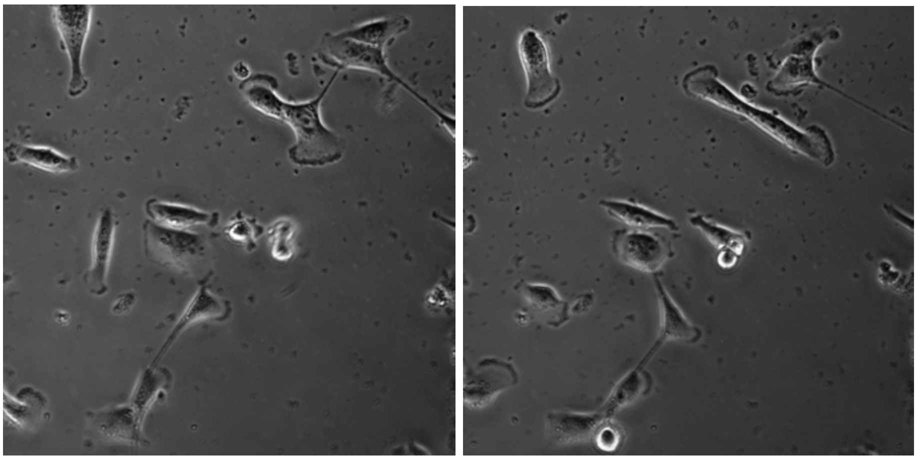

(c) Two hours

(d) Three hours

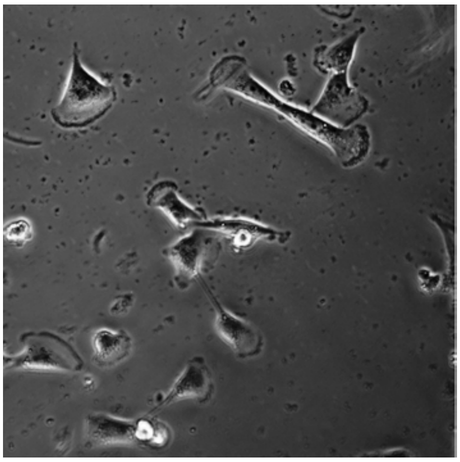

(e) Four hours

**Figure 4.4:** Time lapse images of MDA-MB-231 cells treated with 100 µM $[Fe_2L^{Me}{}_3]^{4+}$, imaged over 4 hours. No real arrest of movement was noted in these images, with cell division seen to be occurring.

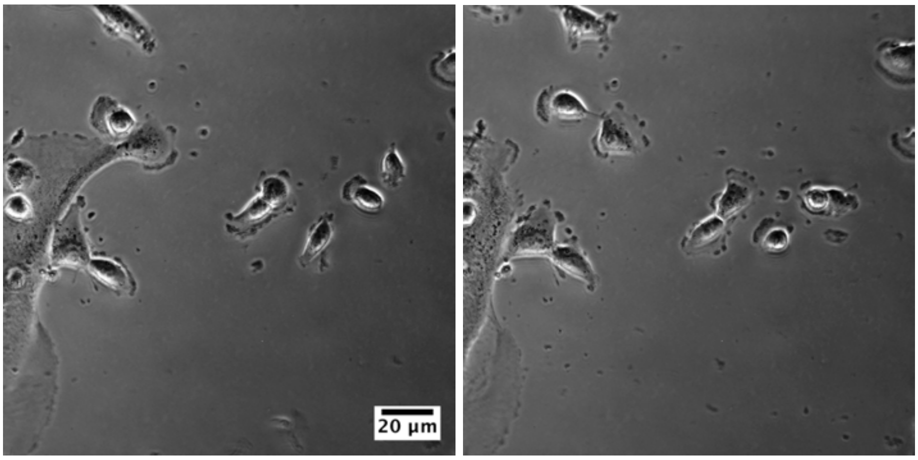

(a)
Zero
hour

(b)
One
hour

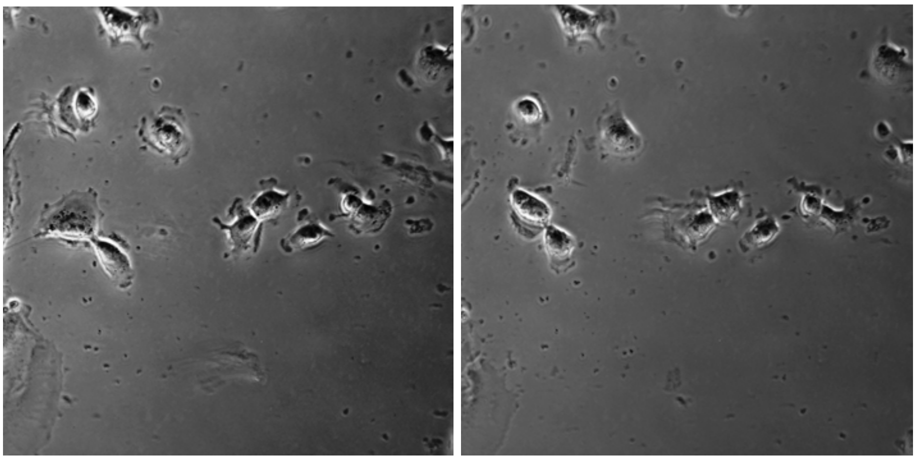

(c)
Two
hours

(d)
Three
hours

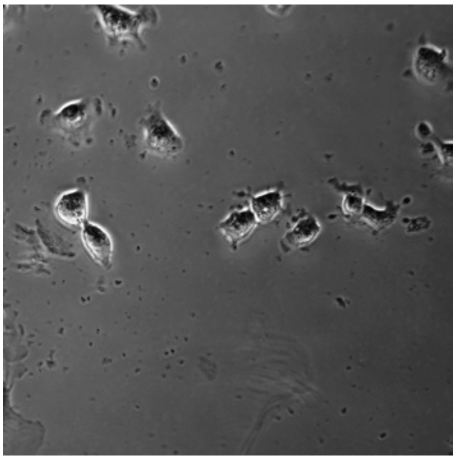

(e)
Four
hours

**Figure 4.5:** Time lapse images of MDA-MB-231 cells treated with 100 μM $[Fe_2L^O{}_3]^{4+}$, imaged over 4 hours. After one hour, very little movement of cells is observed.

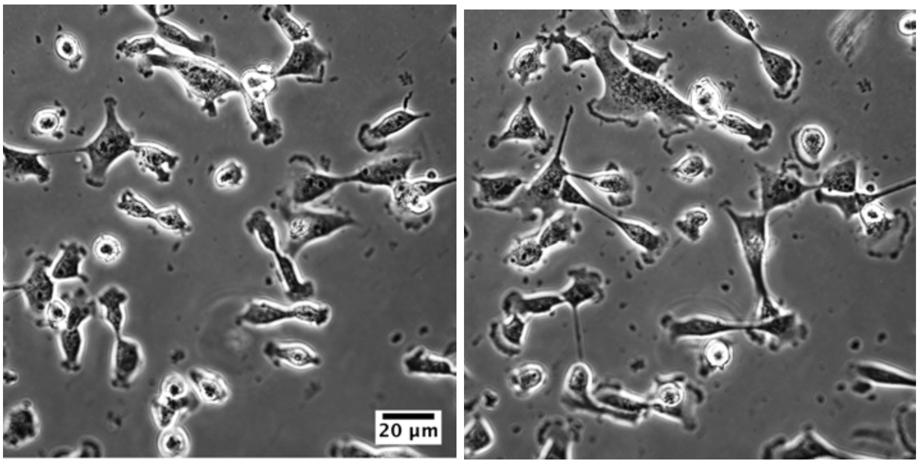

(a) Zero hour

(b) One hour

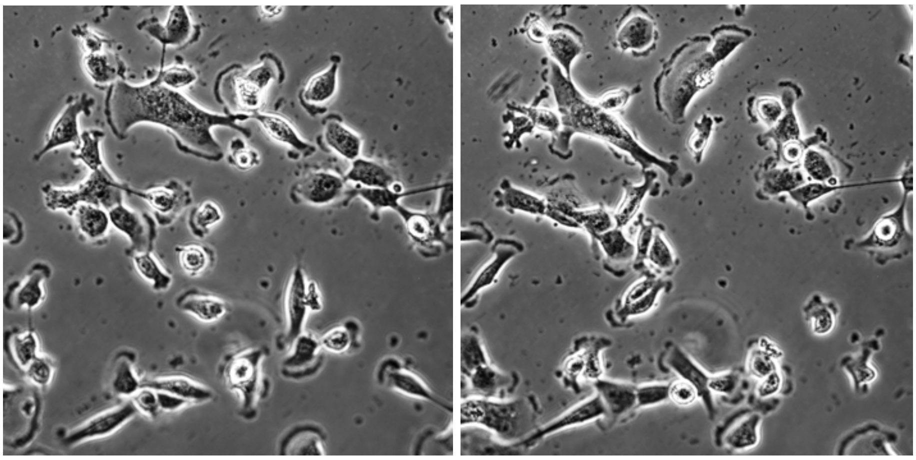

(c) Two hours

(d) Three hours

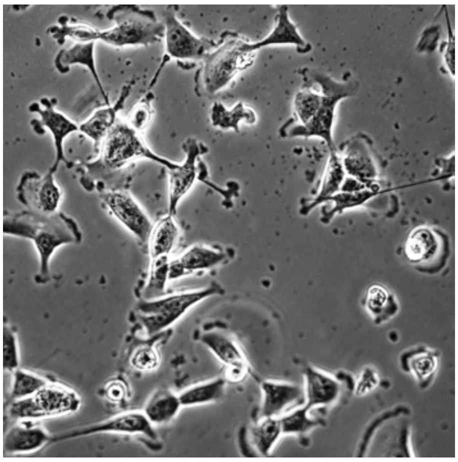

(e) Four hours

**Figure 4.6:** Time lapse images of MDA-MB-231 cells treated with 100 μM $[Fe_2L^S{}_3]^{4+}$, imaged over 4 hours.

This work was repeated with SKOV-3 ovarian cells to see if the cylinders arrested cell movement in a second cell line. Control images of untreated cells and cells treated with cisplatin were recorded and are presented in Figure 4.7 and Figure 4.8 respectively.

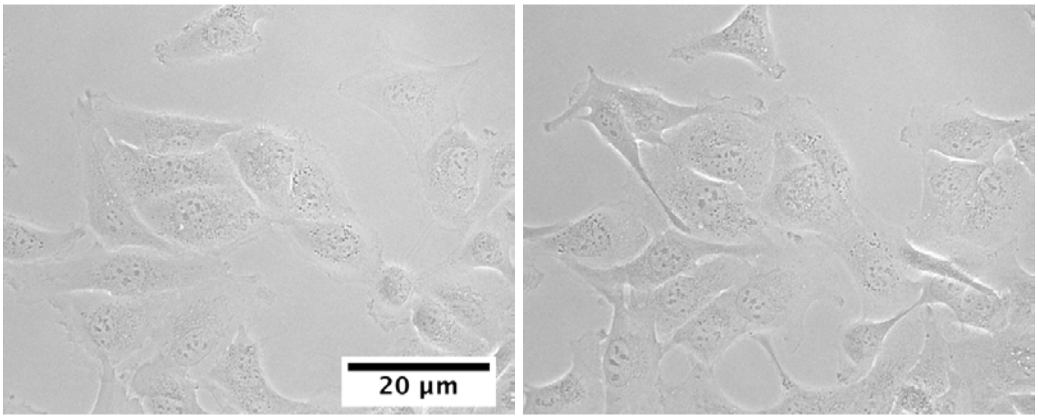

(a) One hour

(b) Two hours

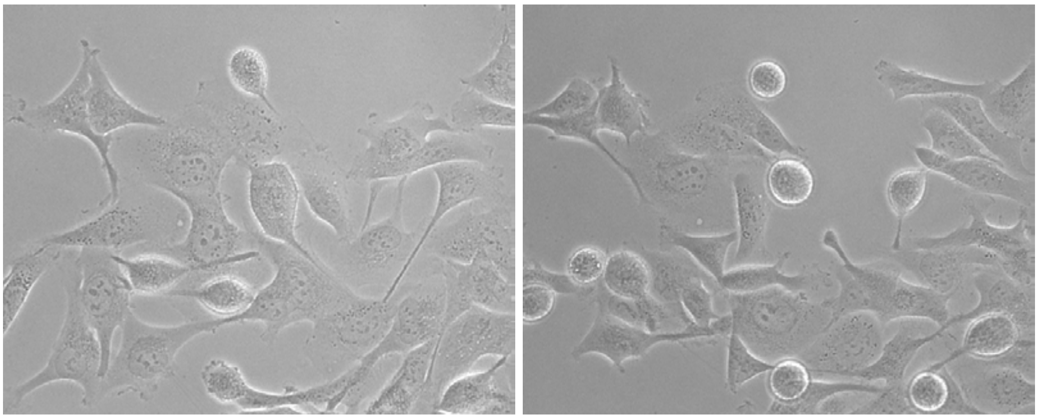

(c) Three hours

(d) Four hours

**Figure 4.7:** Time lapse images of untreated SKOV-3 cells, imaged over 4 hours. There is clear movement of the cells in between each frame.

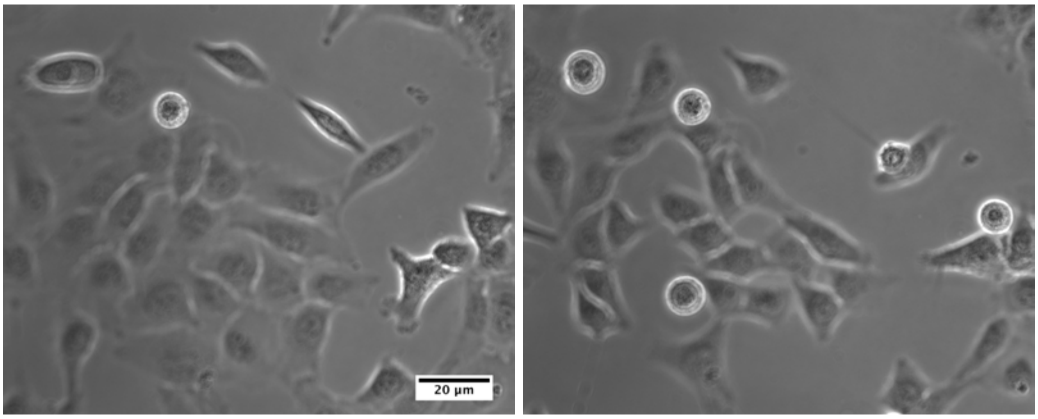

(a) One hour

(b) Two hours

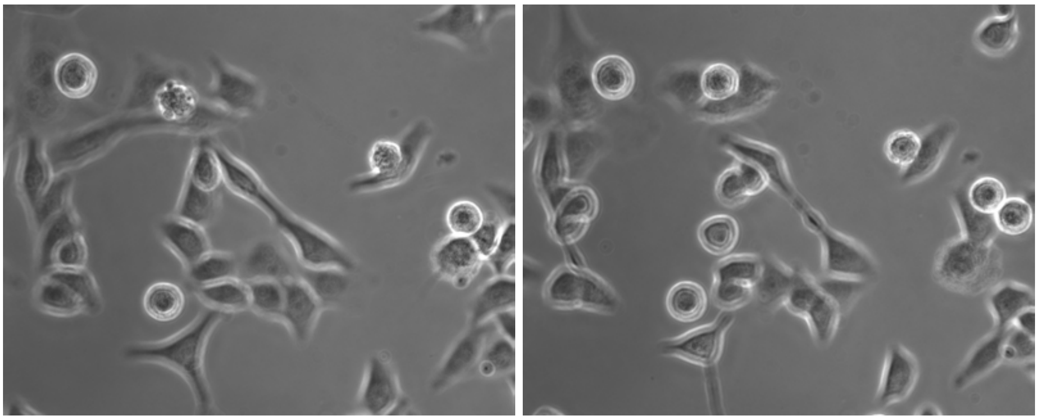

(c) Three hours

(d) Four hours

**Figure 4.8:** Time lapse images of SKOV-3 cells treated with 100 μM cisplatin (bottom row), imaged over 4 hours. By four hours, many of the cells appear to have entered apoptosis as they become spherical and begin to detach from the surface.

The untreated cells are seen in a large monolayer, and move freely within this. Cells treated with cisplatin initially remain moving within their monolayer before contracting, finally appearing to completely ‘ball up’. Imaging of cells treated with the four iron cylinders are presented in Figures 4.9 to 4.12.

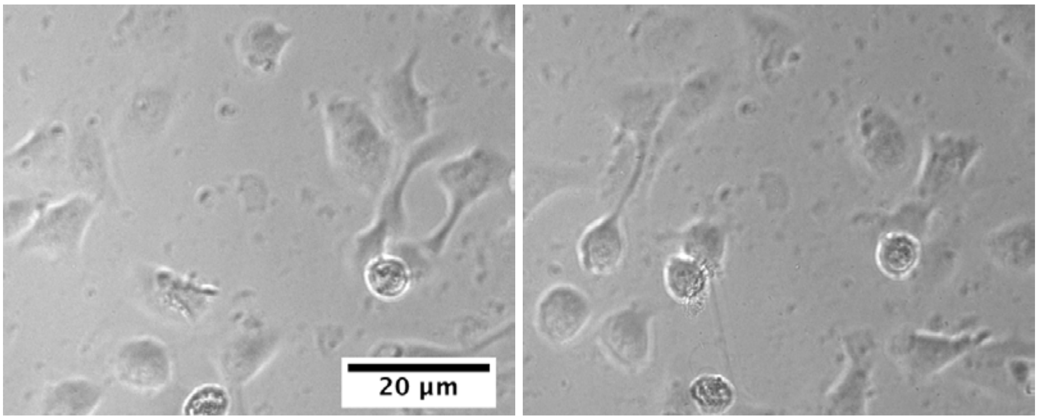

(a) One hour

(b) Two hours

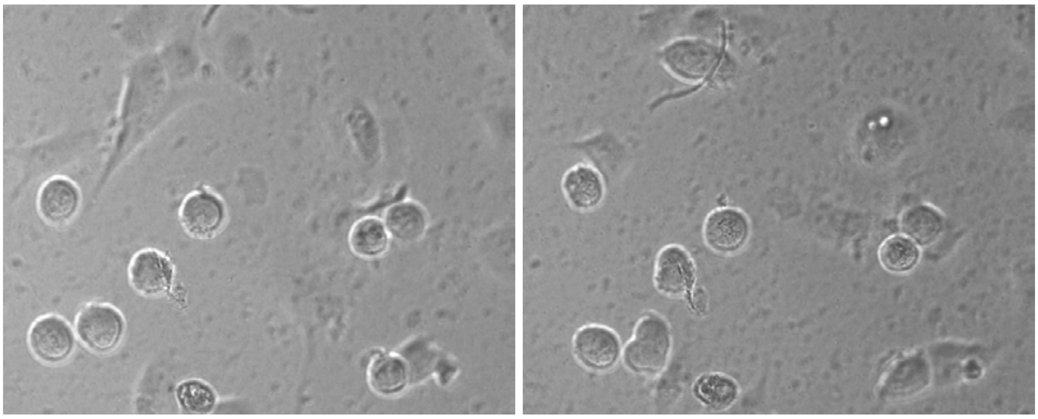

(c) Three hours

(d) Four hours

**Figure 4.9:** Time lapse images of SKOV-3 cells treated with 100 μM $[Fe_2L_3]^{4+}$, imaged over 4 hours. Little movement of cells is observed.

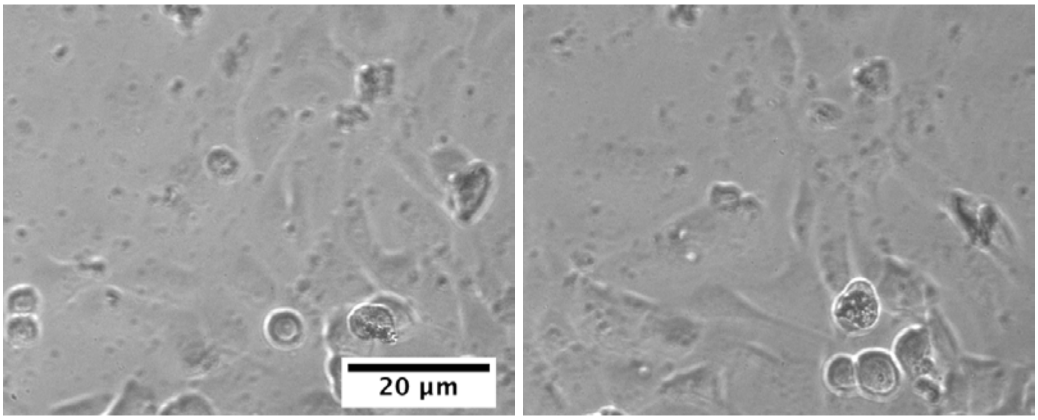

(a) One hour

(b) Two hours

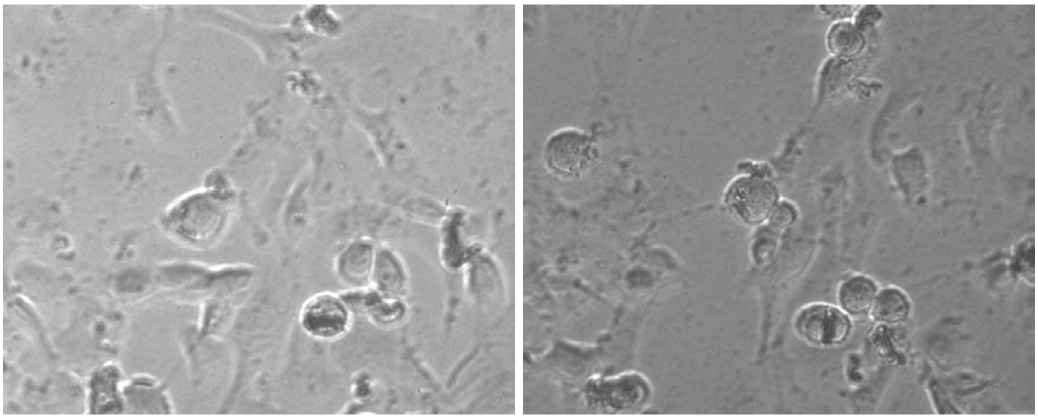

(c) Three hours

(d) Four hours

**Figure 4.10:** Time lapse images of cells treated with 100 μM $[Fe_2L^{Me}{}_3]^{4+}$, imaged over 4 hours. Little movement of cells is observed.

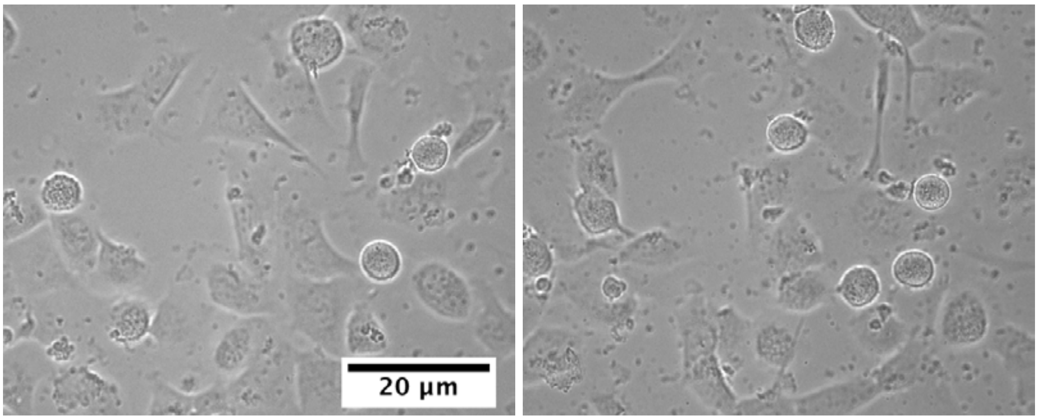

(a)
One
hour

(b)
Two
hours

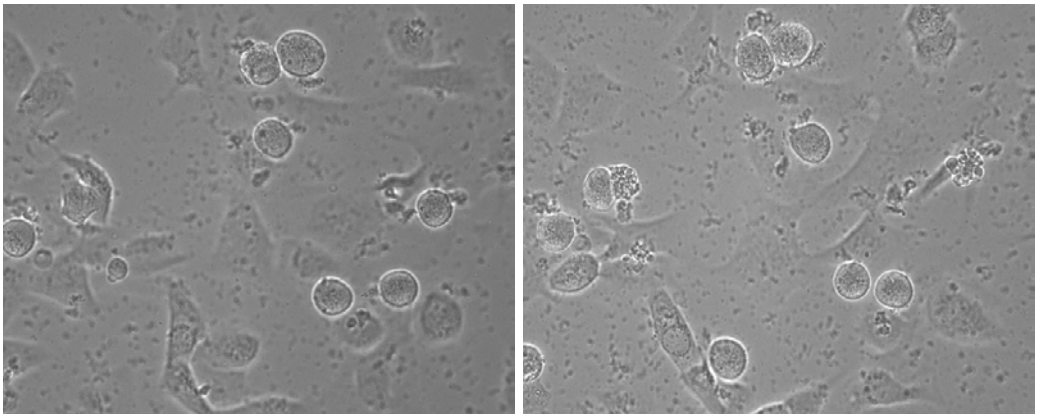

(c)
Three
hours

(d)
Four
hours

**Figure 4.11:** Time lapse images of cells treated with 100 μM $[Fe_2L^O{}_3]^{4+}$, imaged over 4 hours. Increasing cellular debris is noted, but a layer of cells with reduced movement are visible beneath.

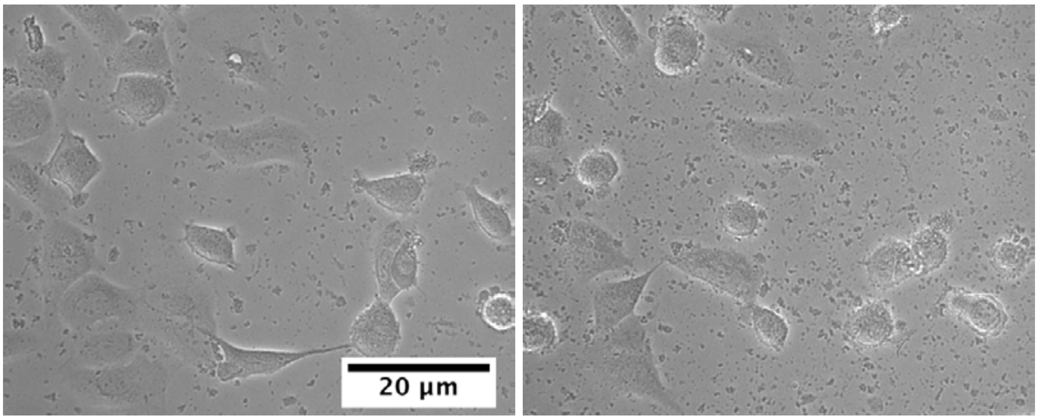

(a) One hour

(b) Two hours

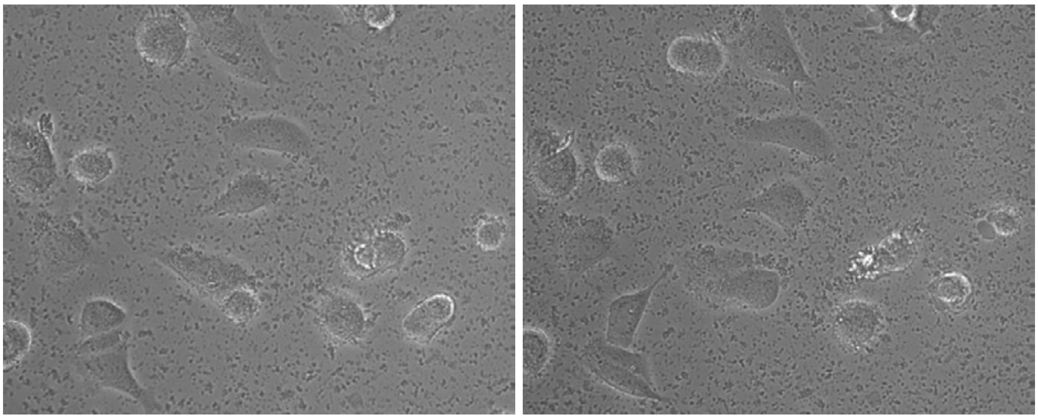

(c) Three hours

(d) Four hours

**Figure 4.12:** Time lapse images of cells treated with 100 µM $[Fe_2L^S{}_3]^{4+}$, imaged over 4 hours. A complete arrest of movement is observed, with increasing cellular debris.

Once again, it was seen that there was a decrease in cellular movement following cylinder treatment. SKOV-3 cells treated with $[Fe_2L_3]^{4+}$, $[Fe_2L^O{}_3]^{4+}$ and $[Fe_2L^S{}_3]^{4+}$ showed similar results to MDA-MB-231 cells when treated with these compounds - within 2 hours post treatment cell movement is almost completely arrested. Surprisingly, this decrease in cell movement is also seen following treatment with $[Fe_2L^{Me}{}_3]^{4+}$, the opposite of what is seen in MDA-MB-231 cells treated with this compound. It is not known what would cause this difference in effect, as it is known that $[Fe_2L^{Me}{}_3]^{4+}$ does not bind to DNA [14]. This result does however point to a explanation that all of the effects on cell motility (across both cell lines) are caused by an interruption to the signalling cascade, not by direct binding to DNA.

### 4.1.2 Imaging cell actin structure with Lifeact-GFP

As the motility and morphology of cells are clearly affected by treatment with our cylinder compounds, work began to image the cell cytoskeleton, and particularly the protein actin. Actin is a globular protein found in all eukaryotic cells. It polymerises into a fibrous form, known as F-actin, which not only forms the thin filaments of muscle, but also the microfilaments that constitute part of the cell cytoskeleton. Previous work within the group has suggested that the cylinder may interfere with the F-actin structure of MDA-MB-231 cells [14]. Treatment of the cells with 50, 100 and 200 μM cylinder appeared to show 'ruffling' of the cells' actin filaments with increasing cylinder concentration, shown in Figure 4.13. This was visualised by the staining of actin using a commercially available dye - FITC-phalloidin. The phalloidin moiety is known to bind to branches of F-actin, whilst FITC acts as a fluorophore ($\lambda_{ex}$ = 496nm, $\lambda_{em}$ = 518nm). Phalloidin can also be combined with other fluorophores such as rhodamine ($\lambda_{ex}$ = 557nm, $\lambda_{em}$ = 577nm), making the imaging of the co-localisation of actin with other fluorophores (such as $[Ru_2L_3]^{4+}$) an attractive option.

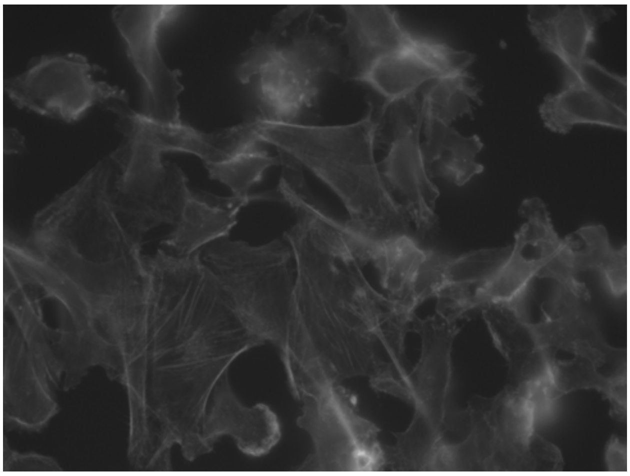

(a) Control image

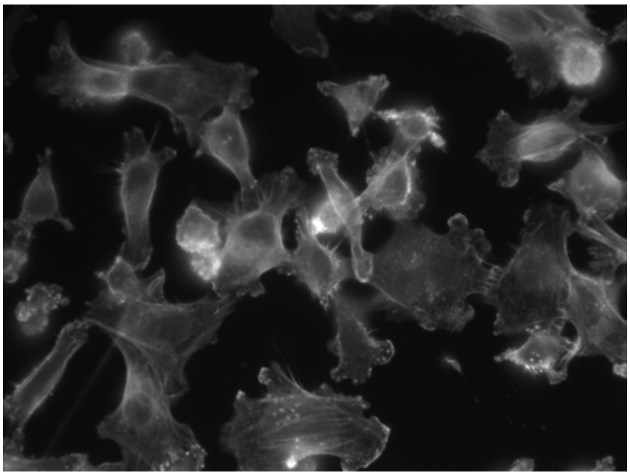

(b) Image following treatment with 200uM cylinder

**Figure 4.13:** Images of MDA-MB-231 cells stained with FITC-phalloidin; control image and image of cell treated with 200 μM parent cylinder [14]

Whilst staining with phalloidin is a very reliable way of imaging actin, the cellular membrane needs to be disrupted in order for the compound to be taken up, and therefore can only be performed on fixed cells. As we were hoping to study the effects of our cylinder over time, it was felt important to keep the membrane uncompromised to prevent unrealistic uptake of the cylinder. It was therefore decided to utilise the recently developed Lifeact marker [96]. This is a simple 17 amino acid peptide which is highly conserved in *Saccharomyces cerevisiae* yeast. Lifeact can be fused to green fluorescent protein (Lifeact-GFP) ($\lambda_{ex}$ = 488nm, $\lambda_{em}$ = 509nm) and introduced to cells as part of a vector plasmid which can be taken into cells without damaging the cell membrane. Lifeact-GFP has been shown to stain actin without interfering in cellular processes, and the considerable difference in emission maxima of GFP and our cylinder should allow for the co-localisation of the two fluorophores to be determined. Furthermore, as there is reported work showing that NAMI-A causes HeLa cells to contract and leave their lamellopodia actin-free [97], it would be interesting to see if the ruthenium cylinder had a similar effect.

In collaboration with Dr Steve Thomas (IBR, Birmingham), the Lifeact vector was expressed in *E. coli* bacteria cells and then isolated using a Sigma Aldrich Genelute Maxiprep Kit, ready to be introduced into our cells.

### 4.1.3 Fluorescence imaging of MDA-MD-231 actin structure

At the time of this work there were no literature reported example of Lifeact-GFP transfected MDA-MB-231 cells, however there was an several example of MBA-MB-231 cells transfected with Lifeact-mCh [98]; Lifeact fused to mCherry fluorescent protein, so this was used as the starting point for our transfection protocol. The experimental detail provided in this paper describes a simple transfection experiment, using commercially available cationic lipid transfection reagents. The use of all cationic lipid transfection reagents follow a very similar protocol where the DNA plasmid of interest is incubated in the transfection reagent and serum-free media. This allows the cationic lipid to interact with the phosphate backbone of the DNA, forming a DNA:liposome complex which can then be combined with serum containing media and used to treat cells. If the DNA:liposome complex has successfully formed, then it should be endocytosed into the cells where the liposome breaks down leading to release of the DNA plasmid into the cytoplasm where it can be expressed. The absence of serum in the first step is crucial to ensuring the formation of the DNA:liposome complex. Control images of MDA-MB-231 cells transfected with Lifeact-GFP, but not treated with ruthenium cylinder show that the cells have retained their characteristic ‘spindle-like’ morphology and are clearly expressing GFP, shown in Figure 4.14.

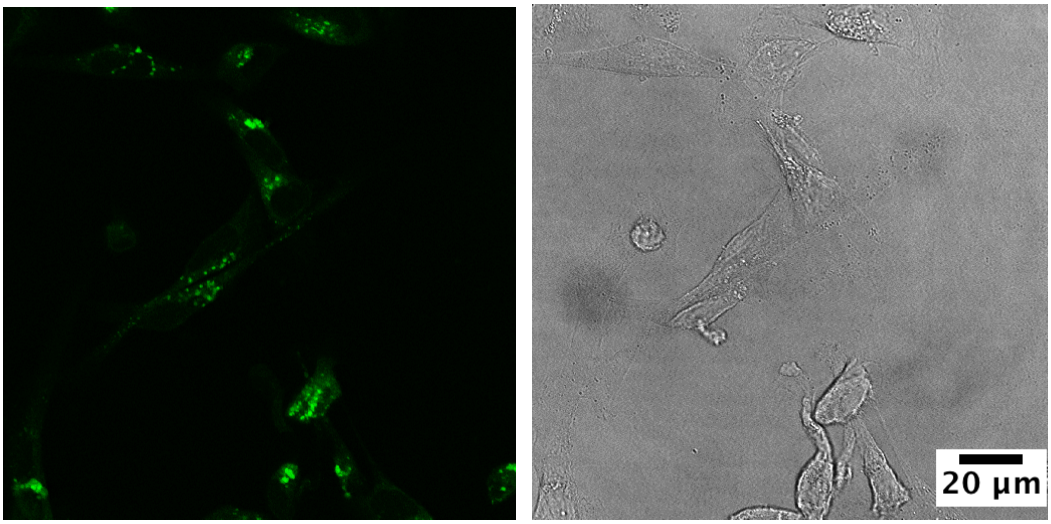

**Figure 4.14:** MDA-MB-231 cells transfected with Lifeact-GFP, brightfield image (left) and corresponding fluorescence image (right).

As the transfection appeared to have been successful,the cells were treated with varying concentrations of $[Ru_2L_3]^{4+}$ and imaged using fluorescence confocal microscopy. A control sample of cells treated with cytochalasin D, a compound known to depolymerise actin fibres, was also prepared. A change in morphology of the cells is observed with increasing $[Ru_2L_3]^{4+}$, as shown in Figure 4.15.

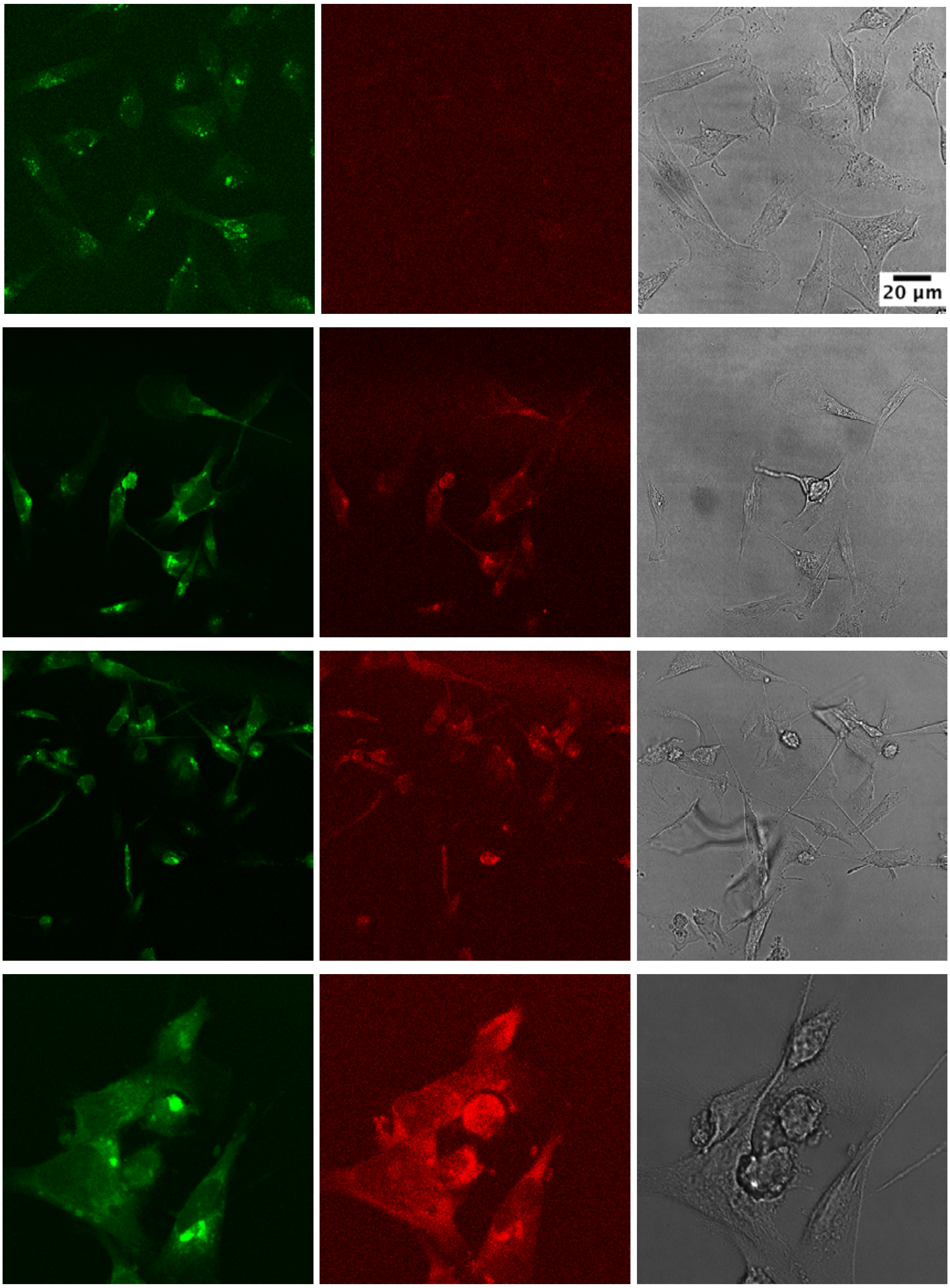

**Figure 4.15:** MDA-MB-231 cells transfected with Lifeact-GFP, and increasing concentrations of $[Ru_2L_3]^{4+}$. From left to right; fluorescence between 500-520nm, fluorescence between 680-720nm,and brightfield image. From top to bottom, concentration of $[Ru_2L_3]^{4+}$; control, 10 µM, 20 µM, 50 µM

By 50 μM concentration of $[Ru_2L_3]^{4+}$, the cells appear more spherical two cells in the centre of those images appear very similar in appearance to the cells treated with cytochalasin D, shown in Figure 4.16. As GFP is excited using the 488nm laser, fluorescence images in the 680-720nm range were also collected to observe any cylinder fluorescence. Again in the 50 μM sample, cylinder associated fluorescence can clearly be seen in all areas of the cell. It is however not seen in high intensity in the regions of high intensity GFP fluorescence suggesting the GFP and cylinder are not co-localised.

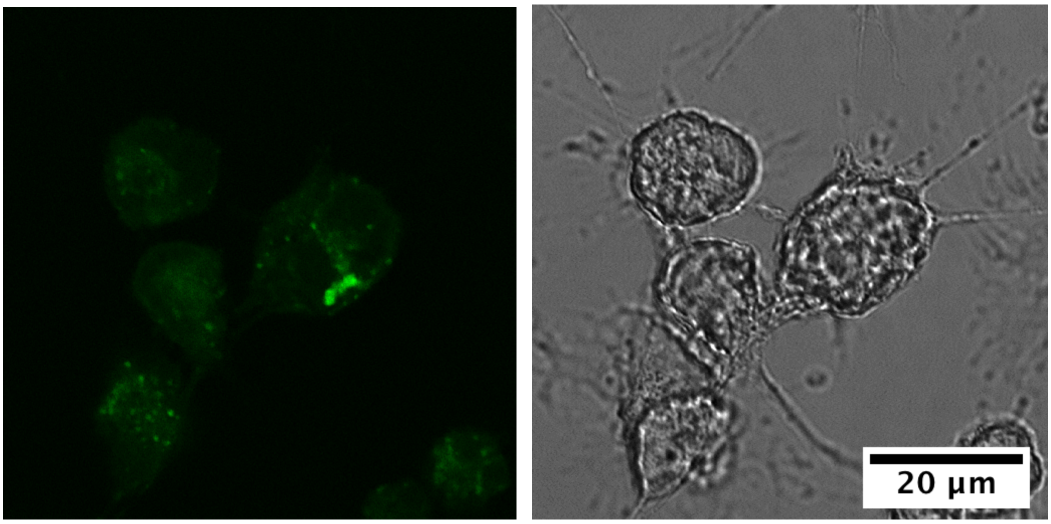

**Figure 4.16:** MDA-MB-231 cells transfected with Lifeact-GFP and then treated with cytochalasin D - fluorescence recorded between 500-520nm (left) and brightfield image (right).

Attempts to repeat the transfection were less successful, with possible precipitation of Lifeact-GFP observed around the nucleus. Modifications to the protocol centred on increasing DNA:liposome complex incubation time from 24 to 72 hours, and when this did not completely solve the problem, attention turned to maintaining a population of transfected cells, instead of repeating small scale transfections before each experiment. Cells survived comfortably for a week post transfection, applying normal cell cultures protocols. These changes improved the overall labelling, as structures such as the microtubule organisation centre (MTOC) and the leading edge of a moving cell can now be observed, and are shown in Figure 4.17. However, whilst the viability of the cells was not compromised, the number of cells expressing

Lifeact-GFP decreased, meaning the DNA plasmid was either being degraded, or was not being replicated during cell division, meaning the proportion of cells expressing the Lifeact-GFP will decrease by 50% with each cell replication cycle. Work therefore began on improving the transfection protocol, firstly by using antibiotic selection to preserve the stably transfected cells and secondly by investigating the technique of electroporation to deliver the plasmid directly to the nucleus, which may lead to more efficient expression of the plasmid.

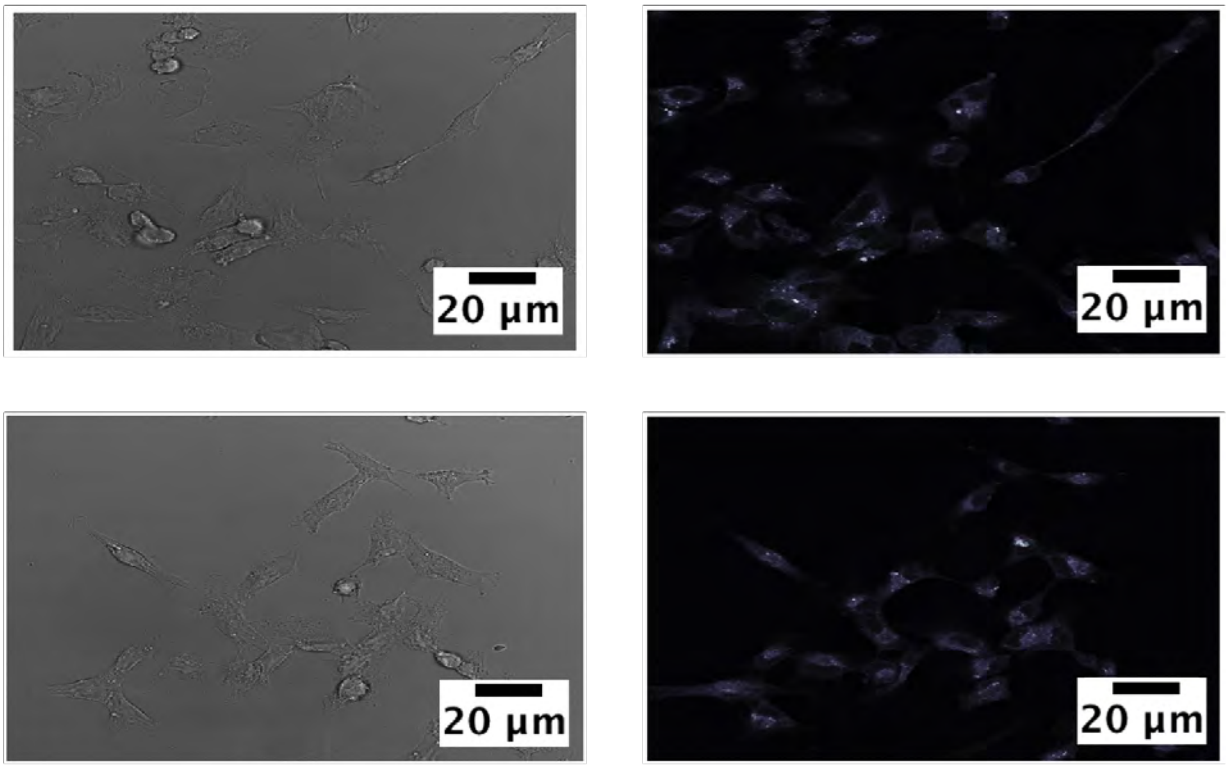

**Figure 4.17:** MDA-MB-231 cells transfected with Lifeact-GFP, brightfield and corresponding fluorescence images 5 (top) and 7 days (bottom) post-transfection.

Electroporation allows a plasmid to cross the cell membrane by increasing its permeability due to the application of an electrical field. This electrical field also temporarily disrupts the membrane of the nuclear envelope, meaning the plasmid can directly enter the nucleus. For the first attempts at nucleofection, a simple max-GFP plasmid was used in order to preserve Lifeact-GFP plasmid for future experiments. The electroporation was performed using an Axama Nucleofector (Lonza) using program X-013, which was recommended for the MDA-MB-231 cell line. However, initial experiments all resulted in immediate cell death. Attempts using different programs, different electroporation reagents and varying concentrations of cells and plasmid all also resulted in immediate cell death. At this point, it was decided to leave electroporation experiments and return to improving the transfection protcol, again using the maxGFP plasmid for initial studies. As well as repeating work with Turbofect, three other commercially available transfection reagents were trialled; X-tremeGENE 9 (Roche), TransIT 293 and TransIT LT-1 (both Mirus). Images were acquired 24 and 48 hours post-transfection, which showed that all four reagents had lead to some transfection of the plasmid, but the sample treated with Turbofect contained a much larger number of fluorescent cells so it was decided to continue work with this reagent. The images acquired at 24 and 48 hours are shown in Figure 4.18 and Figure 4.19 respectively.

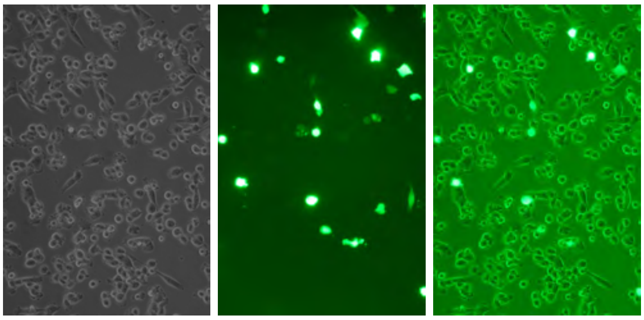

(a) Brightfield (b) Fluorescence (c) Overlay

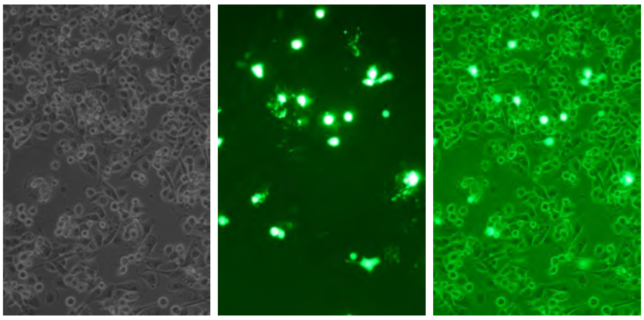

(d) Brightfield (e) Fluorescence (f) Overlay

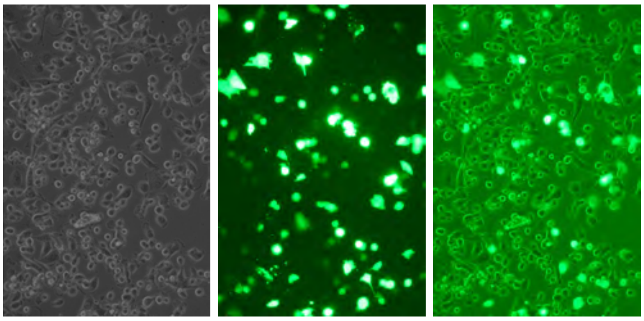

(g) Brightfield (h) Fluorescence (i) Overlay

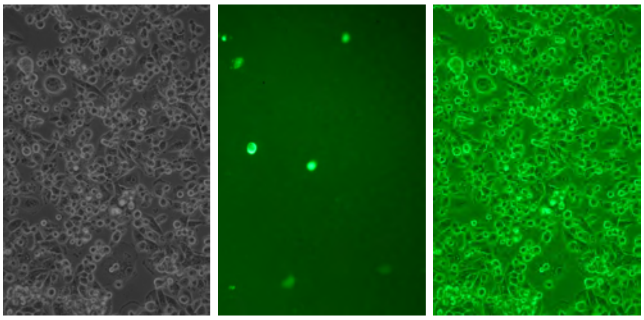

(j) Brightfield (k) Fluorescence (l) Overlay

**Figure 4.18:** MDA-MB-231 cells transfected with maxGFP, using a different transfection reagent for each row; TransIT293 (top), TransITLt1 (second row), Turbofect (third row), X-tremeGENE 9 (bottom). Each row shows brightfield image (left), fluorescence above 500nm following excitation at 488nm (middle), and the overlay of these images (right). All images recorded 24hrs post transfection. All images at 100x magnification.

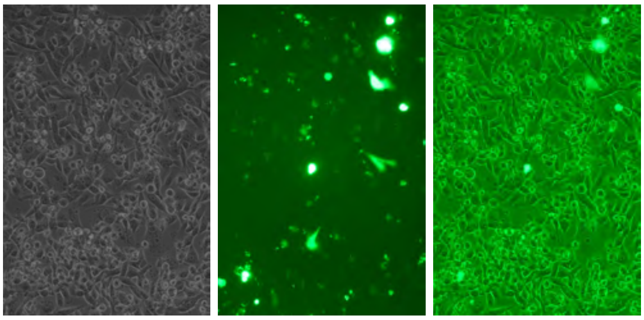

(a) Brightfield (b) Fluorescence (c) Overlay

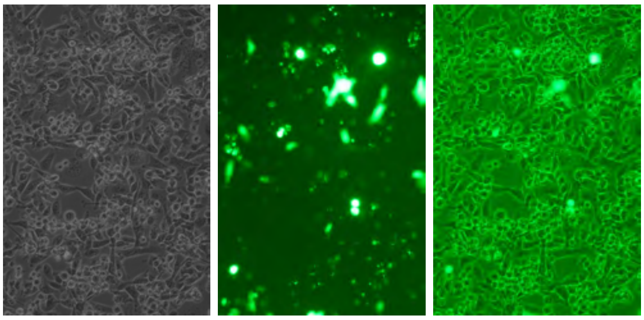

(d) Brightfield (e) Fluorescence (f) Overlay

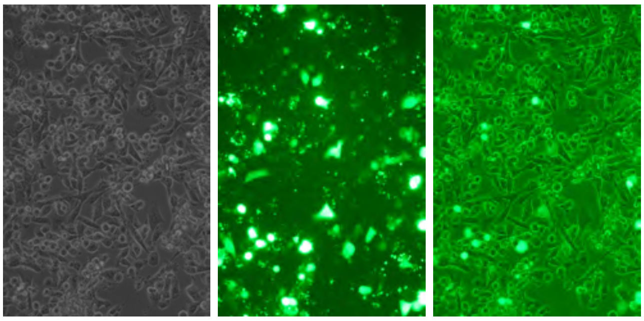

(g) Brightfield (h) Fluorescence (i) Overlay

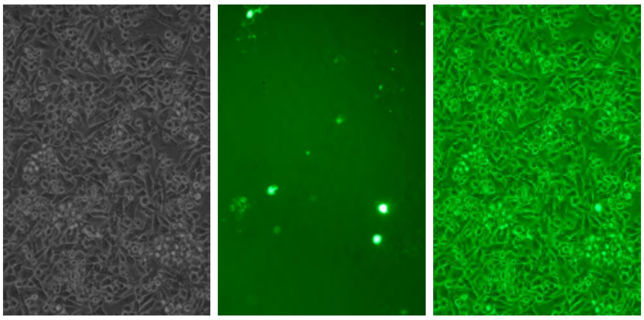

(j) Brightfield (k) Fluorescence (l) Overlay

**Figure 4.19:** MDA-MB-231 cells transfected with maxGFP, using a different transfection reagent for each row; TransIT293 (top), TransITLt1 (second row), Turbofect (third row), X-tremeGENE 9 (bottom). Each row shows brightfield image (left), fluorescence above 500nm following excitation at 488nm (middle), and the overlay of these images (right). All images recorded 48hrs post transfection. All images at 100x magnification.

A further transfection experiment was performed using Turbofect transfection reagent. After 48 hours, the cells were placed into a T25 flask and grown in media containing the antibiotic G418. The plasmid used to transfect the cells with Lifeact-GFP also contained the genetic code for G418 resistance, so growing cells in these conditions should allow only successfully transfected cells to survive leading to a large population of cells expressing Lifeact-GFP. Initially the media was dosed with a low concentration of G418, with the aim of increasing its concentration over 2-3 weeks. However, even at low doses, the antibiotic killed almost all the cells and those that did survive did not replicate (even when switched back into G418-free media), meaning the whole population died within 5-7 days. Repeated attempts at producing a stable population failed, so it was decided to revert to performing transfections on a small sample of cells as and when required. Since this work was performed, the first paper has been published with Lifeact-GFP transfected MDA-MB-231 cells [99]. This work describes the transient transfection of cells using a further transfection reagent - Lipofectamine 2000 (Invitrogen), which may be an avenue to investigate for future work.

To conclude this section of work, a final experiment was performed using MDA-MB-231 cells transiently transfected with Lifeact-GFP. The cells were treated with $[Fe_2L_3]^{4+}$ for two, four or six hours, fixed and imaged using fluorescence confocal microscopy. It is known that $[Fe_2L_3]^{4+}$ can quench the fluorescence of GFP [76], so if $[Fe_2L_3]^{4+}$ co-localises with the Lifeact-GFP, a decrease in fluorescence intensity should be observed with increasing treatment time.

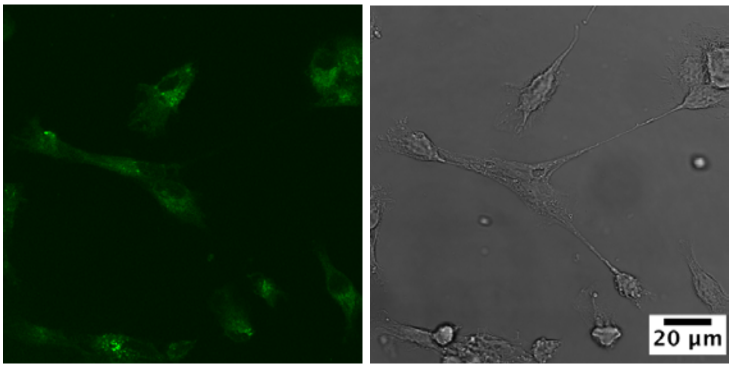

(a) control fluorescence (b) control brightfield

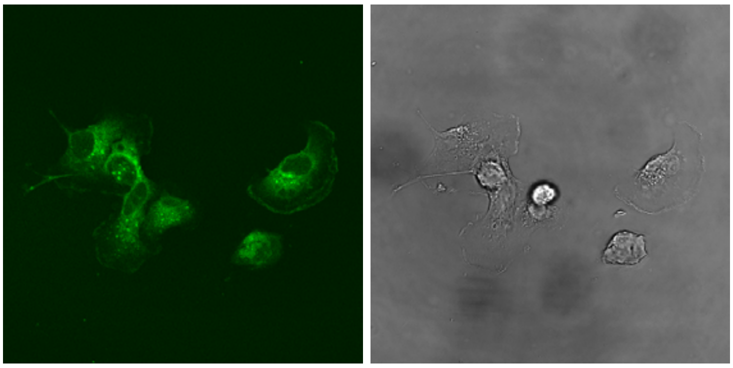

(c) 2hrs fluorescence (d) 2hrs brightfield

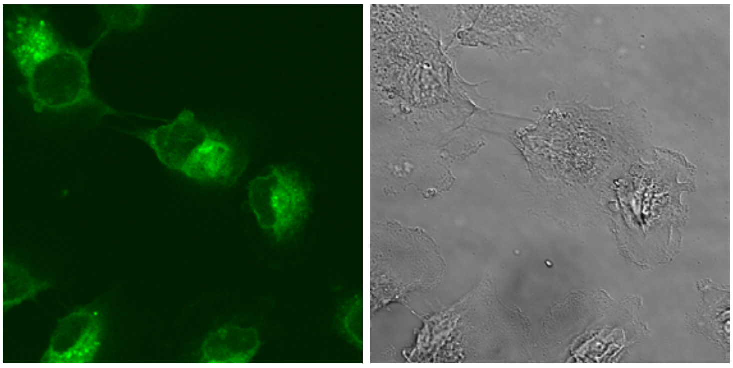

(e) 4hrs fluorescence (f) 4hrs brightfield

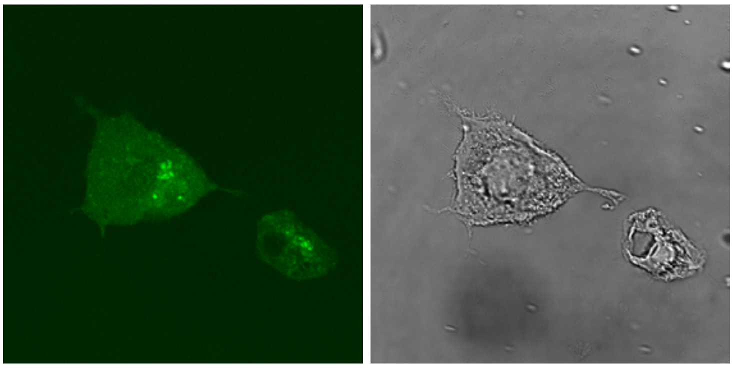

(g) 6hrs fluorescence (h) 6hrs brightfield

**Figure 4.20:** MDA-MB-231 cells transfected with Lifeact-GFP and treated with $[Fe_2L_3]^{4+}$ for two, four or six hours showing clear change in cell morphology.

After just two hours treatment, a change in the cell morphology is clear - the cells are no longer thin and spindle-like, they have spread out and show leading edges along their entire length, which is uncharacteristic for this cell line. By four hours the cells have continued to lose their characteristic morphology and more large leading edges are visible. Following six hours treatment, the cells are almost unrecognisable from the control images. The clear labelling of the actin structure at two and four hours treatment however suggests that the Lifeact-GFP is not being quenched by $[Fe_2L_3]^{4+}$ and, as believed with $[Ru_2L_3]^{4+}$, the cylinder does not directly bind to the actin subskeleton of MDA-MB-231 cells.

Following on from the phase contrast imaging shown in Figure 4.4, the one cylinder which did not cause any decrease in cell motility was $[Fe_2L^{Me}{}_3]^{4+}$. Therefore Lifeact-transfected MDA-MB-231 cells were treated with $[Fe_2L^{Me}{}_3]^{4+}$, and imaged as above. The images obtained are shown in Figure 4.21.

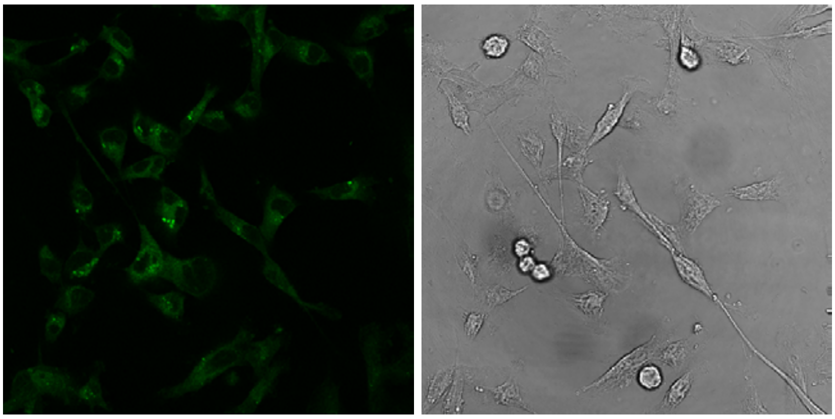

(a) 4hrs fluorescence (b) 4hrs brightfield

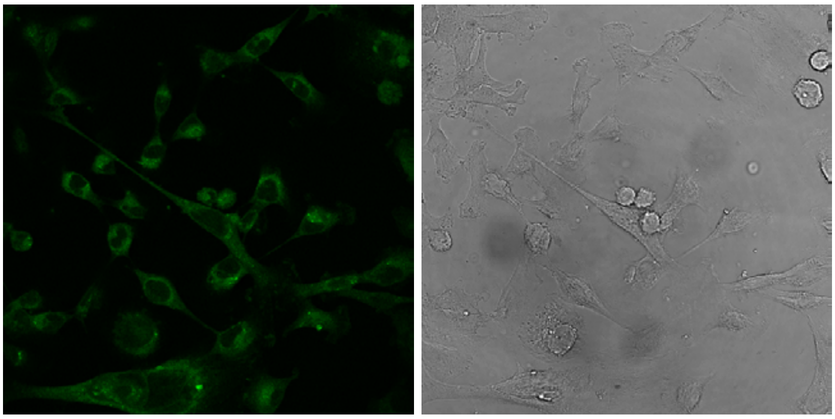

(c) 6hrs fluorescence (d) 6hrs brightfield

**Figure 4.21:** MDA-MB-231 cells transfected with Lifeact-GFP and treated with $[Fe_2L^{Me}{}_3]^{4+}$ for four or six hours showing no change in cell morphology following cellular treatment.

These images confirm that the structural integrity of the cells is maintained following treatment $[Fe_2L^{Me}{}_3]^{4+}$, which again suggest that there is no direct interaction between the cylinders and actin. The branched nature of actin means that there are many junctions of varying sizes that any compound could bind to. Whilst the methyl groups on $[Fe_2L^{Me}{}_3]^{4+}$ prevent its binding to the DNA Y-shaped junction, it seems unlikely that these groups could prevent binding to the larger junctions of the actin protein. As the only disruption to cellular structure and motility is seen when treated with compounds which are known to bind to DNA, it seems logical that it is caused by an interruption of the signalling cascade and not direct interaction between the cylinders and actin.

## 4.2 Investigating the production of gaseous species within MDA-MB-231 and SKOV-3 cells

As it is not believed that the decrease in cell motility observed following cell treatment is due to direct interaction with actin, attention was turned to investigating if cylinder treatment lead to the production of compounds which *are* known to disrupt the motility of cells. A literature review revealed some very interesting work describing the effect of nitric oxide (NO) on two of the cell lines investigated earlier in this chapter; MDA-MB-231 and LX-2 cells, and it is discussed in the following sections.

### 4.2.1 NO and its role in cell function

Nitric oxide is a small gaseous molecule intrinsic to cellular processing and signalling. As it is involved in so many processes, there is conflicting opinion in the literature as to whether NO could be used as part of cancer combination therapy, or if it leads to drug resistance [100] [101] [102]. It is produced within mammalian cell lines during the conversion of L-arginine to L-citrulline by three enzymes known as the NO synthase (NOS) family.

$$\mathrm{L{-}arginine} + \tfrac{3}{2}\,\mathrm{NADPH} + \mathrm{H}^+ + 2\,\mathrm{O}_2 \longrightarrow \mathrm{citrulline} + \mathrm{NO} + \tfrac{3}{2}\,\mathrm{NADP}^+$$

The three isoforms of NOS are traditionally named after the cell type in which there were first isolated [103]. nNOS was first isolated from neuronal tissue, but is predominantly found in skeletal tissue. iNOS was first found in macrophages and so was termed ‘inducible NOS’. The third isoform to be isolated, eNOS, was derived from endothelial cells but is found in platelets and the hippocampus. To further confuse matters, eNOS is additionally termed constitutive NOS (cNOS). To ease confusion, the NOS family are officially categorised as NOS1 (nNOS), NOS2 (iNOS) and NOS3 (eNOS and cNOS), and this terminology will be used from here onwards.

Looking specifically at MDA-MB-231 cells, it has previously been stated that these cells do not produce NO endogenously [104]. This statement was based on the work of Zeillinger *et al* who stated that DNA that codes for NOS3 was not detectable in MDA-MB-231 cells using cRT-PCR [105]. Subsequent papers by Pervin *et al* have repeated Zeillinger's findings and showed that neither NOS3 nor NOS2 are detectable by cRT-PCR [106]. This is however contradictory to the work of Mathews *et al* who used Western Blot experiments to show that MDA-MB-231 cells contain all three isoforms of NOS [107] and treatment with specific NOS3 inhibitor N-LIO increased cell motility[108], again suggesting that MDA-MB-231 cells do contain the NOS isoforms.

NO pro-drug NONO-AM has been shown to be toxic to MDA-MB-231 cells, with NO being released from the drug by esterase enzymes. Cell death correlated with increasing NO levels within cells [109]. Work by Lahiri and Martin investigated the effect of NO on the adhesion and motility of MDA-MB-231 cells [108]. This work again showed a 'two-sided' nature of NO. Low levels of NO (introduced into the cells by treating them with 5 mM L-arginine) were shown to decrease motility as determined by scratch-wound assay, but higher levels of NO decreased cell adhesion. The reported effects of NO upon on MDA-MB-231 cells are similar to the effects observed following cylinder treatment, suggesting that the changes in cell motility seen following cylinder treatment may be due to the production of NO.

### 4.2.2 Investigating the production of NO within cells

Whilst there are many reported probes for NO [110] [111] [112], they are almost all compromised by their non-specificity towards NO, and the fact they contain fluorescent groups such a fluoroscein. A recently published, and now commercially available probe however seems to overcome the disadvantages of the traditional NO probes [15]. This probe, $NO_{550}$, does not contain a diaminobenzene moiety, the electron rich and highly reactive group which reduced the specificity of previous NO probes. In the presence of NO and $O_2$, $NO_{550}$ enters a cascade reaction to form a diazo compound, $AZO_{550}$, the mechanism for which is shown in Figure 4.22. Upon excitation with 470nm light, $AZO_{550}$ has emission centred at 550nm. $NO_{550}$ shows no such emission following excitation at 470nm, and treatment of $NO_{550}$ with molecules such as

$H_2O_2$, $ONOO^-$ and DHA (all of which are known to interfere with currently used probes) does not lead to the formation of $AZO_{550}$, or any other fluorescent compound. This demonstrates the selectivity of $NO_{550}$, and combined with its pH stability and previous use in imaging endogenous NO [15], this made it an extremely attractive route for investigating NO production within the cell lines previously imaged.

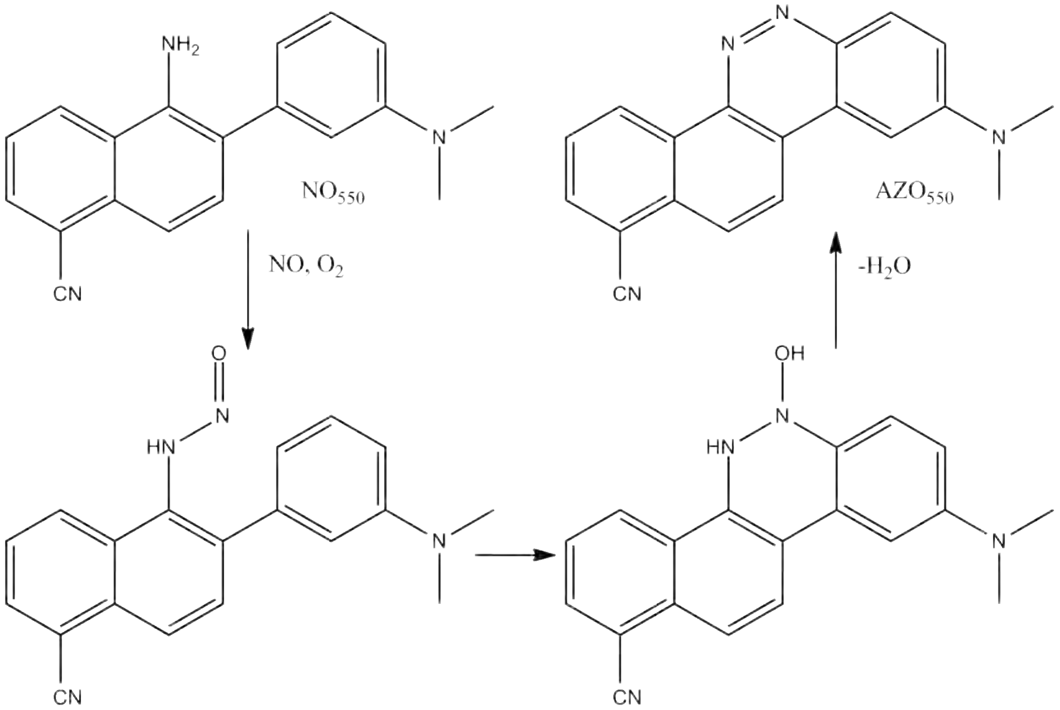

**Figure 4.22:** Mechanism of $AZO_{550}$ production from $NO_{550}$ [15]

The first step was to establish the toxicity of $NO_{550}$ towards MDA-MB-231 cells, so the MTT assay was used to determine an $IC_{50}$ for $NO_{550}$. The $NO_{550}$ shows poor solubility in media which may explain the large error values associated with each concentration value. A Student's T-test comparing the control samples and those treated at 100 μM using a p=0.05 significance, found that there was no significant difference between the two populations, so it was determined that $NO_{550}$ was not toxic to cells over 72 hours at the concentrations tested.

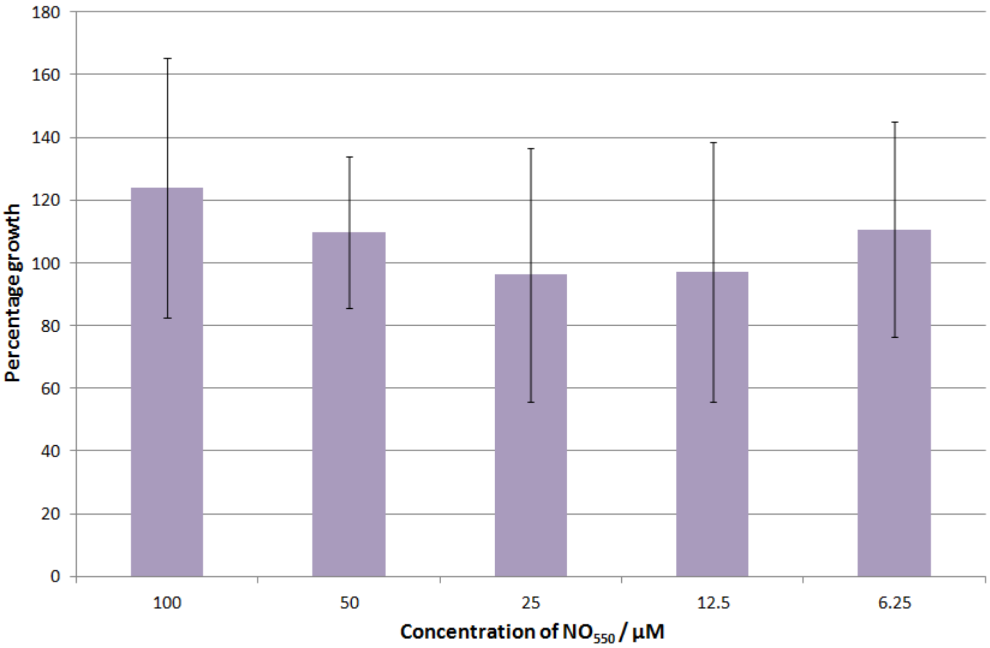

**Figure 4.23:** MTT data of $NO_{550}$ probe, showing that the probe is non-toxic to MDA-MB-231 cells. Plot shows mean and standard deviation (n=3) of triplicate experiments, each experiment was performed in quadruplicate. A Student's t-test was performed using p=0.05, which showed that there was no statistically significant difference in growth rates between populations treated with $NO_{550}$ probe, and those populations which were left untreated.

To investigate the effect of the iron cylinder on NO production within MDA-MB-231 cells, they were incubated with 100 µM of iron cylinder 4h, followed by a 20 minute incubation with 50 µM $NO_{550}$ probe. The cells were then fixed and mounted before being imaged using fluorescence confocal microscopy. Control samples of $NO_{550}$ probe alone and $FeCl_2$, parent ligand and $Ru(NO_3)_3NO$ with $NO_{550}$ were also prepared. The ruthenium nitrosyl sample was prepared as positive control as a source on NO, it was expected that cells treated with $NO_{550}$ followed by ruthenium nitrosyl would lead to the observation of an fluorescent signal within the cell. The images produced show that control sample of cells alone, when excited at 488nm show no autofluorescence in the 520-560nm region. The sample containing just $NO_{550}$ probe, shows low levels of fluorescence in the 520-560nm region, showing that MDA-MB-231 cells do contain low levels of endogenous NO. The sample treated with ruthenium nitrosyl shows large amounts of fluorescence showing that the probe does indeed work in cells with a source of NO.

Excitingly, the sample treated with $[Fe_2L_3]^{4+}$ also shows high levels of fluorescence - strongly suggesting that the parent cylinder induces the production of NO within MDA-MB-231 cells. As control samples containing just $FeCl_2$ or parent ligand resulted in low levels of fluorescence being observed, the effect observed following treatment with $[Fe_2L_3]^{4+}$ is not as a result of the cylinder being metabolised into starting materials either in media or within the cells. All images are shown in Figure 4.24.

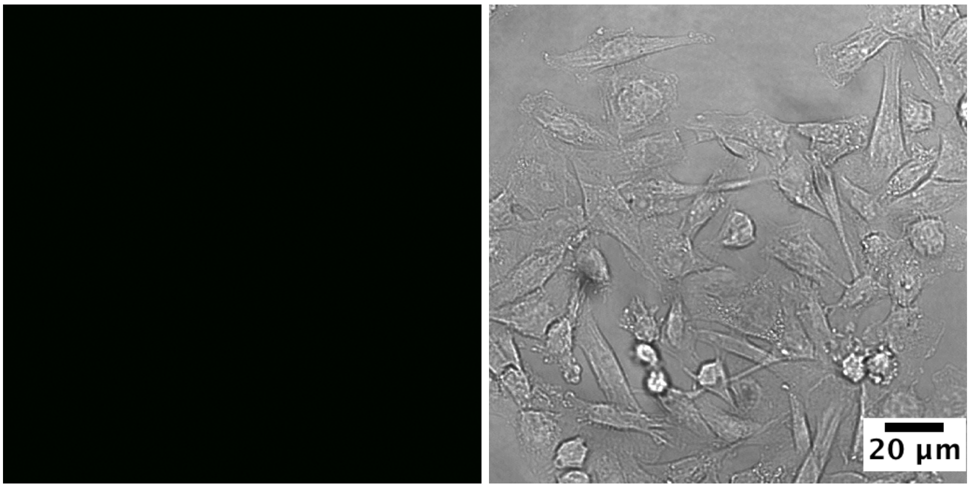

(a) control fluorescence (b) control brightfield

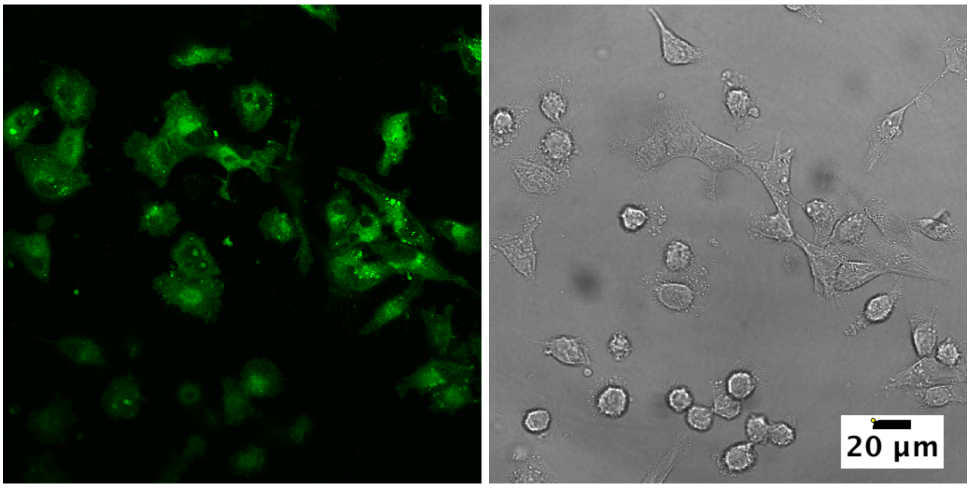

(c) $Ru(NO_3)_3NO$ fluorescence (d) $Ru(NO_3)_3NO$ brightfield

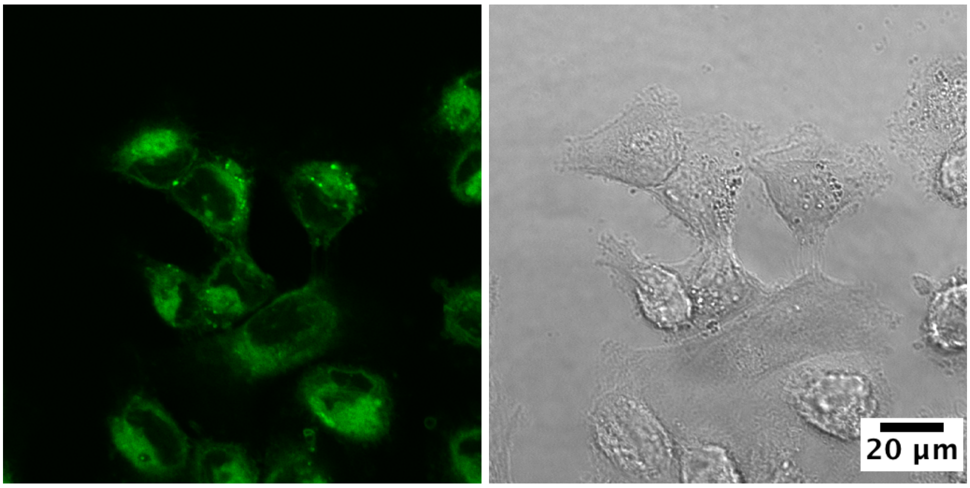

(e) $[Fe_2L_3]^{4+}$ fluorescence (f) $[Fe_2L_3]^{4+}$ brightfield

**Figure 4.24:** Fluorescence and brightfield images of MDA-MB-231 cells showing images of cells treated with; (a-b) no compounds (c-d) $Ru(NO_3)_3NO$ with $NO_{550}$ and (e-f) $[Fe_2L_3]^{4+}$ with $NO_{550}$.

The samples were re-imaged using an integrated microscope-spectrophotometer system to record images and emission spectra for each sample, to hopefully show the presence of an emission band between 520-560nm in samples we believe contain NO. This however proved unsuccessful, as no emission peak in the 520-560nm range could be observed. This was believed to be due to the $AZO_{550}$ photobleaching over the 8 minutes required to record each spectrum. Attention therefore turned to trying to quantify the amount of fluorescence produced by each compound. This was done by determining the mean pixel intensity for each image, using the same algorithm described in Section 3.3.1, and the resulting calculated average intensities are presented in Figure 4.25.

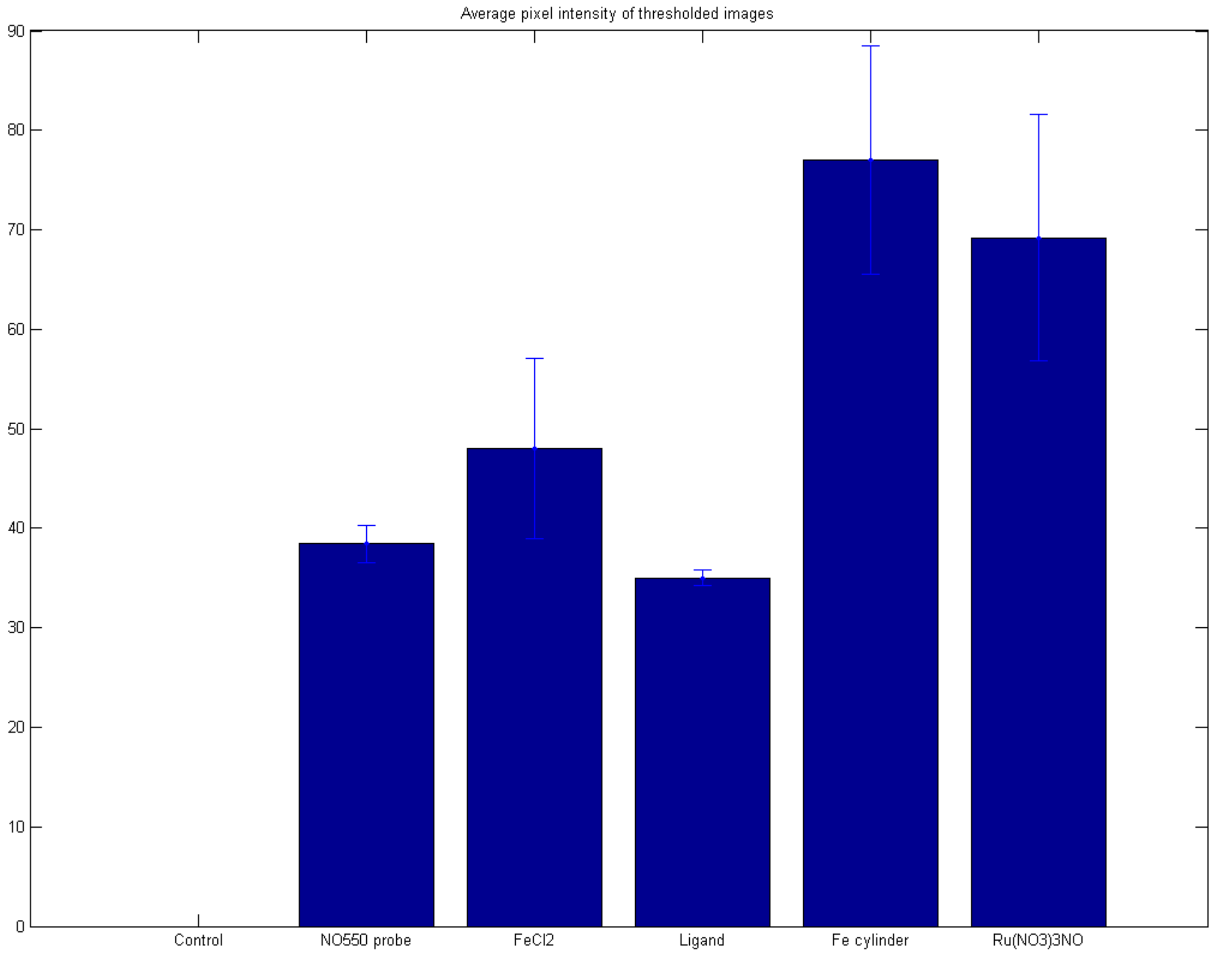

**Figure 4.25:** Intensities of thresholded images containing $NO_{550}$ probe, showing cells treated with $Ru(NO_3)_3NO$ or $[Fe_2L_3]^{4+}$ lead to significantly increased fluorescence signal compared to control samples. Mean pixel intensity shown with one standard deviation (n=3). A Student's t-test at p=0.05 showed that there is a statistically significant difference between the average fluorescence from samples treated with $Ru(NO_3)_3NO$ or $[Fe_2L_3]^{4+}$ compared to all other samples.

These intensities show that the levels of fluorescence seen in samples treated with Fe cylinder or $Ru(NO_3)_3NO$ are significantly higher than those seen in samples treated with ligand, $FeCl_2$ or $NO_{550}$ probe alone (as supported by use of Student's t-test) - strongly suggesting the presence of cylinder induces the production of NO within MDA-MB-231 cells.

Whilst these images are not conclusive that the production of NO is the cause for the change in cell motility, they do show an interesting property of the cylinder that was previously unknown and open up the potential for a entirely new line of work to fully determine the cylinder's mode of action. Repeating this work with $[Fe_2L^{Me}{}_3]^{4+}$, which did not appear to have any effect on cellular motility would allow for a more definitive conclusion to be drawn - if no NO is produced following treatment with $[Fe_2L^{Me}{}_3]^{4+}$, it could then be said that the NO is the cause of the decreased motility.

# Chapter 5

# Towards developing a MALDI imaging protocol for imaging cylinder within tissue

## 5.1 Mass Spectrometry and its application to imaging biological samples

Light microscopy has provided a solid technique for imaging the cylinders and their effects upon cells. However, it does not allow for any investigation into their metabolic fate; once metabolised the ruthenium cylinder loses its fluorescent properties and so can no longer be detected. There is therefore a need to complement the fluorescence microscopy studies presented here with a technique which provides chemical information about the metabolic fate of the ruthenium cylinder, such as mass spectrometry (MS). Fluorescence microscopy studies presented in Section 3.2.1 can show the fate of ruthenium cylinder where the $Ru{-}N_6$ chromophore remains intact, but would not show the localisation of any ruthenium not bound within the cylinder. The XRF studies presented in Section 3.4.4 can show the localisation of elements within a cell, but it cannot be used to determine which compound those elements are found in. By using MS, it is possible to obtain chemical information that can then be used to identify the coumpounds present. The basic events of MS are ionisation of the sample, separation of these ions on the basis of their mass to charge (*m/z*) ratio, and then the detection of these ions. A final spectrum is produced displaying the number of ions of each *m/z* ratio and it is then for the user to determine which chemical species each *m/z* ratio corresponds to. MS has been shown to be applicable in a significant range of sample material, from small molecular weight molecules through to large peptides and proteins, determining parameters as varied as elemental composition through to the detection of lipids in brain tissue samples. This is only possible due to the development of a wide range of ionisation techniques.

The ultimate hard ionisation technique is Inductively Coupled Plasma MS (ICP-MS). The sample is introduced to an argon plasma as an aerosol produced by either laser ablation of a solid sample or by passing a liquid sample through a pneumatic nebuliser. The sample is then vaporised, atomised and ionised. In this extreme environment, only elemental ions will be formed - no intact molecules of the initial sample will remain. This means that whilst the elemental composition of the sample can be determined, no information can be gathered about the sample's chemical composition. The energy within the plasma is around 15.8eV (the first ionisation energy of argon) which allows for ionisation of nearly all the elements of the periodic table as the majority of elements ionise between 4-12eV. The potential for multi-element detection with sensitivity in the parts per billion (ppb) range (depending upon the element) makes ICP-MS one of the most utilised trace element detection techniques. A recent study showed that LA-ICP-MS was a complementary technique to MRI imaging with improved sensitivity and access to information about the fate of carboplatin within pig brain [113].

Secondary Ion Mass Spectrometry (SIMS) also allows for the elemental composition of a sample to be determined, but does not use a laser to ionise the sample. An ion gun within the instrument produces a beam of positive (normally $Cs^+$) or negative (normally $O^{2-}$) ions which are termed the 'primary ions'. These ions are focused onto the sample leading to the sputtering of sample ions which are then termed as the 'secondary ions' which give this technique its name. This ionisation method is not as efficient as ICP-MS, as for every one charged species produced, there are 10,000 neutral species released from the sample which cannot be detected by MS, and there are also issues surrounding sample preparation which can include the need to sputter coat the sample with gold to improve the conductivity of the surface. Whilst these issues are clearly disadvantages with SIMS, the technique has found applicability in analysing small molecules following the development polyatomic primary ion beams such as gold clusters [114] or buckminsterfullerene ions [115].

The technique of SIMS only allows for ionisation of small molecules, larger molecules such as peptides and proteins will fragment under these conditions. Nobel Prize winning chemistry carried out in parallel by two separate research groups led to the development of Matrix Assisted Laser Desorption Ionisation MS (MALDI-MS) [116] [117]. By co-crystallising the sample with a large molar excess of a matrix, the sample is protected from the full force of a laser, resulting in predominantly singularly charged intact sample ions. This technique has been shown to be applicable to samples as large as 1 million Da. As a second material is being introduced to the sample to be analysed, it is imperative that the matrix chosen does not alter the composition of the sample. Matrices are generally small organic molecules which must be chosen to efficiently absorb the light emitted by the instrument laser. As the most commonly used lasers are nitrogen lasers emitting at 337nm, four of the most commonly used matrices - $\alpha$CHCA, THAP, DHB and SPA (shown in Figure 5.1) - are compounds which all readily absorb UV light. The choice of matrix, as well as the method of matrix application (by techniques such as airbrushing, electrospray or acoustic droplet spotting) is not governed by a well-defined set of rules - the events involved in the co-crystallisation of sample and matrix are not wholly understood and so the optimum sample preparation protocol must be determined for each new sample.

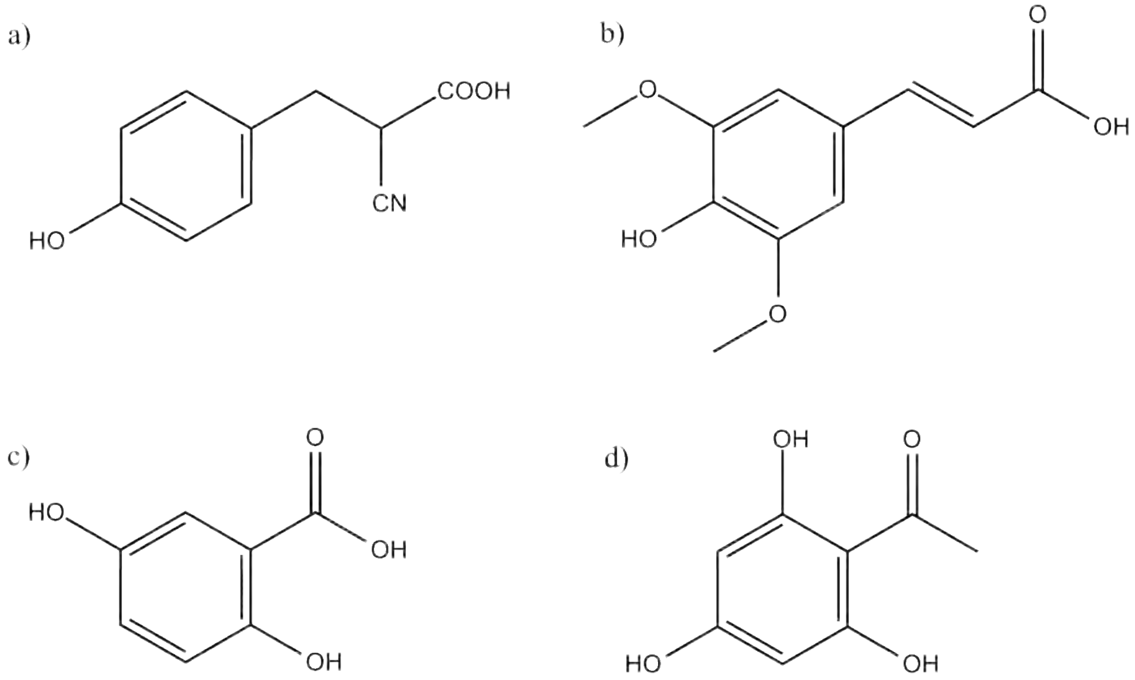

**Figure 5.1:** Structures of four commonly used matrices in MALDI-MS; a) a-hydroxy-4-cinamic acid ($\alpha$CHCA), b) sinapinic acid (SPA), c) 2,5-dihydroxy-benzoic acid (DHB) and d) 2',4',6'-trihydroxy-acetophenone (THAP).

LA-ICP-MS, SIMS and MALDI-MS all allow for imaging of their samples. This is achieved by recording mass spectra at thousands of discrete locations within the sample and then using these to produce images showing the ion counts of the desired *m/z* ratio at each location, in much the same way as elemental maps are produced using XRF as previously discussed in 3.4.1. A schematic of MS imaging is shown in Figure 5.2.

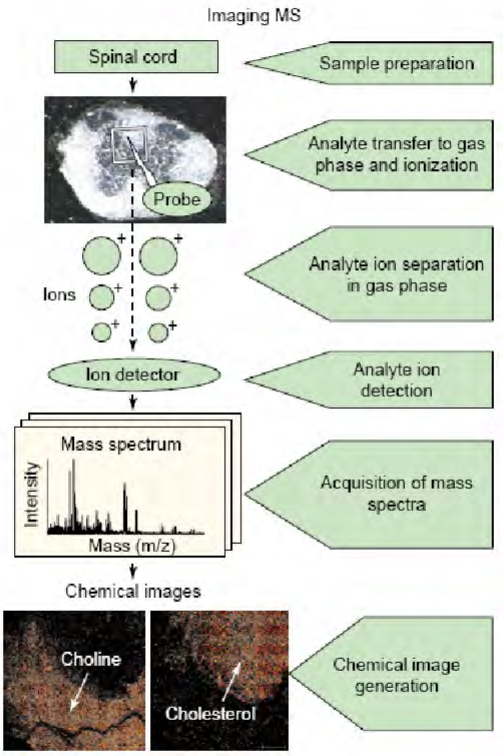

**Figure 5.2:** Schematic of MS imaging showing how multiple *m/z* values of interest can be imaged within one sample and one acquisition experiment. Image reproduced with permission from Figure 1 in [16].

As MALDI-MS has the ability to ionise molecules as large as proteins, any experiment searching for drug molecules in tissue are complicated by the presence of huge amounts of background material as well as matrix associated peaks. Early work on using MALDI-MS to analyse drug in tissue samples highlighted the importance of being able to conduct MS/MS experiments, where an *m/z* ratio of interest can be isolated within an ion trap and subjected to a second MS experiment. This second experiment is used to fragment this species and use the resulting spectrum to conclusively identify the species as either being drug or naturally occurring within the tissue. The Caprioli group have pioneered the use of MALDI-MS for imaging biological samples [118] and presented images of drug distribution (shown in Figures 5.3(a) and 5.3(b)) in tissue as far back as 2001 [17], and more recent work within other groups has shown that the images produced by MALDI-MS are comparable with those produced by autoradiography studies [18], a current standard procedure in the pharmaceutical industry.

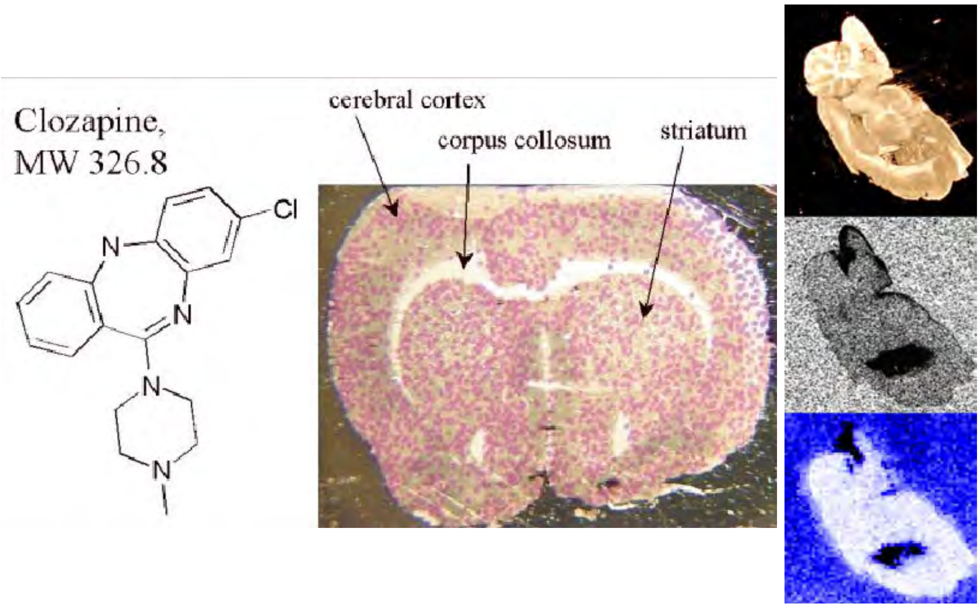

**Figure 5.3:** Left - Superimposed image of optical image of rat cortex and ion density map of clozapine (an anti-psychotic medication) obtained from the same sample. Image reproduced with permission from Figure 4 in [17]. Right - Top; optical image, Middle; autoradiography image and Bottom; MALDI-MS/MS image of clozapine in rat brain. The MALDI MS image shows good correlation with the autoradiogrphy image. Image reproduced with permission from Figure 6 in [18].

Mass Spectrometry has enormous applicability for imaging drug candidates within tissues and offers the significant advantage over current procedures (such as autoradiography) that the metabolic fate of the compound can be studied. It is hoped that these techniques will be applicable to studying our cylinders within cells and tissues. As ruthenium is not naturally found within cells, it allows all MS imaging techniques described to be utilised - LA-ICP-MS can detect ruthenium within tissue, SIMS could be used to image at sub-cellular level and MALDI-MS could be used to detect intact molecule and metabolites within tissue samples.

## 5.2 Studies with cylinder on steel plates

Initial work with mass spectrometry of $[Ru_2L_3]^{4+}$ began with studies into determining how suitable the cylinder is for such analysis. We must be able to observe *m/z* peaks that clearly correspond to cylinder ions or fragments (with good ion counts). Ideally we would also like to be able to select an *m/z* peak we believe is a cylinder ion and subject that to an MS/MS experiment and fragment it to produce a 'fingerprint' spectrum which could then be used to confirm the presence of cylinder within a given sample.

A 4ug/mL methanol solution of cylinder was combined in a 1:1 ratio with a 10mg/mL $\alpha$-CHCA matrix and spotted onto steel plates. Peaks corresponding to $[Ru_2L_3]^+$, $[Ru_2L_3]^{2+}$ and $[Ru_2L_3]^{3+}$ were observed but $[Ru_2L_3]^{4+}$ could not be seen. The most abundant peak occurred at 1331.98 ($[Ru_2L_3]^+$) and so this was subjected to MS/MS analysis under standard instrument conditions. However no fragmentation of this peak was achieved - only intact $[Ru_2L_3]^+$ associated peaks were observed in the MS/MS spectrum. This was not entirely unexpected as the cylinder is a very stable structure, and the cylinder was already known to remain as an intact molecule after ESI-MS analysis. However, without the ability to fragment the cylinder we almost certainly would not be able to identify the cylinder in any tissue sample.

It was decided to repeat the experiment using 3 different matrices - DHB, SPA and THAP, however all of these produced very poor results with very little ionisation of the cylinder observed so it was decided to revert back to $\alpha$-CHCA matrix. Work focused on optimising the parameters of the collision induced dissociation stage to hopefully achieve fragmentation of cylinder. By increasing the collision energy within the chamber during an MS/MS experiment to the instrument's maximum capability, peaks centred around *m/z* = 955.89 were observed which corresponds to $[Ru_2L_2]^{2+}$ and which also showed the correct isotope pattern for this compound. However the ion count for this species was less than 10, meaning it would be entirely lost within the background of a tissue sample. There were also another set of peaks centred at *m/z* = 1251.94 corresponding to another fragment of drug, as identified by its ruthenium isotope pattern, but again the most abundant peaks were un-fragmented $[Ru_2L_3]^+$. Continued alteration of instrument parameters ultimately showed that the peaks centred around *m/z* = 1251 correspond to the most abundant fragment, but again a maximum ion count of 10 was achieved which is too low to be useful in any tissue experiment. MS/MS spectra of the $[Ru_2L_3]^+$ ion are shown in Figure 5.4(a) and 5.4(b).

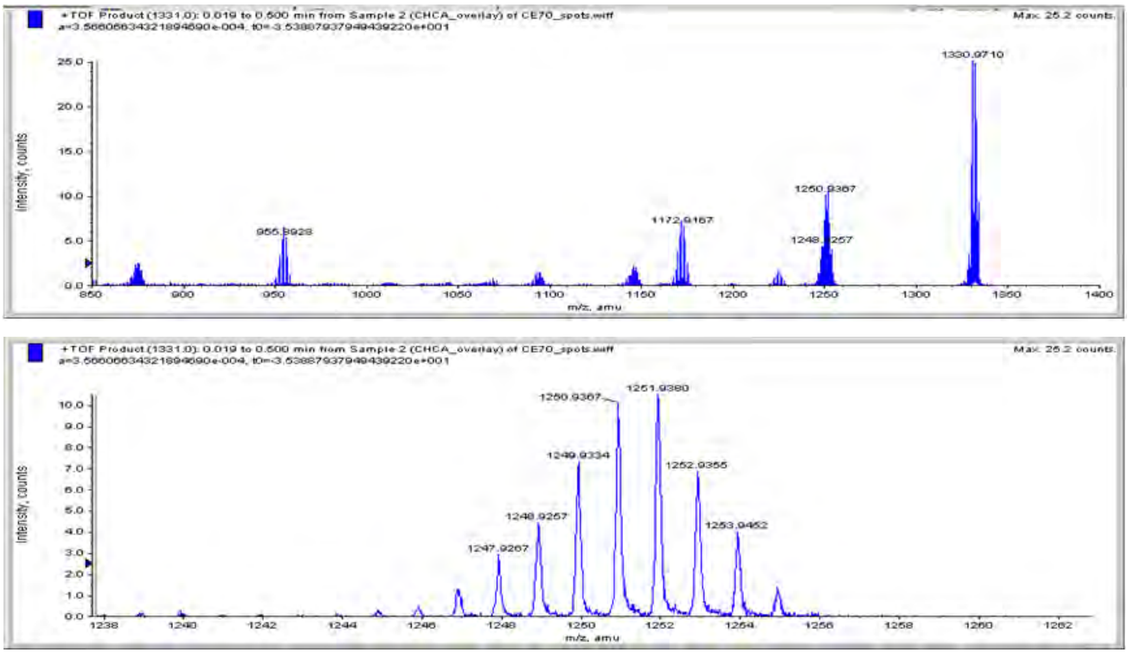

**Figure 5.4:** Above, MS/MS spectra of $[Ru_2L_3]^+$ (*m/z* = 1331.0) ion produced using $\alpha$-CHCA matrix. Below, expansion of *m/z* = 1240 to 1260 showing the correct isotope pattern for a dinuclear ruthenium compound.

Attention was therefore turned to using a technique which has recently been investigated within our group - the doping of the matrix with metal ions not normally found within the system [119]. The ionisation event within the instrument normally involves protonation of the molecular ion when the sample is a relatively straight forward system of compound in matrix spotted onto a steel plate. However, when the sample is a tissue-based system, the ionisation event normally involves cationisation usually by sodium or potassium. The formation of these metal-analyte adducts can massively complicate a spectrum; particularly if the analyte can form adducts with both sodium and potassium. By doping the matrix with metals such as lithium, caesium or silver, the sodium and potassium adducts are suppressed resulting in much cleaner spectra due to only one major metal-analyte adduct being formed. As $[Ru_2L_3]^{4+}$ doesn't fragment easily, using the doped matrix allows for the possibility of observing a metal-cylinder adduct and attempting fragmentation of that; i.e. instead of looking for fragments of the cylinder, look for the intact cylinder as a fragment of a larger adduct. With its distinctive isotope pattern, the cylinder should be relatively easy to identify provided it is seen in high enough ion counts.

Lithium and silver chloride doped samples of $\alpha$-CHCA were prepared, combined with cylinder and spotted onto steel plates. Analysis of silver doped samples revealed very little ionisation of the cylinder - by far the most abundant peaks observed were silver adducts of $\alpha$-CHCA. The lithium doped samples were much more promising - whilst no lithium-cylinder adduct was observed the mere presence of the lithium chloride was shown to increase ion counts of $[Ru_2L_3]^+$. This leads to more ions entering the collision chamber, and so increased ion counts of all the fragments - a maximum of 25 for *m/z* = 1251. Whilst this is still low, a two-fold increase in ion count was observed with a first attempt at matrix doping. It is hoped that the ion count can be improved further by optimising lithium concentration. MS/MS spectra of the $[Ru_2L_3]^+$ ion recorded in lithium-doped matrix are shown in Figure 5.5(a) and 5.5(b).

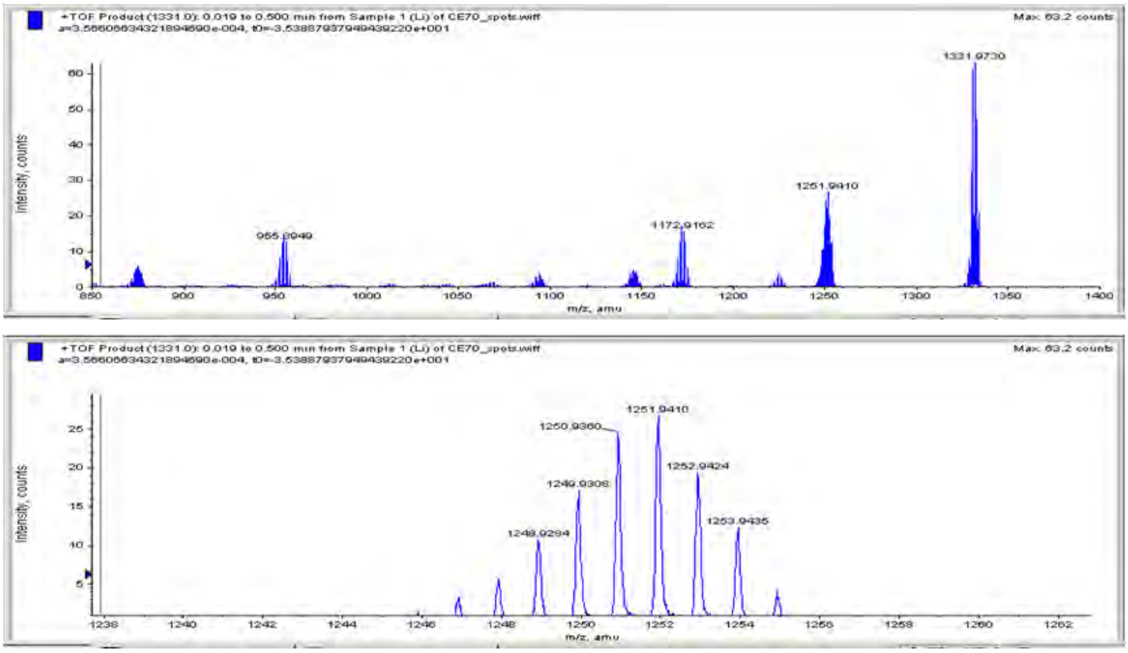

**Figure 5.5:** Above, MS/MS spectra of $[Ru_2L_3]^+$ (*m/z* = 1331.0) ion produced using lithium-doped $\alpha$-CHCA matrix. Below, expansion of *m/z* = 1240 to 1260 showing the correct isotope pattern for a dinuclear ruthenium compound.

Repetition of this experiment gave similar results, but it was qualitatively observed that the spots of lithium-doped samples were much less uniform on the steel plates compared to non-doped samples, and were more difficult to ablate. This very much represents ongoing work to determine optimum lithium concentration and instrument parameters for fragmentation of ruthenium cylinder, but it has been shown that the cylinder can be successfully ionised and fragmented using MALDI mass spectrometry. To take this work forward, experiments on doped tissue homogenates should be performed to determine the concentration of ruthenium needed within a tissue to be observable above the background of the tissue spectrum.

MALDI mass spectrometry therefore offers the opportunity to image and discover the metabolic fate of cylinders within an animal, which is the next stage for the cylinders if they are to become a genuine cancer therapeutic.

# Chapter 6

# Experimental

## 6.1 Ligand synthesis

### 6.1.1 Synthesis of ligand L - $C_{25}H_{20}N_4$

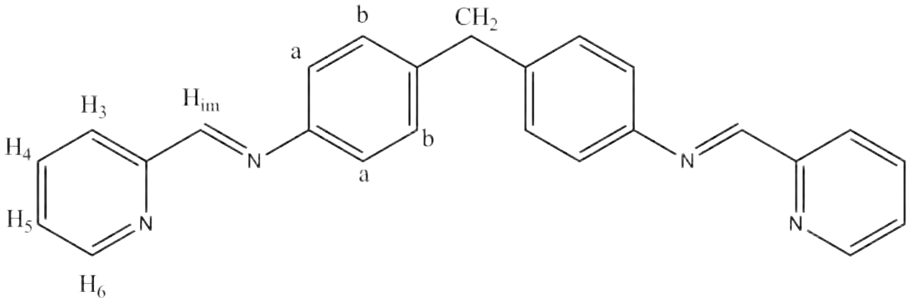

2-pyridine carboxaldehyde (1.4mL, 15.1mmol) and 4,4'-methylenedianiline (1.5g, 7.6mmol) were combined in 100mL ethanol and left to stir at room temperature overnight. The resulting pale yellow precipitate was filtered, washed with ethanol and dried *in vacuo*. Yield = 2.09g (73%)

$^1$H NMR (300MHz, $CDCl_3$, 298K): $\delta$ = 9.21 (2H, s, $H_{im}$), 8.75 (2H, d, J=7.0Hz, $H_3$), 8.51 (2H, d, J=4.2Hz, $H_6$), 7.83 (2H, td, J=8.3, 1.9, 0.6Hz, $H_4$), 7.39 (2H, ddd, J=7.6, 4.9, 1.2Hz, $H_5$), 7.29 (8H, m, $H_{a/b}$), 4.07(2H, s, $H_{CH2}$).

ESI-MS: *m/z* = 775.7 $[2L+Na]^+$

### 6.1.2 Synthesis of ligand $L^{Me}$ - $C_{27}H_{24}N_4$

*The synthesis of $L^{Me}$ was first described in Ref [120], but is included here with this author's characterisation*

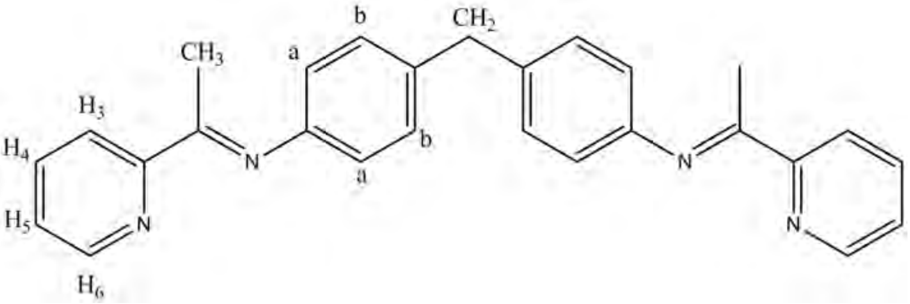

4,4'-methylenedianiline (630mg, 3mmol) was added to 10g of 3*Å* dry molecular sieves in 100mL of toluene and left to stir until all 4,4'-methylenedianiline had dissolved. 2-acetylpyridine (0.71ml, 2mmol) was added and the solution was allowed to stir for three days. The resulting mixture was filtered to remove molecular sieves and the filtrate reduced in volume under vacuum to give a dark yellow oil.

Yield = 0.96g (74%)

$^1$H NMR (300MHz, $CDCl_3$, 298K): $\delta$ = 8.70 (2H, d, J=4.0Hz, $H_6$), 8.05 (2H, d, J=8.0Hz, $H_3$), 7.98 (2H, td, J=7.5, 1.5Hz, $H_4$), 7.45 (2H, dd, J=7.6, 1.2Hz, $H_5$), 6.90 (4H, d, J=8.3Hz $H_{a/b}$), 6.70 (4H, d, J=8.3Hz $H_{a/b}$) 3.80 (2H, s, $H_{CH2}$) 2.80 (6H, s, $CH_3$).

ESI-MS: *m/z* = 405 [$L^{Me}$+H]

### 6.1.3 Synthesis of ligand $L^O$ - $C_{24}H_{18}N_4O$

*The synthesis of $L^O$ was first described in Ref [95], but is included here with this author's characterisation.*

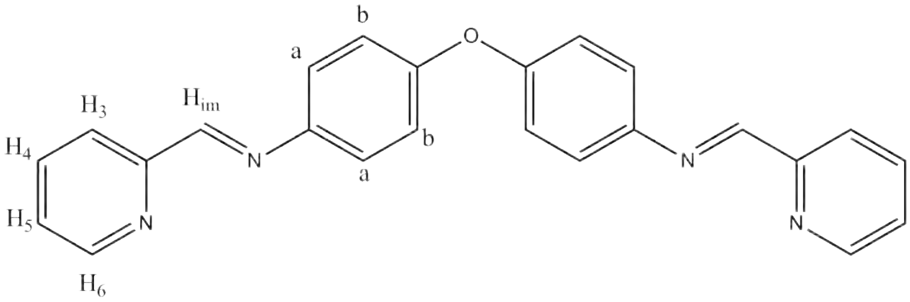

4,4’-diaminophenylether (1.00 g, 5 mmol) was dissolved in MeOH (10 mL) before a solution of 2-pyridinecarboxaldehyde (1.2 g, 11 mmol) in MeOH (15 mL) was added and the mixture was refluxed for 2 h. The solution was evaporated until precipitation occurred.

Yield: 1.10g (88%)

$^1$H NMR (300 MHz, $CDCl_3$, 298K): $\delta$ = 8.70 (2H, d, J=5.0 Hz, $H_6$), 8.65 (2H, s, $H_{im}$), 8.20 (2H, d, J=8.1 Hz, $H_3$), 7.80 (2H, t, J=7.9 Hz, $H_4$), 7.35 (6H, m, $H_5$, $H_{a/b}$), 7.10 (4H, d, J=8.7 Hz, $H_{a/b}$).

ESI-MS: *m/z* = 379 [L+H]

### 6.1.4 Synthesis of ligand $L^S$ - $C_{24}H_{18}N_4S$

*The synthesis of $L^S$ was first described in Ref [95], but is included here with this author’s characterisation.*

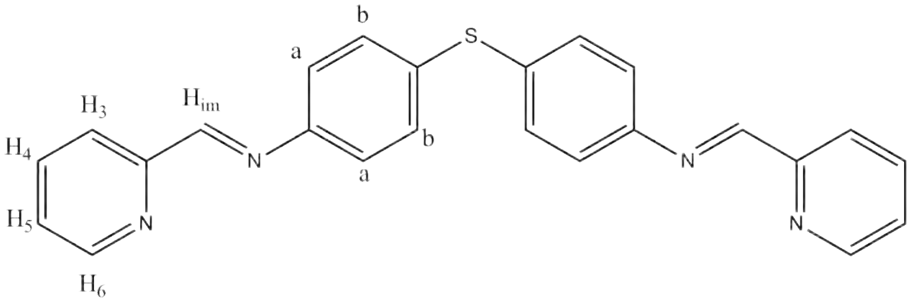

4,4’-thiodianiline (976.1mg g, 4.5 mmol) was dissolved in MeOH (10 mL) before a solution of 2-pyridinecarboxaldehyde (1.07 g, 10 mmol) in MeOH (5 mL) was added and the mixture was refluxed for 2 h. The solution was cooled, filtered and evaporated until a dark yellow/green oil was obtained. Addition of dichloromethane gave a solid which was filtered and dried *in vacuo*. Yield: 0.7191g (41%)

$^1$H NMR (300 MHz, $CDCl_3$, 298K): $\delta$ = 8.60 (2H, d, J=4.5 Hz, $H_6$), 8.45 (2H, s, $H_{im}$), 8.05 (2H, d, J=8.0 Hz, $H_3$), 7.68 (2H, t, J=6.3 Hz, $H_4$), 7.25 (4H, m, $H_{a/b}$), 7.12 (6H, m, $H_5$, $H_{a/b}$).

ESI-MS: *m/z* = 395 [L+H]

## 6.2 Fe-cylinder synthesis

### 6.2.1 Synthesis of $[Fe_2L_3]Cl_4$

Ligand L (0.0301 g, 0.08 mmol) and iron(II) chloride (0.0106 g, 0.05 mmol) were heated under reflux in MeOH (20mL) for 2 hr. The resulting purple-colored solution was cooled and treated with saturated methanolic ammonium hexafluorophosphate. On cooling, a purple precipitate ($[Fe_2L_3](PF_6)_4$) separated and was isolated by filtration (0.0408 g, 84%). Anion exchange to $[Fe_2L_3]Cl_4$ was carried out using tetrabutylammonium chloride.

$^1$H NMR (300 MHz, MeOD, 298K): $\delta$ = 9.20 (2H, s, $H_{im}$), 8.75 (2H, d, J=7.0 Hz, $H_3$), 8.50 (2H, t, J=6.5 Hz, $H_4$), 7.90 (2H, t, J=6.0 Hz, $H_5$), 7.50 (2H, d, J=4.0 Hz, $H_6$), 7.10 (4H, s, $H_{a/b}$), 5.60 (4H, s, $H_{a/b}$), 4.10 (2H, s, $CH_2$).

ESI-MS: *m/z* 310 $[Fe_2L_3]^{4+}$

### 6.2.2 Synthesis of $[Fe_2L^{Me}{}_3]Cl_4$

*The synthesis of* $[Fe_2L^{Me}{}_3]Cl_4$ *was first described in [120], but is included here with this author's characterisation.* Ligand, $L^{Me}$ (205mg, 0.5mmol) was mixed with MeOH (50mL) and stirred for 10min before the addition of $FeCl_2 \cdot 4\,H_2O$ (68mg, 0.3mmol) dissolved in MeOH (50mL) giving a purple solution which was refluxed for three days. The reflux was allowed to cool to room temperature before the addition of a saturated methanolic solution of $NH_4PF_6$ precipitated the desired product out of solution. The purple solid was filtered, washed with MeOH and allowed to dry *in vacuo*. Yield = 0.192g (87%)

Anion exchange to $[Fe_2L^{Me}{}_3]Cl_4$ was carried out using tetrabutylammonium chloride.

$^1$H NMR (300 MHz, MeOD, 298K): $\delta$ = 8.8 (2H, d, J=8.0Hz, $H_3$), 8.8 (2H, t, J=7.5 Hz, $H_4$), 7.80 (2H, t, J=6.5 Hz, $H_5$), 7.50 (2H, dd, J=6.0 Hz, J=1.0Hz, $H_{a/b}$), 7.25 (2H, d, J=4.0 Hz, $H_6$), 6.90 (2H, dd, J=6.5Hz, J=1.5Hz, $H_{a/b}$), 5.60 (2H, dd, J=8.5Hz, J=1.5Hz, $H_{a/b}$), 4.80(2H, dd, J=8.5Hz, J= 1.5Hz, $H_{a/b}$, 4.65 (6H, s, $CH_3$), 4.10 (2H, s, $CH_2$).

raggedright ESI-MS: *m/z* = 395 $[Fe_2L^{Me}{}_3]^{4+}$

### 6.2.3 Synthesis of $[Fe_2L^{O}{}_3]Cl_4$

*This cylinder was synthesised under the same conditions as decribed in Section 6.2.1.*

Yield = 0.452g (82%) $^1$H NMR (300 MHz, $CD_3CN$, 298K): $\delta$ = 9.20 (2H, s, $H_{im}$), 8.65 (2H, d, J=7.0 Hz, $H_3$), 8.40 (2H, t, J=6.5 Hz, $H_4$), 7.85 (2H, t, J=6.0 Hz, $H_5$), 7.60 (2H, d, J=4.0 Hz, $H_6$), 6.50 (4H, bs, $H_{a/b}$), 5.80 (4H, bs, $H_{a/b}$).

ESI-MS: *m/z* = 312 $[Fe_2L^{O}{}_3]^{4+}$

### 6.2.4 Synthesis of $[Fe_2L^{S}{}_3]Cl_4$

*This cylinder was synthesised under the same conditions as decribed in Section 6.2.1.*

Yield = 0.487g (86%)

$^1$H NMR (300 MHz, $CD_3CN$, 298K): $\delta$ = 9.10 (2H, s, $H_{im}$), 8.65 (2H, d, J=7.0 Hz, $H_3$), 8.45 (2H, t, J=6.5 Hz, $H_4$), 7.85 (2H, t, J=6.0 Hz, $H_5$), 7.40 (2H, d, J=4.0 Hz, $H_6$), 7.25 (4H, bs, $H_{a/b}$), 5.55 (4H, bs, $H_{a/b}$).

ESI-MS: *m/z* = 324 $[Fe_2L^{S}{}_3]^{4+}$

## 6.3 Ru-cylinder synthesis

### 6.3.1 Synthesis of cis-$[Ru_2(DMSO)_4Cl_2]$

*The synthesis of cis-$[Ru_2(DMSO)_4Cl_2]$ was first described in Ref [58], but is included here with slight modification.*

cis-$RuCl_3 \cdot 3\,H_2O$ (1 g) was refluxed in DMSO (8 ml) for 5 min and allowed to cool. The volume was reduced by half *in vacuo* and cold acetone (20 ml) was slowly added. After refridgeration overnight, a yellow solid was filtered off, washed with acetone and ether, and vacuum dried.
Yield = 1.33g (72%)

## 6.3.2 Synthesis of $[Ru_2L_3]Cl_4$

**Reflux synthesis**

Ligand L (0.565g, 1.5mmol) and cis-$[Ru(DMSO)_4Cl_2]$ (0.484g, 1mmol) were added to ethylene glycol (20mL). The system was purged with nitrogen before being refluxed for 5 days in an oil-bath preheated to 200°C. The initial yellow mixture became a dark-orange solution upon completion of the reflux, which was then left to cool to room temperature, added to 100mL of saturated $NH_4PF_6$ aqueous solution and refrigerated overnight. The resulting dark orange precipitate was filtered, washed with cold deionised water followed by diethyl ether and left to dry in vacuo. This paste-like product was then re-precipitated from acetonitrile using diethyl ether, and again refrigerated overnight. This precipitate was filtered, washed with diethyl ether followed by chloroform and left to dry *in vacuo*.

The compound was purified by 3 successive silica gel columns using a 15mM $NH_4PF_6$ in 3:1 acetonitrile and water solution as the eluent. In all columns, the compound was eluted as the first orange band, from which the solvent was removed and the compound re-precipitated from acetonitrile using diethyl ether.
Yield = 3.2mg
$^1$H NMR $[Ru_2L_3](PF_6)_4$ (300MHz, $CD_3CN$, 25°C): $\delta$ = 8.7 (s, 1H, $H_{im}$), 8.5 (d, 1H, $H_3$), 8.3 (td, 1H, $H_4$) 7.7 (ddd, 1H, $H_5$), 7.6 (d, 1H, $H_6$), 7.0 (d, 2H, $H_{a/b}$) 5.7(d, 2H, $H_{a/b}$), 4.0 (s, 1H, $H_{CH2}$)
ESI-MS ($CH_3CN$): *m/z* = 333.1 $[Ru_2L_3]^{4+}$ (100%), 444.1 $[Ru_2L_3]^{3+}$ (50%), 811.2 $Ru2L3][PF6]2[Ru_2L_3][PF_6]_2^{2+}$ (15%)

**Microwave synthesis**

Ligand L, (225.6mg, 0.6mmol) and $RuCl_3 \cdot xH_2O$ (82.8mg, 0.4mmol) were added to 20mL ethylene glycol in a sealable microwave vial under a nitrogen atmosphere and heated at 200°C for 4 hours. This resulted in a dark brown solution which was left to cool to room temperature, added to 100mL of saturated $NH_4PF_6$ and refrigerated overnight. The cylinder was then purified using the same procedure as used for the reflux synthesis described above.
Yield = 3.0mg (1%)

## 6.4 Cu-cylinder synthesis

### 6.4.1 Synthesis of $[Cu_2L_3]Cl_4$

Ligand L, (301.9mg , 0.8mmol) and $[Cu(MeCN)_4][BF_4]$ (251.8mg, 0.08mmol) were heated under reflux at 75°C in 200mL methanol under a nitrogen atmosphere for 2hrs. The resulting red solution was left to cool to room temperature, added to 100mL of saturated $NH_4PF_6$ and refridgerated overnight. The dark red precipitate was filtered, washed with methanol and left to dry *in vacuo*.
Yield = 419.1mg, 89.6%

### 6.4.2 Synthesis of copper-anthracene cylinder

*The synthesis of anthracene-tagged ligand and the resulting cylinder were synthesised within our lab by Nicholas J Hobson. The synthesis of the final cylinder and characterisation of the final molecule is included for reference.*
A solution of 5-(anthracen-2-ylcarbamoyl)picolinic acid (20 mg, 0.06 mmol) in MeOH (5 mL) was purged with $N_2$. 4,4-methylenedianiline ( 6 mg, 0.03 mmol) in MeOH (3 mL) was added, followed by [Cu(CH3CN)4](BF4) (6.3 mg, 0.02 mmol) in MeOH (3 mL). The reaction was stirred overnight under a $N_2$ atmosphere to yield a red/brown precipitate which was isolated by filtration and washed with methanol to yield the product in 55 mg (46 %) yield. ESI mass

analysis: m/z = 878.3 $[Cu_2L^1{}_2]^{2+}$, 893.0 $[Cu_2L^1{}_2]^{2+}(CH_3OH)$, 908.3 $[Cu_2L^1{}_2]^{2+}(CH_3OH)_2$.

## 6.5 Cell Culture Protocols

MDA-MB-231 cells were purchased from Sigma Aldrich and seeded in Dulbecco's Modified Eagles' Medium (without phenol red) supplemented with 10% Foetal Bovine Serum (FBS) and 1% Penicillin, L-glutamine and streptomycin. Cells were washed with phosphate buffed saline (PBS) and placed in fresh media every 2 days and cells were split when 80% confluence was reached.

Prior to use, all coverslips were immersed in nitric acid for 10 minutes and then rinsed thoroughly in deionised water. They were finally rinsed with ethanol and left to dry in an oven. 2mg $[Ru_2L_3]^{4+}$ was dissolved in 2mL media and kept as a stock solution at 4°C.

### 6.5.1 Treatment of cells with $[Ru_2L_3]^{4+}$

24 hours prior to treatment with $[Ru_2L_3]^{4+}$, 2.0 x$10^5$ cells were seeded on glass coverslips in 6-well plates with 2mL of media. Cells were then treated with the required volume of $[Ru_2L_3]^{4+}$ in situ and incubated at 37°C for the required length of time. Each well was then washed twice with PBS and 2mL of fresh media was added. Cells were then imaged live using confocal microscopy.

### 6.5.2 Treatment of cells with Hoechst 34580 and $[Ru_2L_3]^{4+}$

24 hours prior to treatment, 2.0 x$10^5$ cells were seeded on glass coverslips in 6-well plates with 2mL of media. Cells were treated in situ with 0.4ug/mL Hoechst 34580 and incubated for 25 minutes at 37°C. Each well was washed with PBS and 2mL fresh media was added. Cells were then treated with 15uM $[Ru_2L_3]^{4+}$ and incubated for 1.5 hours. Again each well was washed twice with PBS and 2mL or fresh media was added. Cells were then imaged live using confocal microscopy.

### 6.5.3 Treatment of cells with Lifeact-GFP and $[Ru_2L_3]^{4+}$ or cytochalasin D

24 hours prior to treatment, $1x10^5$ cells were seeded on glass coverslips with 2mL of media in 6-well plates. Cells were treated with the DNA plasmid using TurboFect transfection reagent, according to the manufacturer's instructions, with slight modifications to published scale-up ratios; well volume was kept at 2mL, and a TurboFect/DNA mixture was prepared to include 3ug of DNA with 300uL serum free media and 5uL of TurboFect for each well to be treated. This was kept at room temperature for 20 minutes, and 300uL of the TurboFect/DNA mixture was added to each well, and left to incubate at 37°C for 72 hours. Cells were then washed with PBS, placed in 2mL fresh media and treated with the required concentration of $[Ru_2L_3]^{4+}$ or cytochalasin D for the desired length of time. Cells were then fixed and imaged using confocal microscopy.

### 6.5.4 ToxiLight BioAssay for detection of adenylate kinase (AK)

The ToxiLight BioAssay kit was purchased from Cambrex BioScience Ltd. $2x10^5$ cells were seeded in a 6-well plate with 2mL of media and incubated for 24 hours to allow for surface attachment. Cells were treated with 12.5, 25, 50 or 100uM $[Ru_2L_3]^{4+}$. Control samples were also prepared by treating cells with either Tris Acetate Buffer (negative control) or 100% Lysis Reagent (positive control) in a 1:2 ratio of reagent to well volume. Both reagents were supplied as part of the assay kit. Three samples of 30uL of supernatant were removed from each well after 0, 2, 4 and 6 hours and frozen until required. Once all samples had been gathered, 20uL of each collected supernatant was transferred to a 96-well plate suitable for use with a luminescence microplate reader. 100uL of supplied AK detection reagent was added to each well and left to equilibrate for 5 minutes. The intensity of the emitted light (340-700nm) was then measured using a TECAN GENios Multifunction Microplate reader.

### 6.5.5 MTT assay for determining cell viability

*Based on the method first described in [121]* 1x$10^5$ cells were seeded in a 96-well plate in 200uL of media and incubated for 24 hours to allow for surface attachment. Four wells were treated with 100, 50, 25, 12.5 or 6.25uM of desired compound. Cisplatin was used as a control on each plate tested. 72 hours after treatment, cells were washed twice with PBS and 200uL of fresh media was added. 20uL of a 5mg/mL PBS solution of MTT was added to each well, and left to incubate for 2 hours. After this, all media was removed and 200uL DMSO was added to each well and left to incubate for a further 20 minutes. The absorbance of each well at 550nm was then read. A dose-response curve was then plotted to determine the concentration of compound at which only 50% of cells were viable.

## 6.6 Statistical Analysis

Initial analysis of data was performed by determining the mean and standard deviation of the sample population, using the following formula;

$$\sqrt{\frac{\sum(x-\bar{x})^2}{n}}$$

Where x represents each data point, $\bar{x}$ represents the mean of the population and n represents the number of data points. Where appropriate, a Student's t-test has been used to determine if differences in populations show significantly different results. Determination of the t-value was performed using Excel function 'ttest', and degrees of freedom were taken as number of samples in each population less one. To determine if this result was significant, the calculated t-value was compared to those included in t-tables as printed in [122]. A confidence interval of p=0.05 and a two-tailed test were used to be confident that any significant difference in either direction was noted. Only if the calculated t-value was higher than that found within the t-tables, was the result said to be significant.

## 6.7 Imaging protocols

All confocal microscopy was performed using a Leica DM IRE2 system and visualised using Leica confocal software. A 405nm diode laser was used to acquire DIC images and a 488nm argon laser was used to acquire fluorescence images of $[Ru_2L_3]^{4+}$.

### 6.7.1 Live Cell Imaging

Coverslips were removed in turn from the 6-well plate and placed in an Attofluor cell chamber, purchased from Invitrogen. 1mL of media was added and a second coverslip was used to seal the chamber. To maintain cell integrity, a heated stage was used to keep the cells at 37°C during image acquisition.

### 6.7.2 Fixed Cell Imaging

Cells were fixed in 4% paraformaldehyde using the following protocol. 4g paraformaldehyde was dissolved in 100mL PBS and pH adjusted to 7.4 using hydrochloric acid and sodium hydroxide. Media was removed from the cells which were washed with PBS. 1mL of paraformaldehyde was added and the cells were left in the dark at room temperature for 20 minutes. The paraformaldehyde was removed and each well was washed 3 times with PBS. A small amount of Vectamount (a commercially available fixing agent) was placed on a microscope slide and the coverslip was lifted out of the media and placed cell side down onto the Vectamount. This was left to dry for 2 hours and the coverslip edges were sealed onto the microscope slide with a coat of nail varnish. Slides were then kept in the dark at 4°C until imaged.

## 6.8 Synchrotron Imaging

### 6.8.1 Quartz slide sample preparation

75x25mm quartz slides (UQG Optics Ltd, UK - Part no. FQM-7521) were washed with ethanol and a Flexiperm silicon ring cell culture chamber attached to each slide. 2mL of FBS was added to the growth chamber for 30 minutes to aid cell attachment. After removing the FBS, 200,000 cells in 2mL media were added to each growth chamber. Slides were stored in petri dishes and incubated at 37°C in 5% $CO_2$ for 24hrs. Cells were then treated with compound at the required concentration and time. Cells were then washed with PBS and fixed by plunge freezing in dry-ice cooled methanol. Cells were stored at -20°C until required for imaging.

### 6.8.2 $SiN_3$ window sample preparation

5x5mm silicon nitride windows with membrane thickness 200nm (Silson Ltd, UK. Ref 10610106) were washed by dipping in ethanol, followed by PBS and then media before being placed in individual wells of a 6-well plate. To ensure cells attached predominantly to the window, a concentrated stock of $2x10^5$ cells in 1mL of media was prepared. 80uL of this stock ($\approx$16,000 cells) was added directly on top of each window and left to begin to adhere for 45mins. 2mL of fresh media was added to each well and cells were incubated for 24hrs. Cells were treated with compound and frozen in the same way as described in 6.8.1.

### 6.8.3 Synchrotron imaging and XANES spectroscopy

Once mounted onto the I18 beamline, samples were optically imaged to use a reference for elemental distribution maps. A helium cryojet was used to protect the cells from radiation damage. A four element Vortex detector was used in rastering mode to measure X-ray fluorescence. A beam of approximately 5x5 microns was used to map areas of $\approx 200x200um^2$ to allow for imaging of a number of cells in each imaging run. A beam energy of 11keV was used to map the metals of interest (Fe and Ni) whilst also detecting cellular elements such as Cl, Ca and Zn. Where areas of high metal concentration were found, XANES spectra were recorded using beam energy appropriate for the K-edge of each metal - 7112keV for Fe and 8333keV for Ni. XANES spectra of pellets of cylinder powder were also recorded for reference. Reference spectra of Fe foil and ferrihydrite were provided by Dr Tina Geraki of Diamond. Elemental maps were generated constructed using PyMCA software [123] by normalising the fluorescence signals with the incoming X-ray beam intensity, $I_0$. Signal peaks due to detector glitches were removed by applying an upper limit on normalised intensity at the 99th percentile. XANES spectra were analysed using Athena software (IFFEIT) [92], protocols for background subtraction were provided by Dr Tina Geraki [88]. The pre-edge background was removed by a linear approximation in the range of 30 to 150 eV for iron (or -13 to -21 eV for nickel) before the edge and subtraction of this baseline from the overall data. The spectra was then normalised by fitting a quadratic polynomial to the post-edge region of the spectra from 48 to 97 eV when looking at iron data, or 44 to 85 eV when looking at nickel. The edge position of the element was identified as the maximum in the first derivative of the spectrum, which correlated to the inflection point of the steeply rising edge. Linear combination analysis was performed followed protocols as provided within Athena manuals, with spectra of all standards available included within the population used by Athena to determine fitting.

# Chapter 7

# Conclusions and Future Work

Three key aspects of work regarding the cylinders has been addressed in this work - the synthesis of a ruthenium based cylinder, determining the cellular localisation of the cylinders also determining the cellular effects of the cylinders.

The first issued considered was to improve the synthetic protocol of the ruthenium cylinder. This is the most challenging of the cylinders to make, due to the non-reactive nature of the starting materials and the formation of polymeric side products. Within the literature, there is only one other example of a ruthenium triple helicate compound [64], and it was this paper that was used as a starting point for developing a microwave synthesis protocol. The 36 % yield achieved by Glasson *et al.* could not be repeated with the ruthenium cylinder, which was surprising given the similarity between the two compounds. It was however noted as part of this work, that the syntheses that gave the greatest yields were those where no pressure built up within the microwave system. This has led to the conclusion that there is a contaminant within some of the attempted syntheses that has a higher vapour pressure than the intended components, leading to incomplete reactions within the microwave. This therefore leads to a suggestion for future work to be to consider further which solvents are suitable for use within a microwave, and then favour those which are available as dry solvents so hopefully removing any contaminants. The purification of the ruthenium cylinder has historically also been problematic, with both large amounts of material adhering to the solid phase of any column chromatograph and also the cylinder elutes very closely to other by-products. This continues to remain an issue, however the use of Sephadex as a solid phase (as opposed to silica or alumina) has led to a more efficient purification, as now only two columns are typically required to obtain pure ruthenium cylinder as opposed to the three or four used previously. An increased yield in percentage terms is now reported, with a shorter synthetic protocol which now no longer required the synthesis of an intermediary compound, $Ru(DMSO)_4Cl_2$. This therefore represents a positive step forward for the synthesis of this compound. However, this work may still be able to be improved upon by surveying a family of Ru(II) compounds as it is hypothesised that starting with a metal of the required oxidation state would lead to a higher yield. As discussed earlier in this work the fluorescent properties of the ruthenium cylinder mean that improving the synthesis of this compound is something that is worthwhile, to allow for further investigation into the cellular localisation of this class of compounds.

As the synthesis of the ruthenium cylinder continued to be time-consuming, an alternative strategy of imaging a cylinder which has been modified to contain a fluorescent moiety has also been investigated. A modified copper based cylinder which contains an anthracene group attached to the end of each ligand has been prepared within the research group [73], but has been considered as part of this work as its suitability as an imaging probe. The use of an integrated UV-Vis spectrometer has shown that the anthracene moiety remains bound to parent ligand within MDA-MB-231 cells, but as no fluorescence due to a metal-ligand transition is observed, it cannot be said if the cylinder structure is stable as a whole. The addition of the anthracene moiety vastly increases the size of each ligand, making it difficult to form a triple stranded cylinder. Whilst the double stranded cylinders have previously been synthesised [124], they have not previously been used within cellular studies. The related compound $[Cu_2L_2]^{2+}$ has been shown to be stable in solution following stability studies performed using absorption spectroscopy, and so this does present a potential future line of work. However by altering the cylinder structure, none of the data previously gathered in relation to the triple stranded cylinder can be relied upon to be relevant for this compound. This is especially true given that it has already been found that the reduced charge on a copper double-stranded cylinder is responsible for reduced DNA binding in solution when compared to iron cylinder [124]. It is therefore proposed that any future work performed utilising a fluorophore tagged cylinder is part of development of that compound in its own right - although difficult to produce, to use fluorescence microscopy to view the localisation of the cylinders needs to be performed utilising an inherent property of the cylinders, only then can any results found from imaging studies be truly correlated to any cell assays or DNA binding studies already performed.

A first attempt at determination of the cellular localisation of the cylinders has been undertaken, with initial confocal microscopy showing observable fluorescence from the ruthenium cylinder within MDA-MB-231 cells, but not within SKOV-3 cells. This result opened a series of questions, such as is the lack of fluorescent signal due to preferential uptake of the ruthenium cylinder in MDA-MB-231 compared to SKOV-3 cells, or is it due to the ruthenium cylinder being metabolised within the SKOV-3 cells (and so losing the $Ru-N_6$ chromophore) but remaining intact within MDA-MB-231 cells? MTT data presented here has shown that free ruthenium is not toxic to SKOV-3 cells and it has previously been shown that the free ligand is also not toxic to this cell line [42]. The iron analogue of the cylinder has been shown to be toxic to SKOV-3 cells [41], so there is no reason to believe that the ruthenium cylinder would not be taken into the SKOV-3 cells, however there is no conclusive evidence to say that the cylinder has in fact entered the cell. It therefore remains unclear as to why no fluorescence is observed within these samples. It does however show a degree of selectivity in the uptake or metabolism of this compound in these two cell lines. As one of the main drawbacks of initial anti-cancer metallo-drugs was a lack of selectivity between cell types, this result does add to cell test data showing that not all cell lines are affected by the cylinders [14], further enhancing the potential for this class of compounds to be considered for use in clinical applications.

An initial 'proof of concept' experiment has shown that it is possible to perform co-localisation experiments with Hoechst nuclear stains, which appear to show a reduction in mean fluorescence in MDA-MB-231 cells which have been labelled with Hoechst, following further treatment with iron cylinder. This suggests that the cylinder is either quenching Hoechst emission, or is displacing it from binding to DNA. The initial result presented here has since been supported by further research within the group that showed over a Z-stack of images capturing entire cells, mean Hoechst fluorescence decreased following treatment with the iron cylinder [76]. These results combined show that at least some of the cylinder that enters the cells is localised within the nucleus of MDA-MB-231 cells. This is a significant result as it means that the DNA-binding studies performed in solution, particularly those that show prevention of DNA replication [44], may be replicated within a cellular environment.

But it is synchrotron radiation that seemingly offers the most promising route to investigating cylinder localisation within cells. This is due to the compound being able to be imaged without requiring any properties such as fluorescence, or modification to achieve fluorescence. It also allows for the imaging of multiple cylinders in multiple cell lines under comparable conditions, and as such, this represents the main focus of future work. A sample preparation route of growing cells on silicon nitride windows has been developed, and allowed for the imaging of iron and nickel cylinders within SKOV-3 cells. This showed that high levels of iron are found near the cell membrane, corresponding to areas of high calcium concentration, whereas nickel is found more uniformly spread throughout the cell. However, as both nickel and iron are endogenous elements, the aim continues to be to use this technique to image ruthenium within cells, as all ruthenium observed can then only be attributable to treatment with the cylinder. This however is not possible using the I-18 beamline at Diamond Light Source. The K-edge of Ru is around 22keV which is above the 20.5keV upper energy limit of I-18. The L-lines of Ru (L$\alpha$=2.56keV and L$\beta$=2.68keV) are within the energy range of I-18 but they coincide with the K-lines of Cl (K$\alpha$=2.62keV and K$\beta$=2.82keV) and, given the abundance of Cl within the cells, the would make distinguishing the two elements very difficult. Any further work in this respect would have to be performed at another facility such as Advanced Photon Source, Chicago. However, the imaging of iron has led to the observation of ’hot spots’ near the cell membrane. Linear combination analysis of XANES spectra (including standards of ferrihydrite and powdered cyliner) of these areas show that the iron found there is a mixture of Fe(III) and Fe(II). This finding of an environment of mixed Fe oxidation states does however support a hypothesis that the iron cylinder may be taken into cells using the transferrin pathway. This represents the first time that any chemical information about the cylinder has been obtained within a biological system, and so again opens up new avenues of further investigation such as potential co-localisation studies between cells containing fluorescently tagged transferrin receptors and the cylinders.

As well as attempting to determine the localisation of the cylinder, the cellular effects of cylinder treatment upon two cell lines have also been imaged by producing phase contrast videos. The striking observation from these videos being that the motility of cells is compromised by cylinder treatment. While this effect has not been quantified, the consistency with which this observation was noted lead to cause of the arrest to be investigated. As a polymer that is well known to be involved in cell motility [96], the effect of the cylinders upon the cellular actin structure has been investigated. Given the filamentous nature of actin structure, it was hypothesised that the cylinder would be able to bind to the junctions of actin fibres, much in the same way it binds to Y-shaped junctions of DNA. The actin structure of MDA-MB-231 cells was shown to be disrupted following cylinder treatment, but it is now understood that this is not due to direct binding of the cylinder to actin - fluorescence co-localisation studies led to very little overlap being observed between the two. When the structures of compounds which are know to bind to actin such as phalloidin, cytochalasin D and Lifeact (all of which are significantly larger, more flexible molecules) are considered, it is perhaps unsurprising that the cylinder does not specifically bind to actin. A literature review of factors affecting the motility of the MDA-MB-231 cell line led to research being uncovered which debated the impact of NO upon this cell line, and indeed a debate on whether these cells produce endogenous NO [104], [106], [107] and [108]. Using a newly developed NO cellular probe, $NO_{550}$, the production of NO within MDA-MB-231 cells was observed following treatment with both iron cylinder and ruthenium nitrosyl, which was used as a positive control. Very low levels of fluorescence were observed within the control sample, which adds evidence to the literature debate that these cells do indeed contain endogenous NO. The observation of increased NO within the cells following treatment with iron cylinder is a significant advancement in the understanding of the mode of action of these compounds. Whilst it was known that the ruthenium cylinder can lead to the production of singlet oxygen within a cell [3], this was only observed following UV irradiation - this is the first time the cylinders have been seen to lead to the production of a gaseous species within a cell. Future work in this respect must therefore concentrate on repeating this experiment in multiple cell lines, with multiple cylinders and at multiple time points to determine if it is the level of production of NO within cells that is determining the overall toxicity of the cylinders.

This work represents the first attempt at using imaging techniques to determine the localisation and effect of a class of novel cancer therapeutics on a range on cancer cell lines. Whilst progress has been made to answer these questions, there any now many more avenues of work which can be pursued to discover the full range of effects the cylinders have upon a cell, and so establish if this class of compounds can be considered a truly promising cancer therapeutic.

# Chapter 8

# Bibliography

[1] M. J. Hannon, V. Moreno, M. J. Prieto, E. Moldrheim, E. Sletten, I. Meistermann, C. J. Isaac, K. J. Sanders, and A. Rodger. Intramolecular DNA coiling mediated by a metallo-supramolecular cylinder. *Angewandte Chemie International Edition*, 40(5):879–884, 2001.

[2] A. Oleksi, A. G. Blanco, R. Boer, I. Us*ó*n, J. Aymam*í*, A. Rodger, M. J. Hannon, and M. Coll. Molecular recognition of a three-way dna junction by a metallosupramolecular helicate. *Agnewandte Chemie International Edition*, 45:1227–1231, 2006.

[3] J. Malina, M. J. Hannon, and V. Brabec. Recognition of dna three-way junctions by metallosupramolecular cylinders: Gel electrophoresis studies. *Chemistry - A European Journal*, 13:3871–3877, 2007.

[4] G.I. Pascu, A.C.G. Hotze, C. Sanchez-Cano, B.M. Kariuki, and M.J. Hannon. Dinuclear ruthenium (II) triple-stranded helicates: Luminescent supramolecular cylinders that bind and coil DNA and exhibit activity against cancer cell lines. *Angewandte Chemie*, 119(23):4452–4456, 2007.

[5] P. Lang, K. Yeow, A. Nichols, and A. Scheer. Cellular imaging in drug discovery. *Nature Reviews Drug Discovery*, 5:343–356, 2006.

[6] C. A. Puckett and J. K. Barton. Methods to explore cellular uptake of ruthenium complexes. *Journal of the American Chemical Society*, 129:46–47, 2007.

[7] R. Safaei, K. Katano, B. J. Larson, G. Samimi, A. K. Holzer, W. Naerdemann, M. Tomioka, M. Goodman, and S. B. Howell. Intracellular localization and trafficking of fluorescein-labeled cisplatin in human ovarian carcinoma cells. *Clinical Cancer Research*, 11(2):756–767, 2005.

[8] P. Marqu*é*s-Gallego, H. den Dulk, J. Brouwer, S. Tanase, I. Mutikainen, U. Turpeinen, and J. Reedijk. Cytotoxic activity and cellular processing in human ovarian carcinoma cell lines of a new platinum(II) compound containing a fluorescent substituted propylene diamine ligand. *Biochemical Pharmacology*, 78:365–373, 2009.

[9] M. R. Gill, J. Garcia-Lara, S. J. Foster, C. Smythe, G. Battaglia, and J. A. Thomas. A ruthenium(II) polypyridyl complex for direct imaging of DNA structure in living cells. *Nature Chemistry*, 1:662–667, 2009.

[10] X. Tian, M. R. Gill, I. Cant*ó*n, J. A. Thomas, and G. Battaglia. Live cell luminescence imaging as a function of delivery mechanism. *ChemBioChem*, 12:548–551, 2011.

[11] N. A. O'Connor, N. Stevens, D. Samaroo, M. R. Solomon, A. A. Mart*í*, J. Dyer, H. Vishwasrao, D. L. Akins, E. R. Kandel, and N. J. Turro. A covalently linked phenanthridne-ruthenium(II) complex as a RNA probe. *Chemistry Communications*, 19:2640–2642, 2009.

[12] C. A. Puckett and J. K. Barton. Targeting a ruthenium complex to the nucleus with short peptides. *Bioorganic & Medicinal Chemistry*, 18:3564–3569, 2010.

[13] J. B. Aitken, S. Antony, C. M. Weekley, B. Lai, L. Spiccia, and H. H. Harris. Distinct cellular fates for KP1019 and NAMI-A determined by X-Ray fluorescence imaging of single cells. *Metallomics*, 4:1051–1056, 2012.

[14] A. J. Pope. *Supramolecular Anticancer Agents and their Effects on Cells and Biomolecules*. PhD thesis, University of Birmingham, 2011.

[15] Y. Yang, S. K. Seidlits, M. M. Adams, V. M. Lynch, C. E. Schmidt, E. V. Anslyn, and J. B. Shear. A highly selective low-background fluorescent imaging agent for nitric oxide. *Journal of the American Chemical Society*, 132(38):13114–13116, 2010.

[16] S. S. Rubakhin, J. C. Jurchen, E. B. Monroe, and J. V. Sweedler. Imaging mass spectrometry: fundamentals and applications to drug discovery. *Drug Discovery Today*, 10(12):823–837, 2005.

[17] P. J. Todd, T. G. Schaaff, P. Chaurand, and R. M. Caprioli. Organic ion imaging of biological tissue with secondary ion mass spectrometry and matrix-assisted laser desorption/ionization. *Journal of Mass Spectrometry*, 36(4):355–369, 2001.

[18] Y. Hsieh, J. Chen, and W. A. Korfmacher. Mapping pharmaceuticals in tissues using MALDI imaging mass spectrometry. *Journal of Pharmacological and Toxicological Methods*, 55(2):193 – 200, 2007.

[19] B. Rosenburg, L. VanCamp, and T. Krigas. Inhibition of cell division in escherichia coli by electolysis products from a platiunum electrode. *Nature*, 205:698–699, 1965.

[20] B. Rosenburg, E. Renshaw, L. VanCamp, J. Hartwick, and J. Drobnik. Plantinum-induced filamentous growth in escherichia coli. *Journal of Bacteriology*, 93:716–721, 1967.

[21] N. J. Wheate, S. Walker, G. E. Craig, and R. Oun. The status of platinum anticancer drugs in the clinic and in clinical trials. *Dalton Trans.*, 39:8113–8127, 2010.

[22] E. R. Jamieson and S.J. Lippard. Structure, recognition, and processing of cisplatin-DNA adducts. *Chemical Reviews*, 99(9):2467–2498, 1999.

[23] J. S. Mymryk, E. Zaniewski, and T. K. Archer. Cisplatin inhibits chromatin remodeling, transcription factor binding and transcription from the mouse of mammary tumor virus

promoter *in vivo*. *Proceedings of the National Academy of Sciences*, 92:2076–2080, 1995.

[24] S. Ishida, J. Lee, D. J. Thiele, and I. Herskowitz. Uptake of the anticancer drug cisplatin mediated by the copper transporter CTR1 in yeast and mammals. *Proceedings of the National Academy of Sciences*, 99(22):14298–14302, 2002.

[25] G. Samimi, N. M. Varki, S. Wilczynski, R. Safaei, D. S. Alberts, and S. B. Howell. Increase in expression of the copper transporter ATP7A during platinum drug-based treatment is associated with poor survival in ovarian cancer patients. *Clinical Cancer Research*, 9(16):5853–5859, 2003.

[26] K. D. Ivy and J. H. Kaplan. A re-evaluation of the role of hCTR1, the human high-affinity copper transporter, in platinum-drug entry into human cells. *Molecular Pharmacology*, 83:1237–1246, 2013.

[27] J. A. Gottlieb and B. Drewinko. Review of the current clinical status of platinum coordination complexes in cancer chemotherapy. *Cancer chemotherapy reports. Part 1*, 59(3):621, 1975.

[28] T. Schilling, B. K. Keppler, M. E. Heim, G. Niebch, H. Dietzfelbinger, J. Rastetter, and A. R. Hanauske. Clinical phase I and pharmacokinetic trial of the new titanium complex budotitane. *Investigational New Drugs*, 13(4):327–332, 1996.

[29] E. Meléndez. Titanium complexes in cancer treatment. *Critical Reviews in Oncology/Hematology*, 42(3):309 – 315, 2002.

[30] C. Gabbiani, A. Casini, and L. Messori. Gold(III) compounds as anticancer drugs. *Gold Bulletin*, 40:73–81, 2007.

[31] M. F. R. Fouda, M. M. Abd-Elzaher, R. A. Abdelsamaia, and A. A. Labib. On the medicinal chemistry of ferrocene. *Applied Organometallic Chemistry*, 21(8):613–625, 2007.

[32] A. Bergamo, R. Gagliardi, V. Scarcia, A. Furlani, G. Alessio, E. amd Mestroni, and G. Sava. In vitro cell cycle arrest, in vivo action on solid metastasizing tumors, and host toxicity of the antimetastatic drug NAMI-A and cisplatin. *The Journal of Pharmacology and Experimental Therapeutics*, 289:559–564, 1999.

[33] C. G. Hartinger, M. A. Jakupec, S. Zorbas-Seifried, M. Groessl, A. Egger, W. Berger, H. Zorbas, P. J. Dyson, and B. K. Keppler. KP1019, a new redox-active anticancer agent - preclinical development and results of a clinical phase I study in tumor patients. *Chemistry & Biodiversity*, 5(10):2140–2155, 2008.

[34] E. Alessio and G. Sava. *Personal Communication*, 2013.

[35] G. Sava, S. Zorzet, C. Turrin, F. Vita, M. Soranzo, G. Zabucchi, M. Cocchietto, A. Bergamo, S. DiGiovine, G. Pezzoni, L. Sartor, and S. Garbisa. Dual action of nami-a in inhibition of solid tumor metastasis - selective targeting of metastatic cells and binding to collagen. *Clinical Cancer Research*, 9:1898–1905, 2003.

[36] M. Groblewska, M. Siewko, B. Mroczko, and M. Szmitkowski. The role of matrix metalloproteinases (MMPs) and their inhibitors (TIMPs) in the development of esophageal cancer. *Folia Histochemica et Cytobiologica*, 50:12–19, 2012.

[37] P. Heffeter, K. Böck, B Atil, M. A. R. Hoda, W. Körner, C. Bartel, U. Jungwirth, B. K. Keppler, M. Micksche, W. Berger, and G. Koellensperger. Intracellular protein binding patterns of the anticancer ruthenium drugs KP1019 and KP1339. *Journal of Biological Inorganic Chemistry*, 15:737–748, 2010.

[38] M. J. Clarke. Ruthenium metallopharmaceuticals. *Coordination Chemistry Reviews*, 236:209–233, 2003.

[39] M. Groessl, Y. O. Tsybin, C. G. Hartinger, B. K. Keppler, and P. J. Dyson. Ruthenium versus platinum: interactions of anticancer metallodrugs with duplex oligonucleotides characterised by electrospray ionisation mass spectrometry. *Journal of Biological Inorganic Chemistry*, 15:677–688, 2010.

[40] M. Groessl, O. Zava, and P. J. Dyson. Cellular uptake and subcellular distribution of ruthenium-based metallodrugs under clinical investigation versus cisplatin. *Metallomics*, 3:591–599, 2011.

[41] A. C. G. Hotze, N. J. Hodges, R. E. Hayden, C. Sanchez-Cano, C. Paines, N. Male, M. Tse, C. M. Bunce, K. J. Chipman, and M. J. Hannon. Supramolecular iron cylinder with unprecedented DNA binding is a potent cytostatic and apoptotic agent without exhibiting genotoxicity. *Chemistry and Biology*, 15(12):1258 – 1267, 2008.

[42] C. Sanchez-Cano. *Biomolecular interactions and cellular effects of steroidal and metallosupramolecular metallodrugs*. PhD thesis, University of Birmingham, 2009.

[43] J. Malina, M. J. Hannon, and V. Brabec. Interaction of dinuclear ruthenium(II) supramolecular cylinders with DNA: Sequence-specific binding, unwinding and photocleavage. *Chemistry - A European Journal*, 14(33):10408–10414, 2008.

[44] C. Ducani, A. Leczkowska, N. J. Hodges, and M. J. Hannon. Noncovalent DNA-binding metallo-supramolecular cylinders prevent dna transactions in vitro. *Angewandte Chemie International Edition*, 49(47):8942–8945, 2010.

[45] G. Krishna and M. Hayashi. In vivo rodent micronucelus assay: protocol, conduct and data interpretation. *Mutation Research*, pages 155–166, 2000.

[46] *Global Approach in Safety Testing: ICH Guidelines Explained*. Springer, 2013.

[47] C. A. Puckett and J. K. Barton. Mechanism of cellular uptake of a ruthenium polypyridyl complex. *Biochemistry*, 47:11711–11716, 2008.

[48] P. Watson, A. T. Jones, and D. J. Stephens. Intracellular trafficking pathways and drug delivery: fluorescence imaging of living and fixed cells. *Advanced Drug Delivery Reviews*, 57:43–61, 2005.

[49] J. H. Price, A. Goodacre, K. Hahn, L. Hodgson, E. A. Hunter, S. Krajewski, R. F. Murphy, A. Rabinovich, J. C. Reed, and S. Heynen. Advances in molecular labeling,

high throughput imaging and machine intelligence portend powerful functional cellular biochemistry tools. *Journal of Cellular Biochemistry Supplement*, 39:194–210, 2002.

[50] C. Molenaar, J. Teuben, R. J. Heetebrij, H. J. Tanke, and J. Reedijk. New insights in the cellular processing of platinum antitumor compounds, using fluorophore-labeled platinum complexes and digital fluorescence microscopy. *Journal of Biological Inorganic Chemistry*, 5(5):655–665, 2000.

[51] D. Ding, K. Li, Z. Zhu, K-Y. Pu, Y. Hu, X. Jiang, and B. Liu. Conjugated polyelectrolyte-cisplatin complex nanoparticles for simultaneous *in vivo* imaging and drug tracking. *Nanoscale*, 3(5):1997–2002, 2011.

[52] N. H. Damrauer, G. Cerullo, A. Yeh, T. R. Boussie, C. V. Shank, and J. K. McCusker. Femtosecond dynamics of excited-state evolution in $[Ru(bpy)_3]^{2+}$. *Science*, 54:54–57, 1997.

[53] J. N. Demas and A. W. Adamson. A new photosensitizer. tris(2,2'-bipyridine)ruthenium(II) chloride. *Journal of the American Chemical Society*, 93(7):1800–1801, 1971.

[54] A. E. Friedman, J-C. Chambron, J-P. Sauvage, N. J. Turro, and J. K. Barton. Molecular "'light switch"' for DNA: $Ru(bpy)_2(dppz)^{2+}$. *Journal of the American Chemical Society*, 112:4960–4962, 1990.

[55] C. Rajput, R. Rutkaite, L. Swanson, I. Haq, and J. A. Thomas. Dinuclear monointercalating ru(II) complexes that display high affinity binding to duplex and quadruplex (DNA). *Chemistry - A European Journal*, 12:4611–4619, 2006.

[56] G-J. Lin, G-B. Jiang, Y-Y. Xie, H-L. Huang, Z-H. Liang, and Y-J. Liu. Cytotoxicity, apoptosis, cell cycle arrest, reactive oxygen species, mitochondrial membrane potential, and western blotting analysis of ruthenium(II) complexes. *Journal of Biological Inorganic Chemistry*, 2013.

[57] A Leczkowska. *Non-covalent DNA binding ruthenium anticancer drugs*. PhD thesis, University of Birmingham, 2011.

[58] I. P. Evans, A. Spencer, and G. Wilkinson. Dichlorotetrakis(dimethyl sulphoxide)ruthenium(II) and its use as a source material for some new ruthenium(II) complexes. *J. Chem. Soc., Dalton Trans.*, pages 204–209, 1973.

[59] E. Alessio, G. Mestroni, G. Nardin, A. M. Wahib, M. Calligaris, G. Sava, and S. Zorzet. *cis*- and *trans*- dihalotetrakis(dimethyl sulfoxide) ruthenium (II) complexes: Synthesis, structure and antitumor activity. *Inorganic Chemistry*, 27:4099–4106, 1988.

[60] P. Lidstr*ö*m, J. Tierney, B. Wathey, and J. Westman. Microwave assisted organic synthesis - a review. *Tetrahedron*, 57(45):9225 – 9283, 2001.

[61] D. Martineau, M. Beley, and P. C. Gros. Pyrrolidine-containing polypyridines: New ligands for improved visible light absorption by ruthenium complexes. *The Journal of Organic Chemistry*, 71(2):566–571, 2006.

[62] K. Servaty, C. Moucheron, and A. Kirsch-De Mesmaeker. Trinuclear ruthenium dendrons based on bridging PHEHAT and TPAC ligands. *Dalton Trans.*, 40:11704–11711, 2011.

[63] S. Rau, B. Sch*ä*ß fer, A. Gr*ü*ing, S Schebesta, K. Lamm, J. Vieth, H. G*ö*rls, D. Walther, M. Rudolph, U. W. Grummt, and E. Birkner. Efficient synthesis of ruthenium complexes of the type $(R{-}bpy)_2RuCl_2$ and $[(R{-}bpy)_2Ru(L{-}L)]Cl_2$ by microwave-activated reactions (R: H, Me, tert-But) (L-L: substituted bibenzimidazoles, bipyrimidine, and phenanthroline). *Inorganica Chimica Acta*, 357(15):4496 – 4503, 2004.

[64] C. R. K. Glasson, G. V. Meehan, J. K. Clegg, L. F. Lindoy, J. A. Smith, F. R. Keene, and C. Motti. Microwave synthesis of a rare $[Ru_2L_3]^{4+}$ triple helicate and its interaction with DNA. *Chemistry - A European Journal*, 14(34):10535–10538, 2008.

[65] *The Properties of Gases and Liquids*. McGraw-Hill, New York, 2001.

[66] O. Ciocirlan and O. Iulian. Vapour pressure, density, viscosity and refractive index of dimethyl sulfoxide + 1,4-dimethylbenzene system. *Hungarian Journal of Industrial Chemistry*, 31:23–29, 2003.

[67] C. Mesangeau, S. Yous, B. Peres, D. Lesieur, and T. Besson. Pictet-spengler heterocyclizations via microwave-assisted degredation of dmso. *Tetrahedron Letters*, 46:2465–2468, 2005.

[68] M. Maestri, N. Armaroli, V. Balzani, E. C. Constable, and A. M. W. Cargill-Thompson. Complexes of the ruthenium(II)-2,2':6',2"-terpyridine family. Effect of electron-accepting and -donating substituents on the photophysical and electrochemical properties. *Inorganic Chemistry*, 34(10):2759–2767, 1995.

[69] U.S. Schubert and H. Hofmeier. Metallo-supramolecular graft copolymers: a novel approach toward polymer-analogous reactions. *Macromolecular rapid communications*, 23(9):561–566, 2002.

[70] G. Sathyaraj, T. Weyherm*ü*ller, and B. U. Nair. Synthesis, characterization and DNA binding studies of new ruthenium(II)bisterpyridine complexes. *European Journal of Medicinal Chemistry*, 45(1):284 – 291, 2010.

[71] A. C. G. Hotze, J. A. Faiz, N. Mourtzis, G. I. Pascu, P. R. A. Webber, G. J. Clarkson, K. Yannakopoulou, Z. Pikramenou, and M. J. Hannon. Far-red luminescent ruthenium pyridylimine complexes; building blocks for multinuclear arrays. *Dalton Transactions*, pages 3025–3034, 2006.

[72] L. Cardo, V. Sadovnikova, S. Phongtongpasuk, N. J. Hodges, and M. J. Hannon. Arginine conjugates of metallo-supramolecular cylinders prescribe helicity and enhance DNA junction binding and cellular activity. *Chemistry Communications*, 47:6575–6577, 2011.

[73] N. J. Hobson. *Synthesis of Fluorescent Ligands to Monitor Iron (II) Metallosupramolecular Mechansims in Cells*. PhD thesis, University of Birmingham, 2011.

[74] C. L. Painting. *Metallo-assembled Supramolecular Architectures*. PhD thesis, University of Warwick, 1999.

[75] L.J. Childs, J. Malina, B.E. Rolfsnes, M. Pascu, M.J. Prieto, M.J. Broome, P.M. Rodger, E. Sletten, V. Moreno, A. Rodger, et al. A dna-binding copper (I) metallosupramolecular cylinder that acts as an artificial nuclease. *Chemistry-A European Journal*, 12(18):4919–4927, 2006.

[76] Z. Khan and M. J. Hannon. *Personal Communication*, 2013.

[77] A. A. Hummer and A. Rompel. The use of x-ray absorption and synchrotron based micro-x-ray fluorescence spectroscopy to investigate anti-cancer metal compounds *in vivo* and *in vitro*. *Metallomics*, 5:597–614, 2013.

[78] I. Ascone, L. Messori, A. Casini, C. Gabbiani, A. Balerna, F. Dell'Unto, and A. C. Castellano. Exploiting soft and hard x-ray absorption spectroscopy to characterize metallodrug/protein interactions: the binding of [*trans*-$RuCl_4$(im)(dimethylsulfoxide)][ImH] (Im = imidazole) to Bovine Serum Albumin. *Inorganic Chemistry*, 47:8629–8634, 2008.

[79] A Levina, J. B. Aitken, Y. Y. Gwee, Z. J. Lim, M. Liu, A. M. Singharay, P. F. Wong, and P. A. Lay. Biotransformations of anticancer ruthenium(III) complexes: An x-Ray absorption spectroscopic study. *Chemistry - A European Journal*, 19:3609–3619, 2013.

[80] R. McRae, B. Lai, and C. J. Fahrni. Subcellular redistribution and mitotic inheritance of transition metals in proliferating mouse fibroblast cells. *Metallomics*, 5:52–61, 2013.

[81] C. J. Fahrni. Biological applications of x-ray fluorescence microscopy: exploring the subcellular topography and speciation of transition metals. *Current Opinion in Chemical Biology*, 11(2):121 – 127, 2007.

[82] K. J. Davis, J. A. Carrall, B. Lai, J. R. Aldrich-Wright, S. F. Ralph, and C. T. Dillon. Does cytotoxicity of metallointercalators correlate with cellular uptake or DNA affinity? *Dalton Transactions*, 41:9417–9426, 2012.

[83] E. Kosior, S. Bohic, H. Suhonen, R. Ortega, G. Dev*é*s, A. Carmona, F. Marchi, J. F. Guillet, and P. Cloetens. Combined use of hard X-ray phase conbtrast imaging and X-ray fluorescence microscopy for sub-cellular metal quantification. *Journal of Structural Biology*, 177:239–247, 2012.

[84] Z. M. Qian and P. L. Tang. Mechanisms of iron uptake by mammalian cells. *Biochemica et Biophysica Acta*, 1269:205–214, 1995.

[85] M. Kawamoto, T. Horibe, M. Kohno, and K. Kawakami. A novel transferrin receptor-targeted hybrid peptide disintegrates cancer cell membrane to induce rapid killing of cancer cells. *BMC Cancer*, pages 11–359, 2011.

[86] H. Lodish, A. Berk, S. L. Zipursky, P. Matsudaira, D. Baltimore, and J. Darnell. *Molecular Cell Biology, 4th edition.* WH Freeman, 2000.

[87] A. Al-Ebraheem, J. Goettlicher, K. Geraki, S. Ralph, and M. J. Farquharson. The determination of zinc, copper and iron oxidation state in invasive ductal carcinoma of breast tissue and normal surrounding tissue using XANES. *X-Ray Spectrometry*, 39:332–337, 2010.

[88] T. Geraki. *Personal Communication*, 2014.

[89] M. D. Hall, C. T. Dillon, M. Zhang, P. Beale, Z. Cai, B. Lai, A. P. J. Stampfl, and T. W. Hambley. The cellular distribution and oxidation state of platinum(II) and platinum(IV)

antitumour complexes in cancer cells. *Journal of Biological Inorganic Chemistry*, 8:726–732, 2003.

[90] E. A. Carter, B. S. Rayner, A. I. McLeod, L. E. Wu, C. P. Marshall, A. Levina, J. B. Aitken, P. K. Witting, B. Lai, Z. Cai, S. Vogt, Y-C. Lee, C-I Chen, M. J. Tobin, H. H. Harris, and P. A. Lay. Silicon nitride as a versatile growth substrate for microspectroscopic imaging and mapping of individual cells. *Molecular BioSystems*, 6:1316–1322, 2010.

[91] S. Antony, J. B. Aitken, S. Vogt, B. Lai, T. Brown, L. Spiccia, and H. H. Harris. X-ray fluorescence imaging of single human cancer cells reveals that the N-heterocyclic ligands of iodinated analogues of ruthenium anticancer drugs remain coordinated after cellular uptake. *Journal of Biological Inorganic Chemistry*, 18:845–853, 2013.

[92] B. Ravel and M. Newville. ATHENA, ARTEMIS, HEPHAESTUS: data analysis for x-ray absorption spectroscopy using IFEFFIT. *Journal of Synchrotron Radiation*, 12(4):537–541, 2005.

[93] T. K. Sham. X-ray absorption spectra of ruthenium l edges in $Ru(NH_3)_6Cl_3$. *Journal of the American Chemical Society*, 105(8):2269–2273, 1983.

[94] A. Thompson, D. Attwood, E. Gullikson, M. Howells, K-J. Kim, J. Kirz, J. Kortright, I. Lindau, Y. Liu, P. Pianetta, A. Robinson, J. Scofield, J. Underwood, G. Williams, and H. Winick. X-ray data booklet. *Center for X-Ray Optics and Advanced Light Source*, 2009.

[95] Y. Parajo, J. Malina, I. Meistermann, G. J. Clarkson, M. Pascu, A. Rodger, M. J. Hannon, and P. Lincoln. Effect of bridging ligand structure on the thermal stability and DNA binding properties of iron(II) triple helicates. *Dalton Trans.*, pages 4868–4874, 2009.

[96] J. Riedl, A.H. Crevenna, K. Kessenbrock, J.H. Yu, D. Neukirchen, M. Bista, F. Bradke, D. Jenne, T.A. Holak, Z. Werb, et al. Lifeact: a versatile marker to visualize F-actin. *Nature methods*, 5(7):605–607, 2008.

[97] G. Sava, F. Frausin, M. Cocchietto, F. Vita, E. Podda, P. Spessotto, A. Furlani, V. Scarcia, and G. Zabucchi. Actin-dependent tumour cell adhesion after short-term exposure to the antimetastasis ruthenium complex NAMI-A. *European Journal of Cancer*, 40(9):1383–1396, 2004.

[98] F. Lizárraga, R. Poincloux, M. Romao, G. Montagnac, G. Le Dez, I. Bonne, G. Rigaill, G. Raposo, and P. Chavrier. Diaphanous-related formins are required for invadopodia formation and invasion of breast tumor cells. *Cancer Research*, 69:2792–2800, 2009.

[99] J. Zanet, A. Jayo, S. Plaza, T. Millard, M. Parsons, and B. Stramer. Fascin promotes filopodia formation independent of its role in actin bundling. *The Journal of Cell Biology*, 197(4):477–486, 2012.

[100] D. A. Wink, Y. Vodovotz, J. Laval, F. Laval, M. W. Dewhirst, and J. B. Mitchell. The multifaceted roles of nitric oxide in cancer. *Carcinogenesis*, 19:711–721, 1998.

[101] A. W. Carpenter and M. H. Schoenfisch. Nitric oxide release: Part II. therapeutic applications. *Chemical Society Reviews*, 41:3742–3752, 2012.

[102] A. J. Burke, F. J. Sullivan, F. J. Giles, and S. A. Glynn. The yin and yang of nitric oxide in cancer progression. *Carcinogenesis*, 34:503–512, 2013.

[103] R. G. Knowles and S. Moncada. Nitric oxide synthases in mammals. *Biochemistry Journal*, 298:249–258, 1994.

[104] S. Pervin, R. Singh, and G. Chaudhuri. Nitric oxide-induced cytostasis and cell cycle arrest of a human breast cancer cell line (MDA-MB-231): Potential role of cyclin D1. *Proceedings of the National Academy of Sciences*, 98:3583–3588, 2001.

[105] R. Zeillinger, E. Tantscher, C. Schneeberger, W. Tschugguel, S. Eder, G. Sliutz, and J. C. Huber. Simultaneous expression of nitric oxide synthase and estrogen receptor in human breast cancer cell lines. *Breast Cancer Research and Treatment*, 40:205–207, 1996.

[106] R. Singh, S. Pervin, A. Karimi, S. Cederbaum, and G. Chaudhuri. Arginase activity in human breast cancer cell line: N$^{\omega}$-Hydroxy-L-arginine selectively inhibits cell proliferation and induces apoptosis in MDA-MB-468 cells. *Cancer Research*, 60:3305–3312, 2000.

[107] N. E. Mathews, M. A. Adams, L. R. Maxwell, T. E. Gofton, and C. H. Graham. Nitric oxide-mediated regulation of chemosensitivity in cancer cells. *Journal of the National Cancer Institute*, 93:1879–1885, 2001.

[108] M. Lahiri and J. H. J. Martin. Nitric oxide decreases motility and increases adhesion in human breast cancer cells. *Oncology Reports*, 21:275–281, 2009.

[109] A-M. Simeone, S. Colella, R. Krabe, M. M. Johnson, E. Mora, and A. M. Tari. N-(4-hydroxyphenyl)retinamide and nitric oxide pro-drugs exhibit apoptotic and anti-invasive effects against bone metastic breast cancer cells. *Carcinogenesis*, 27(3):568–577, 2006.

[110] H. Kojima, N. Nakatsubo, K. Kikuchi, S. Kawahara, Y. Kirino, H. Nagoshi, Y. Hirata, and T. Nagano. Detection and imaging of nitric oxide with novel fluorescent indicators: Diaminofluoresceins. *Analytical Chemistry*, 70:2446–2453, 1998.

[111] M. H. Lim, D. Xu, and S. J. Lippard. Visualization of nitric oxide in living cells by a copper-based fluorescent probe. *Nature Chemical Biology*, 2(7):375–380, 2006.

[112] S. Wang, M-Y. Han, and D. Huang. Nitric oxide switches on the photoluminescence of molecularly engineered quantum dots. *Journal of the American Chemical Society*, 131:11692–11694, 2009.

[113] J. A. T. Pugh, A. G. Cox, C. W. McLeod, J. Bunch, M. J. Writer, S. L. Hart, A. Bienemann, E. White, and J. Bell. Elemental imaging of MRI contrast agents: benchmarking of LA-ICP-MS to MRI. *Analytical and Bioanalytical Chemistry*, 403:1641–1649, 2012.

[114] N. Davies, D. E. Weibel, P. Blenkinsopp, N. Lockyer, R. Hill, and J.C. Vickerman. Development and experimental application of a gold liquid metal ion source. *Applied Surface Science*, 203-204:223 – 227, 2003.

[115] S. C. C. Wong, R. Hill, P. Blenkinsopp, N. P. Lockyer, D. E. Weibel, and J. C. Vickerman. Development of a $C_{60}^+$ ion gun for static sims and chemical imaging. *Applied Surface Science*, 203-204:219 – 222, 2003.

[116] K. Tanaka, H. Waki, Y. Ido, S. Akita, Y. Yoshida, and T. Yoshida. Protein and polymer analyses up to *m/z* 100,000 by laser ionization time of flight mass spectrometry. *Rapid Communications in Mass Spectrometry*, 2:151–153, 1988.

[117] M. Karas and F. Hillenkamp. Laser desorption ionization of proteins with molecular masses exceeding 10,000 daltons. *Analytical Chemistry*, 60(20):2299–2301, 1988.

[118] R. M. Caprioli, T. B. Farmer, and J. Gile. Molecular imaging of biological samples: Localization of peptides and proteins using MALDI-TOF MS. *Analytical Chemistry*, 69(23):4751–4760, 1997.

[119] R. L. Griffiths and J. Bunch. A survey of useful salt additives in matrix-assited laser desorption/ionization mass spectrometry and tandem mass spectrometry of lipids: intorducing nitrates for improved analysis. *Rapid Communications in Mass Spectrometry*, 26:1557 – 1566, 2012.

[120] J. M. C. A. Kerckhoffs, J. C. Peberdy, I. Meistermann, L. J. Childs, C. J. Isaac, C. R. Pearmund, V. Reudegger, S. Khalid, N. W. Alcock, M. J. Hannon, and A. Rodger. Enantiomeric resolution of supramolecular helicates with different surface topographies. *Dalton Transaction*, pages 734–742, 2007.

[121] T. Mosmann. Rapid colorimetric assay for cellular growth and survival: Application to proliferation and cytotoxicity assays. *Journal of Immunological Methods*, 65:55–63, 1983.

[122] E.S. Pearson and H.O. Hartley. *Biometrika Tables for Statisticians*. Cambridge University Press, 1956.

[123] V. A. Solé, E. Papillon, M. Cotte, P. Walter, and J. Susini. A multiplatform code for the analysis of energy-dispersive x-ray fluorescence spectra. *Spectrochimica Acta Part B: Atomic Spectroscopy*, 62(1):63 – 68, 2007.

[124] L. J. Childs, J. Malina, B. E. Rolfsnes, M. Pascu, M. J. Prieto, M. J. Broome, P. M. Rodger, E. Sletten, V. Moreno, A. Rodger, and M. J. Hannon. A dna-binding copper(i) metallosupramolecular cylinder that acts as an artificial nuclease. *Chemistry - A European Journal*, 12(18):4919–4927, 2006.

# Chapter 9

# Publications Arising

Work contained within this thesis has been presented as posters at two conferences, the abstracts of which are included here.

**Exploring the structure of anti-cancer metallosupramolecular cylinders in biological systems**

Laura E Rowley[1], Richard L Williams[1], Zahra Khan[1], Lindsey van Gemeren[1], Tina Geraki[2], Josephine Bunch[1] and Michael J Hannon[1]

[1]*PSIBS Doctoral Training Centre, University of Birmingham, Birmingham UK, B15 2TT*
[2]*Diamond Light Source Ltd, Harwell Science and Innovation Campus, Oxfordshire*
*OX11 0DE*

**Figure 9.1:** Abstract submitted to Diamond Synchrotron Users Meeting, September 2012

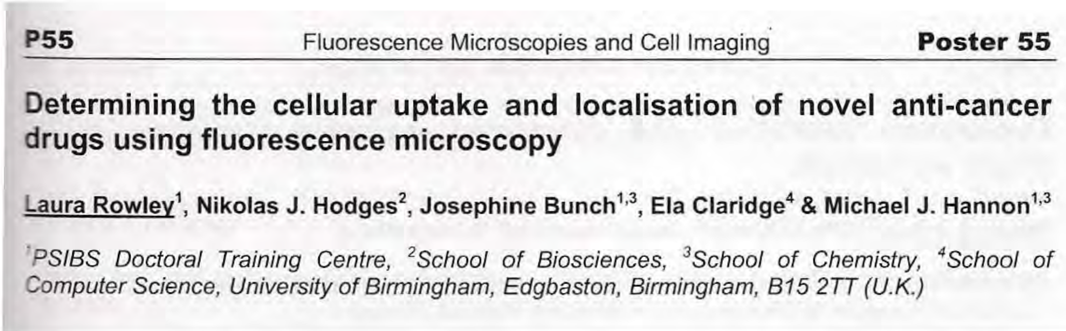

**P55** Fluorescence Microscopies and Cell Imaging **Poster 55**

## Determining the cellular uptake and localisation of novel anti-cancer drugs using fluorescence microscopy

**Laura Rowley[1], Nikolas J. Hodges[2], Josephine Bunch[1,3], Ela Claridge[4] & Michael J. Hannon[1,3]**

*[1]PSIBS Doctoral Training Centre, [2]School of Biosciences, [3]School of Chemistry, [4]School of Computer Science, University of Birmingham, Edgbaston, Birmingham, B15 2TT (U.K.)*

**Figure 9.2:** Abstract submitted to MAF 12 - 12th International Conference on Methods and Applications of Fluorescence, September 2011